

ABSTRACT

Title of thesis: **DESIGN OF AN ANTHROPOMORPHIC
ROBOTIC HAND FOR SPACE OPERATIONS**

Emily Tai, Master of Science, 2007

Thesis directed by: Associate Professor David L. Akin
Department of Aerospace Engineering

Robotic end-effectors provide the link between machines and the environment. The evolution of end-effector design has traded off between simplistic single-taskers and highly complex multi-function grippers. For future space operations, launch payload weight and the wide range of desired tasks necessitate a highly dexterous design with strength and manipulation capabilities matching those of the suited astronaut using EVA tools.

The human hand provides the ideal parallel for a dexterous end-effector design. This thesis discusses efforts to design an anthropomorphic robotic hand, focusing on the detailed design, fabrication, and testing of an individual modular finger with considerations into overall hand configuration. The research first aims to define requirements for anthropomorphism and compare the geometry and motion of the design to that of the human hand. Active and passive ranges of motion are studied along with coupled joint behavior and grasp types. The second objective is to study the benefits and drawbacks of an active versus passive actuation systems. Tradeoffs between controllability and packaging of actuator assemblies are considered. Finally,

a kinematic model is developed to predict tendon tensions and tip forces in different configurations. The results show that the measured forces are consistent with the predictive model. In addition, the coupled joint motion shows similar behavior to that of the human hand.

DESIGN OF AN ANTHROPOMORPHIC
ROBOTIC HAND FOR SPACE OPERATIONS

by

Emily Tai

Thesis submitted to the Faculty of the Graduate School of the
University of Maryland, College Park in partial fulfillment
of the requirements for the degree of
Master of Science
2007

Advisory Committee:

Associate Professor David L. Akin, Chair/Advisor

Assistant Professor Sean Humbert

Dr. Mary Bowden

© Copyright by

Space Systems Laboratory

University of Maryland

2007

DEDICATION

To my mom and dad:

Thank you for giving me the opportunity to succeed and
for always being there along the way.

ACKNOWLEDGMENTS

Along the ever winding and seemingly unending path that was my thesis, I was extremely fortunate to have so many people that helped me along the way. I am deeply grateful for everyone who helped me make it to the end.

My first thanks go to the faculty, staff, and students at the Space Systems Lab. Not only have you helped and supported me over the past few years, you've also made it an amazing environment to work in. You inspire creativity and persistence and have been the biggest influence on me at Maryland since I started as a lab undergrad. Thanks to Dave for all the opportunities you've given me. Thank you Dave Hart for making me a reasonably competent person. Thanks to all the grad students for all your support and for the much-needed distractions. Mike, I'm impressed we survived putting up with each other for the past 35,000 hours straight. A special thanks to Madeline, without whom nothing would have gotten done. Kiwi, thanks for keeping me sane.

My greatest thanks go to my family. Thank you mom and dad for always believing in me and pushing me to my limits. Thanks to my big sister, who has been an inspiration my whole life.

Rich, thanks for reminding me to stop for a minute and look up at the sky.

TABLE OF CONTENTS

| | |
|---|-----|
| List of Tables | vi |
| List of Figures | vii |
| List of Abbreviations | ix |
| 1 Introduction | 1 |
| 1.1 Motivation | 1 |
| 1.2 Organization of Thesis | 4 |
| 2 Robotic Hand Designs | 5 |
| 2.1 Industrial Grippers | 5 |
| 2.2 Early Hands | 6 |
| 2.2.1 Utah/MIT Hand | 7 |
| 2.2.2 Salisbury Hand | 8 |
| 2.3 Barrett Hand | 9 |
| 2.4 Gifu Hand | 11 |
| 2.5 CyberHand | 12 |
| 2.6 Shadow Hand | 13 |
| 2.7 Robonaut Hand | 14 |
| 2.8 SSL Hand | 15 |
| 3 Design Requirements | 17 |
| 3.1 Human Hand Anatomy | 18 |
| 3.2 Anthropomorphic Requirements | 22 |
| 3.2.1 Hand Sizing | 22 |
| 3.2.2 Joint Range of Motion | 23 |
| 3.3 Grasp Requirements | 25 |
| 3.3.1 Grasp Classification | 25 |
| 3.3.2 Grasp Force Requirements | 26 |
| 3.3.3 Grasp Distribution | 27 |
| 3.4 Joint Torque Requirements | 29 |
| 4 Hardware Development | 31 |
| 4.1 Hand Configuration | 31 |
| 4.2 Finger Skeletal Structure | 32 |
| 4.2.1 Compliant Mechanism Development | 32 |
| 4.2.2 MP Joint Design | 35 |
| 4.2.3 Phalange Connection | 37 |
| 4.3 Actuation System | 40 |
| 4.3.1 Actuator Type Selection | 40 |
| 4.3.2 Tendon Forces and Motor Selection | 44 |
| 4.3.3 Component Selection | 46 |

| | | |
|-------|--|-----|
| 4.3.4 | Packaging | 48 |
| 4.3.5 | Passive vs. Active Actuation | 49 |
| 4.4 | Sensors | 50 |
| 4.4.1 | Position and Force Sensing | 51 |
| 4.4.2 | Tactile Sensing | 52 |
| 5 | Kinematics Analysis | 54 |
| 5.1 | Finger Kinematics | 54 |
| 5.1.1 | Forward Kinematics | 54 |
| 5.1.2 | Inverse Kinematics | 56 |
| 5.1.3 | Velocities and Static Forces | 59 |
| 5.1.4 | Jacobian Matrix | 60 |
| 5.2 | Multifingered Hand Kinematics | 62 |
| 5.2.1 | Hand Kinematics | 62 |
| 5.2.2 | Grasp Quality Considerations | 63 |
| 6 | Testing and Results | 66 |
| 6.1 | Test Setup | 66 |
| 6.2 | Data/Results | 69 |
| 6.2.1 | Coupled Joint Angles | 69 |
| 6.2.2 | Tendon Forces in a Cylindrical Grasp | 70 |
| 6.2.3 | Active Antagonism | 72 |
| 7 | Conclusions & Future Work | 76 |
| 7.1 | Summary | 76 |
| 7.2 | Future Work | 77 |
| 7.2.1 | Single Finger Development | 77 |
| 7.2.2 | Three-Finger Grasper | 78 |
| 7.2.3 | Five-Finger Hand | 79 |
| A | Design Measurements and Calculations | 81 |
| A.1 | Hand Measurements | 81 |
| A.2 | Matlab Code | 83 |
| A.2.1 | Leadscrew Selection Calculations | 83 |
| A.2.2 | Motor/Gearbox Calculations | 84 |
| A.2.3 | Finger Force-Moment Analysis | 85 |
| B | Component Drawings | 87 |
| C | Kinematic Analysis | 99 |
| C.1 | Mathematica Code | 99 |
| C.2 | Inverse Kinematics | 111 |
| | Bibliography | 115 |

LIST OF TABLES

| | | |
|-----|---|----|
| 3.1 | Desired Sizing for Finger Design | 23 |
| 3.2 | Hand Range of Motion Requirements | 24 |
| 3.3 | Force Distribution in Cylindrical Grip[1, 2] | 27 |
| 3.4 | Force Distribution Over Phalanges in Cylindrical Grip[1, 2] | 28 |
| 3.5 | Mean values of force centers | 29 |
| 3.6 | Hand Geometry for $\varnothing 2.00''$ Cylindrical Grasp | 29 |
| 3.7 | 20 lb Load Distribution (all values given in lbs) | 30 |
| 3.8 | Joint Torques for a 20 lb Cylindrical Grasp, $\varnothing 2.00''$ | 30 |
| 4.1 | Comparison of Actuator Types | 43 |
| 4.2 | Peak and Holding Forces for Unweighted Setup | 45 |
| 5.1 | Denavit-Hartenberg Parameters for Finger | 55 |
| A.1 | Human Forearm and Hand Measurements | 81 |
| A.2 | Hand Measurements | 82 |

LIST OF FIGURES

| | | |
|-----|---|----|
| 1.1 | Ranger TSX | 3 |
| 2.1 | Pivoting Jaw (top row) and Parallel Jaw (bottom row) Grippers[3] . . | 5 |
| 2.2 | Utah/MIT Hand | 7 |
| 2.3 | Stanford/JPL Hand[3] | 9 |
| 2.4 | Barrett Hand | 10 |
| 2.5 | Gifu Hand | 11 |
| 2.6 | CyberHand concept | 12 |
| 2.7 | Shadow Dexterous Hand | 13 |
| 2.8 | Robonaut | 15 |
| 2.9 | SSL Hand[4] | 16 |
| 3.1 | Bones and Joints of the Hand | 19 |
| 3.2 | Direction of Joint Motion | 20 |
| 3.3 | Relation Between PIP and DIP Flexion, Right Index Finger[5] | 21 |
| 3.4 | Bio-Concepts Hand Measurement Chart[6] | 22 |
| 3.5 | Finger joint angle flexion for varying cylinder diameters, averaged over digits II-V | 28 |
| 4.1 | Cross section of compliant hinge | 35 |
| 4.2 | Exploded View of MP Joint | 36 |
| 4.3 | Assembled MP Joint | 36 |
| 4.4 | Exploded View of Finger | 39 |
| 4.5 | Full Finger Assembly (palm not shown) | 39 |
| 4.6 | Projected Actuation Tendon Forces | 44 |
| 4.7 | Experimentally Derived Tendon Forces | 46 |

| | | |
|-----|---|-----|
| 4.8 | Actuator Packaging in Forearm | 49 |
| 5.1 | Kinematic Structure of Individual Finger | 54 |
| 6.1 | Side View & Close-Up of Load Cells/Top Plate | 67 |
| 6.2 | Close-up of Load Cell Attachment and Top Plate | 68 |
| 6.3 | PIP-DIP Joint Coupling | 70 |
| 6.4 | Tendon Tensions for Applied Loads on a 1.25" Diameter Cylindrical Grasp | 71 |
| 6.5 | DIP Flexion for Varying Antagonistic Tendon Tensions | 73 |
| 6.6 | PIP Flexion for Varying Antagonistic Tendon Tensions | 73 |
| 6.7 | Tip Force vs Joint Torque | 74 |
| C.1 | Geometric View in Arm Plane | 113 |

LIST OF ABBREVIATIONS

| | |
|------|--|
| CATs | Crew Aids and Tools |
| CNS | Central Nervous System |
| DH | Denavit-Hartenberg |
| DIP | Distal Interphalangeal |
| DOF | Degrees of Freedom |
| EAP | Electroactive Polymer |
| EMG | Electromyography |
| EVA | Extravehicular Activity |
| IEEM | Interchangeable End Effector Mechanism |
| IP | Interphalangeal |
| JPL | Jet Propulsion Laboratory |
| MIT | Massachusetts Institute of Technology |
| MP | Metacarpophalangeal |
| PIP | Proximal Interphalangeal |
| PNS | Peripheral Nervous System |
| SMA | Shape Memory Alloy |

Chapter 1

Introduction

Robots have the potential to play a large role in our world. They are currently widely used in industrial applications for labor-intensive operations that require a high level of precision and repetition. In addition, robots can be found in the entertainment industry in the form of toys and animatronics. The function of robots in society is constantly evolving and current research endeavors to bring them further into the realm of domestic assistance, medicine, military, search and rescue, and exploration. In many of these applications, the robot must perform only one specific task and thus can be designed to handle a single operation. However, as the potential use for robots grows, so does their need to interact with objects in their environment. The design of end effectors that can pick up a variety of objects and utilize them as tools is a significant challenge in robot development.

1.1 Motivation

Single function end effectors such as parallel jaws, tools drives, and specialized grippers are commonly seen on robotic systems today. These interfaces have the benefit of simplicity in design and thus increased reliability and reduced maintenance costs. However, in order to perform multiple tasks, a single robot would need to have either multiple arms with different end effectors or the ability to swap end

effectors. Situations requiring greater flexibility thus need a more universal method to interact with the environment.

Robots for space exploration applications, such as planetary surface sampling and extravehicular activity (EVA) operations, typically benefit from a more universal, high-dexterity end effector. For EVA operations in particular, there are currently 242 crew aids and tools (CATs) and interfaces that are used during tasks performed outside the space shuttle. Several more exist for other operational purposes and in developmental stages for future use. Among the many categories of CATs and interfaces are common wrench and cutter type tools, drive tools, power and electrical equipment, restraints, and adapters[4]. Each of these CATs is designed to be used by a suited astronaut. For a robot to be of assistance in general EVA operations, it must be able utilize all the required CATs and interfaces. The options are thus to design a different robot for each job, provide a single robot with a large set of tool and gripper attachments, or design an end effector capable of the same grasps as a suited astronaut.

The Ranger Telerobotic Shuttle Experiment (TSX), developed by the Space Systems Lab at the University of Maryland, College Park, was designed to demonstrate on-orbit telerobotic servicing technologies (Figure 1.1). Ranger's design concept views the end-effector as the tool, rather than the interface to the tool. Thus, the Ranger TSX arms utilize a specialized set of interchangeable end-effectors that can use EVA interfaces. The primary weakness in this system is the number of specialized tools needed to complete a job, particularly on extended servicing missions. As the number increases, the total cost to design, manufacture, and launch a full

set of end-effectors becomes prohibitive. In addition, each individual end-effector is limited in mobility as the Interchangeable End Effector Mechanism (IEEM) allows for a maximum of two degrees of freedom (DOF)[7]. Tasks requiring high dexterity are thus unachievable by this system.

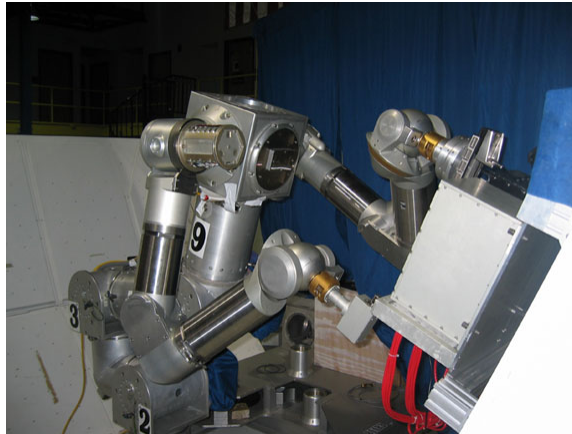


Figure 1.1: Ranger TSX

A final issue with the interchangeable mechanism is the need to swap out end-effectors between tasks. If the robot is not capable of performing the change on its own, a human operator must intervene, which either places a human in the environment or halts work while the robot is removed for exchange. Though Ranger has demonstrated its ability to perform complex servicing missions, the use of a single, highly dexterous end-effector would eliminate many of the restrictions of single function end-effectors.

The human hand is a prime example of a high dexterity end-effectors. The hand is capable of a multitude of power and precision grasps. It is thus able to pick up a wide range of objects and utilize them as tools in various fashions. Research in robotic hand design has ranged from simplified opposing grippers to highly anthropomorphic designs. For the purposes of EVA operations, a human hand serves

as the basis for all tools and thus makes a good basis for a robotic equivalent.

This research examines the design and analysis of an anthropomorphic end effector for use in EVA and exploration operations. To achieve these goals, the structure and use of the human hand as applied to a robotic design is examined. The scope of this thesis also establishes the requirements for anthropomorphic grasping of EVA CATs and interfaces and details the design of a finger and its configuration within a robotic hand. In addition, a kinematic model is built and testing is done to demonstrate anthropomorphic geometry and operational capability in EVA applications.

1.2 Organization of Thesis

The scope of this thesis is to document the design of an anthropomorphic robotic end effector, compare its performance to that of a human hand, and examine the related kinematics.

Chapter 2 discusses previous robotic end-effector development. Characterization of human hand geometry and performance as well as the derived design requirements are outlined in Chapter 3. Chapter 4 describes the development process and final design. The kinematic model is explained in Chapter 5. Chapter 6 details the testing process. Finally, Chapter 7 summarizes the results of testing and future work to advance the state of the design.

Chapter 2

Robotic Hand Designs

2.1 Industrial Grippers

Grasping and manipulation needs have driven end effector development in various directions. Dedicated task devices such as welders, bolt drivers, and paint sprayers may be better suited than the human hand to perform specific tasks. In many cases, these end effectors may be more efficient and economical than complex hand designs. As a result, dedicated task devices are commonly found in industrial robotics. However, general use grippers are necessary to advance the field of robotics. The two leading general end effector designs in the industrial market today are pivoting finger grippers and parallel jaw grippers (Figure 2.1). Both types are low dexterity and are thus limited in their applications.

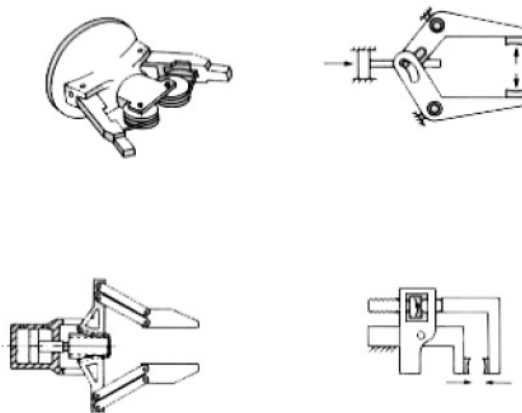


Figure 2.1: Pivoting Jaw (top row) and Parallel Jaw (bottom row) Grippers[3]

Turret and quick-change grippers are utilized in an effort to make up for the low dexterity of pivoting and parallel grippers. In order to perform a wider range of tasks, the turret gripper rotates between various individual end effectors. The turret provides a fast and simple method for alternating between tools, but is large in size and limited to a finite set of grippers. The quick-change gripper selects from grippers stored externally on a rack, much like the Ranger IEEM previously described. While providing a smaller end effector interface than the turret, this method is still limited by the number of individual tools available.

Industrial end effector design is primarily driven by providing commercially viable products that can function in an assembly line system. However, as the use of robots for non-specialized tasks expands, so does the need for a high dexterity end effector. To achieve this level of robotic sophistication, universities and research institutions are studying the control, compact design, and kinematics problems that must be solved to produce a fully anthropomorphic hand.

2.2 Early Hands

The first high dexterity robotic hands were developed in the 1980s. These initial research-oriented designs utilized various quasi-anthropomorphic configurations and actuation systems. Intended to broaden the study of mechanical design, kinematics, and control, many of the early hands are still in use in universities and corporate research departments today. Of these early prototypes, the two most well known are the Utah/MIT Hand and the Salisbury Hand.

2.2.1 Utah/MIT Hand

The Utah/Massachusetts Institute of Technology (MIT) Dexterous Hand, shown in Figure 2.2 below, was designed by the Center for Engineering Design at the University of Utah in conjunction with the Artificial Intelligence Laboratory at MIT. Created primarily as a research tool to examine controls, tactile sensing, and anthropomorphic design, it has four fingers and employs a pulley-based tendon drive[8].



Figure 2.2: Utah/MIT Hand

<http://www.cs.rochester.edu/u/jag/vision/lab/UtahMIT.jpg>

The overall configuration has three modular four DOF fingers mounted parallel to the palm plane with a non-anthropomorphic thumb orientation. Unlike the human hand, the Utah/MIT thumb is mounted near the center of the palm in direct opposition to the fingers. Joint mobility gives $0-95^\circ$ for the distal hinge joints, $\pm 25^\circ$ for the base yaw of the fingers, and $\pm 45^\circ$ for the base yaw of the thumb. Despite the non-anthropomorphic configuration, the total joint mobility allows for near natural interaction between the thumb and fingertips.

The drive system involves 32 individual pneumatic actuators with opposing tendons for each joint. Flat Dacron and Kevlar tendons are routed throughout the

system by a series of axial twists and bends over pulleys. These tendons allow for actuators to be located remotely. However, the transmission system is prohibitively large and bulky for practical use outside of laboratory research. The pneumatic actuators generate 25 lbs of tendon force, resulting in a maximum tip force of 7 lbs. In addition, the fingers can execute rapid motions at frequencies greater than 10 Hz, the minimum threshold defined by the project to perform dynamic tasks.

Integrated joint angle and tendon tension sensors provide the necessary feedback for control system design research. The Utah/MIT Hand utilizes Hall effect sensors to obtain accurate joint angle information. Initially, designers hoped to place tendon tension sensors at the joint interface. However, due to packaging problems, the tendon force transducers were moved to the wrist. These sensors use a semiconductor strain gauge bridge to measure beam deflection, which is proportional to tendon tension.

With its quasi-anthropomorphic configuration, the Utah/MIT Hand, including its wrist, provides over 25 DOFs. While not suitable for commercial applications, it provides an excellent research platform. Since its development, control system experiments studying task definition, manipulation strategies, grasping functions, and the sensor utilization have been conducted.

2.2.2 Salisbury Hand

The Salisbury Hand, previously known as the Stanford/Jet Propulsion Laboratory (JPL) Hand, was developed by Kenneth Salisbury as part of his doctoral

dissertation. This hand also serves primarily as a research tool for studying the design and control of high dexterity robotic hands[9]. Unlike the Utah/MIT Hand, the Salisbury Hand does not use an anthropomorphic design. The hand instead consists of three fingers configured with one in opposition, providing a stable spherical grasp (Figure 2.3). Each finger has three DOFs and is actuated by four Teflon-coated cables driven by remotely located servomotors. To help compensate for the fewer total DOFs, the distal joint of each finger has a wider range of motion than the human joint, thus making more grasp types possible.

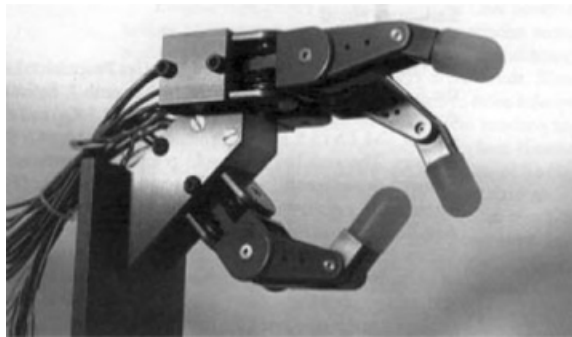


Figure 2.3: Stanford/JPL Hand[3]

The Salisbury Hand is equipped with tendon tension sensors, motor position encoders, and six-axis fingertip force torque sensors for tactile operations. Maximum output force is approximately 10 lbs with a minimum force sensing capacity of 0.01 lb. Several research institutions continue to use the Salisbury Hand to explore haptic models, control systems, and articulated manipulation.

2.3 Barrett Hand

More recently, robotic hand research has produced increasingly dexterous, commercially available end effectors. While many have tracked towards increasingly

humanoid designs, the Barrett Hand is a novel non-anthropomorphic manipulator with considerable grasp capabilities[10]. Intended for factory usage, the Barrett Hand is a highly programmable, three-fingered, eight-axis, reconfigurable "grasper" (Figure 2.4). The palm and the three articulated fingers are a self-contained unit, weighing 1.18kg and requiring only a cable for power and communications to operate. A single motor drives each finger. A fourth motor allows two of the fingers to spread around the palm, providing the capability to reconfigure itself.



Figure 2.4: Barrett Hand

<http://www.barretttechnology.com/robot/customer/CustServ.JPG>

The Barrett Hand also utilizes an innovative cable pre-tensioning system. In order to maintain reliable, high performance of a tendon drive system, the cables must be pre-tensioned to approximately 50% of the maximum operating tensions. Most methods used in other cable systems are highly complex and require significant effort. Barrett Technology endeavored to devise a simple pre-tensioning technique that could properly tune the cables in a single action by a single person with one hand and did not require any form of locking device. These goals were achieved by using a worm drive to relatively counter-rotate a pinion shaft and pinion sleeve

relative to one another[11]. With the pinion shaft and sleeve attached to opposing tension elements, this provides for a method to pretension the cable with the single motion of turning the worm.

2.4 Gifu Hand

While most hand designs discussed utilize some form of cable drive, the Gifu hand took the alternative approach of using built-in servomotors. The Gifu hand is highly anthropomorphic with the total size of thumb, four modular fingers, and palm being only slightly larger than the human hand. Each of the fingers has four joints with the thumb providing four DOFs and each finger providing three DOFs. As with the human hand, the distal finger joints are coupled in the Gifu hand. This design uses a planar four-bar linkage mechanism to achieve the coupling.



Figure 2.5: Gifu Hand

<http://robo.mech.gifu-u.ac.jp/image/title.1.jpg>

Six-axis force sensors are integrated into the fingertips of the Gifu hand. In addition, distributed tactile sensor can be integrated externally over the hand. Combined with a bandwidth greater than that of the human hand, the Gifu hand provides an excellent test bed for controls research.

2.5 CyberHand

Biomechatronics brings a new level of complexity to robotic hand design. The CyberHand, developed at the Scuola Superiore Sant'Anna in Italy, is one of the more recent efforts to bring robotic hand design and prosthetics together. For this design goal, weight and size become a greater priority over high dexterity. Due to the packaging constraints, the CyberHand uses miniature embedded motors instead of a tendon system. Two motors per finger are located in the palm. While compact and robust, this design provides a lower maximum output force than most robotic hands designed for strict manipulation purposes. This drawback is commonly found for embedded actuators versus tendon systems.

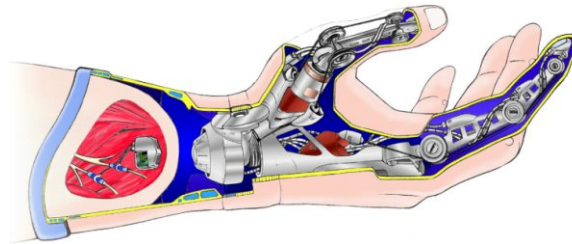


Figure 2.6: CyberHand concept
<http://www.cyberhand.org/>

Prosthetic design also adds a new level of consideration in the field of controls. Ideally, a prosthetic will involve a highly dexterous robotic hand that can attach to the human arm and both feel and control naturally. Most previous work in “natural” control interfaces have typically been limited to using electromyography (EMG) to read the electrical signals generated by muscle contraction. The human hand uses efferent neural signals sent from the central nervous system (CNS) to the peripheral nervous system (PNS), controlling the muscles. Sensory information



Figure 2.7: Shadow Dexterous Hand
<http://www.shadowrobot.com/media/pictures.shtml>

from natural sensors in the hand is then sent back to the CNS by means of afferent peripheral nerves. The CyberHand is attempting to mimic this process by designing a neural interface and an efferent neural signal processing technique that combined, can interface with the natural and artificial world. In addition, work is underway to develop biomimetic sensors and utilize them to stimulate the afferent nerves, thus sending tactile and other sensing information back to the CNS[12].

2.6 Shadow Hand

One of the most advanced anthropomorphic robotic hands today is the Shadow Dexterous Hand. The Shadow hand is highly anthropomorphic in size and shape and unlike all the previous designs discussed, utilizes air muscles to control the joints. The hand uses 36 air muscles coupled to the joints by tendons in both opposing muscle pairs and in single muscle with spring return setups. Designed to provide comparable force output and sensitivity to the human hand, it can move at only approximately half the speed.

The Shadow Hand has 20 DOFs, including two wrist DOFs. Each finger has

four joints with the distal and middle phalanges coupled, leaving three DOFs. The thumb has five joints and five DOFs. The final hand DOF is an extra palm joint by the little finger. A Hall effect sensor system provides information about joint position. Tactile sensing is embedded in the fingertips and pads. Two large area tactels are placed on the middle and proximal phalanges while the fingertips contain 34 discrete tactels, providing highly sensitive touch sensing capabilities[13].

2.7 Robonaut Hand

Looking specifically at end effector development for EVA operations, the Robotic Systems Technology Branch at NASA Johnson Space Center has developed Robonaut to work on with external space structures with human interfaces. The Robonaut hand, shown in Figure 2.8 below, is a highly anthropomorphic, fourteen DOF hand. The hand was designed to mimic as closely as possible the size, strength, and kinematics of a suited astronaut hand. In addition, in order to make the device EVA compatible, the materials and components were selected to operate under EVA conditions.

The primary components of the Robonaut hand are the forearm which houses all fourteen brushless motors and drive electronics, a two DOF wrist, and a five finger, twelve DOF hand. The hand is split into a dexterous work set for manipulation and a grasping set used to maintain stable grasps. Two three DOF fingers (pointer and middle) and a three DOF opposable thumb make up the dexterous set. As with the previous designs, the PIP and DIP joints of the fingers are coupled. The



Figure 2.8: Robonaut

<http://media.nasaexplores.com/03-012/robonaut2.jpg>

grasping set consists of two one DOF fingers (ring and pinky) and a palm joint. All fingers are shock mounted to the palm[14].

Flexible drive trains allow for remotely located motors in the forearm. The motors are coupled to short, sheathed flex shafts connected to small, modular lead-screw assemblies. The leadscrew assembly includes a load cell for force feedback and a short cable used to actuate the joints. Yaw joint control is achieved by antagonistic cables while the pitch joints utilize spring return.

The Robonaut hand has fewer degrees of freedom than the human hand, but maintains a high level of dexterity. It has demonstrated the capability to manipulate many of the CATs used by astronauts and perform several EVA tasks.

2.8 SSL Hand

Previous work in hand design for EVA applications at the Space Systems Lab yielded the SSL Hand, a four-finger non-anthropomorphic end effector. Each finger

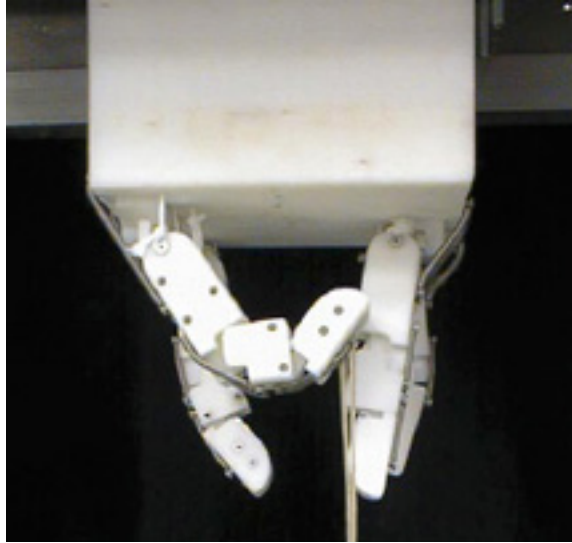


Figure 2.9: SSL Hand[4]

has four joints and three DOFs with the distal and middle segments coupled by means of a four-bar linkage. Three fingers arranged in an opposing configuration are optimized for cylindrical grasps and a fourth grasping finger provides additional stability (Figure 2.9). The fingers attach to a hollow, square palm and are arranged such that common CATs can be grasped as required for EVA operations.

The SSL Hand utilizes a tendon drive system in combination with passive spring return. Actuators are not incorporated into the full design at the current developmental state. However, a modified leadscrew assembly was used for strength testing of the SSL Hand. Preliminary testing has shown its ability to firmly and stably grasp various tools used on EVA operations[4].

Chapter 3

Design Requirements

The primary objective for the design described in this thesis is to produce a robotic end effector capable of using EVA tools and interfaces. From the NASA-STD-3000 Man-Systems Integration Standards, “hand tools shall require an actuation force of less than 89N (20 lbs),” which defines the minimum required grasp force for the gripper design[15]. In addition, the end effector must be capable of grasping all EVA tools and have sufficient dexterity to manipulate the CATs and interfaces.

Most commercially available general use grippers have only one or two DOFs and thus are not suitable for the required tasks. Innovative non-anthropomorphic robotic hand configurations have yielded highly dexterous platforms capable of a wide range of grasps. This provides a balance between the complexity of a fully anthropomorphic and a simplistic low DOF design. However, as EVA tools are designed specifically for a suited astronaut hand, an anthropomorphic design provides a greater parallel for EVA compatibility. Matching human hand geometry also ensures that the end effector will be able to operate in the same workspace as the astronauts. The human hand has proven to be highly capable of both strength and fine motion, making it an ideal model for general use dexterous operations. Thus, an anthropomorphic approach was selected for the end effector design.

3.1 Human Hand Anatomy

In order to design an anthropomorphic hand, it is necessary to study human osteology and syndesmology to gain an understanding of how the human hand functions. The following section details the skeletal bone structure and joint types of the human hand. This basic anthropometric description provides a basis for the robotic hand design configuration and degrees of freedom.

The skeleton of the hand is divided into three groups: carpals, metacarpals, and phalanges. The carpal, or wrist, bones are eight in number arranged in two rows of four. The bones of the proximal row (that closest to the center of the body) are named the scaphoid, lunate, triquetrum, and pisiform. These bones connect to the two forearm bones, the radius (thumb side) and the ulna (little finger side). The distal row of bones (those furthest from the center of the body) are the trapezium, trapezoid, capitate, and hamate. These bones join with the five metacarpal bones that make up the palm, which connect on the other side to the digits. Fourteen phalanges comprise the five digits, giving a total of 27 bones in the hand. Each finger has three phalanges (proximal, middle, and distal) while the thumb has just two. The digits are typically referred to by the numbers I - V for the thumb, index, middle, ring, and little fingers respectively. Figure 3.1 details the individual bones and digit numberings.

A large set of freely movable articulations is formed by the connections of the bones in the hand. At the wrist joint where the proximal carpals interact with the radius in the forearm, is a condyloid articulation. In a condyloid joint,

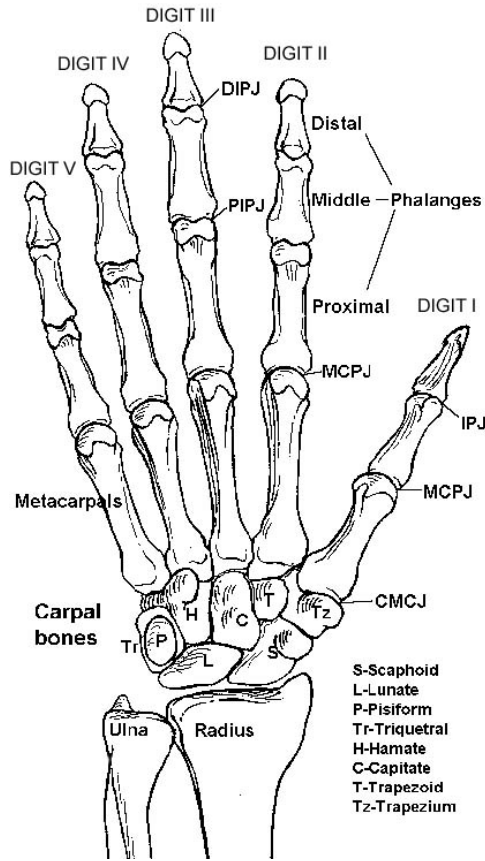


Figure 3.1: Bones and Joints of the Hand
<http://www.pncl.co.uk/belcher/handbone.htm>

the oval projection of one bone fits against the end of another bone and provides two DOFs. Thus, the wrist joint is capable of flexion and extension (forward and backward motion) as well as adduction and abduction (toward and away from the midline of the hand). The intercarpal articulations of the proximal and distal rows of wrist bones are arthrodial joints, allowing only for gliding motions between the bones. However, the mid-carpal joint where the two rows move with respect to one another has a combination of gliding joints and a cup-shaped cavity that creates a three DOF ball-and-socket type connection. Intercarpal motion is primarily in flexion/extension, but unlike the other carpal interactions, a very slight amount of rotation is also permitted.

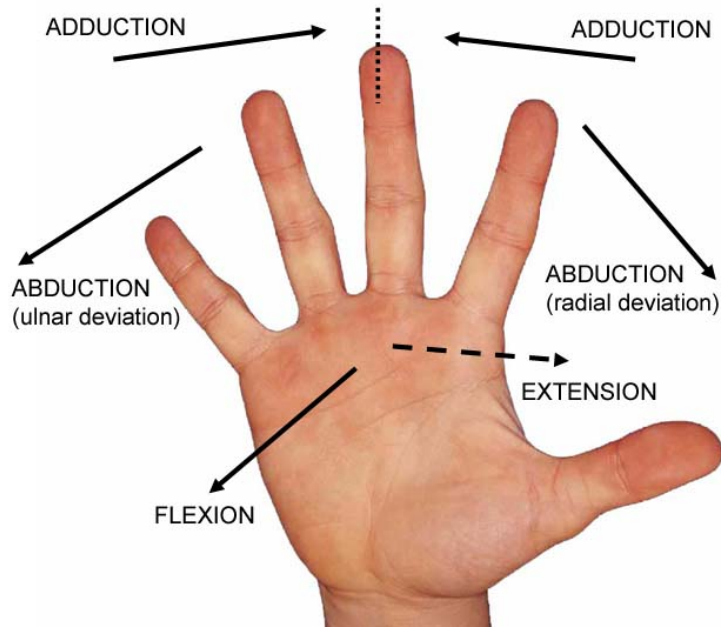


Figure 3.2: Direction of Joint Motion

Beyond the wrist bones are the carpometacarpal (CMC) articulations. The joints between the carpus and the II-V metacarpal bones are all arthrodiar. A small amount of gliding motion is permitted, increasing from index to the little finger. However, the CMC articulation of the thumb enjoys a great freedom of movement due to its configuration as a saddle joint. Saddle joints also allow two DOFs. In the case of the thumb CMC joint, movements permitted are flexion/extension in the palm plane and abduction/adduction in the perpendicular palm plane. For both saddle and condyloid joints, circumduction, where flexion, extension, abduction, and adduction movements are combined in sequence, is also possible. The geometry of the thumb CMC joint in relation to the rest of the hand provides opposition, one of the primary factors allowing for a wide variety of grasps.

The metacarpophalangeal (MP) joints exist where the metacarpals meet the proximal phalanges of the digits. For digits II-V, these articulations are condyloids

and permit flexion/extension as well as limited abduction/adduction. When the fingers are flexed, abduction and adduction cannot be performed. The thumb MP joint is more of a ginglymoid, or hinge, joint. Hinge joints only allow for flexion and extension.

Interphalangeal (IP) articulations are the final joints of the hand. As with the thumb MP joint, the IP joints are all hinge joints and only flexion/extension is permitted. The capability for flexion in these joints is much greater than extension. While the thumb has only a single IP joint, digits II-V have two separate articulations, the proximal (PIP) and distal (DIP) interphalangeal joint. The motion of these two joints are coupled together, as shown in Figure 3.3, with flexion at the PIP joint being more extensive than at the DIP joint of the same digit. The combined joints of the hand provide three DOFs per finger and four DOFs in the thumb for a total of 16 DOFs, outside of the wrist. Though the wrist does allow for some rotation, the amount is small enough that the human wrist is typically modeled as having two DOFs[16, 17].

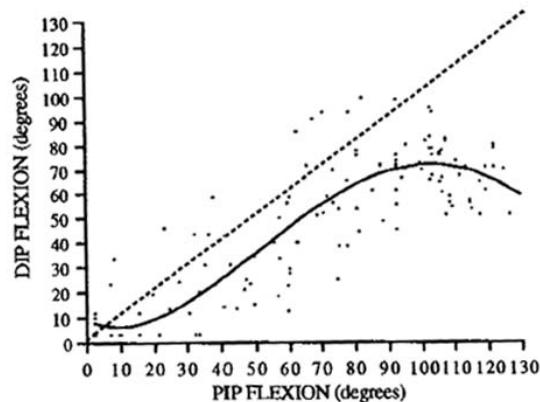


Figure 3.3: Relation Between PIP and DIP Flexion, Right Index Finger[5]

3.2 Anthropomorphic Requirements

3.2.1 Hand Sizing

Data from multiple existing anthropometric studies was compiled to determine human hand dimension requirements. The subjects of these studies included both males and females from various ethnic backgrounds. However, not all datasets provided the same set of measurements. Anthropometric data was therefore taken from only the most extensive study, that of American military males[18]. In addition, further measurements were taken for increased detail on finger geometry. Both left and right hands for 20 subjects were measured using the measurement chart shown in Figure 3.4. In addition to values defined in the chart, overall hand length and breadth were measured.

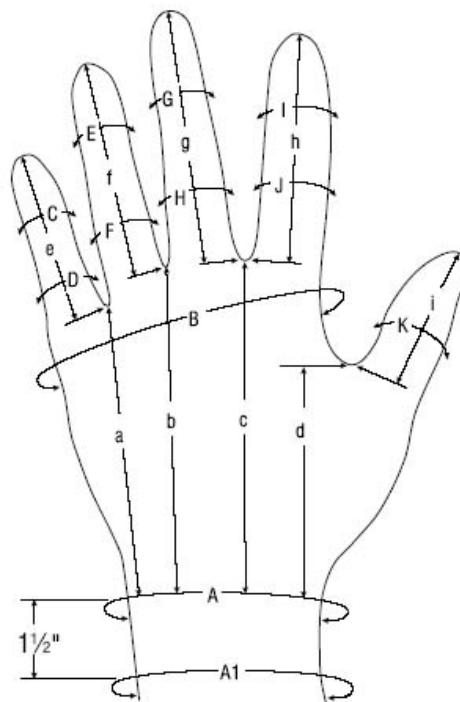


Figure 3.4: Bio-Concepts Hand Measurement Chart[6]

The desired geometry is based on an average American male. Given the EVA requirement, an upper bound on end-effector sizing is defined based on dimensions for a 95th percentile American male wearing an EVA glove. The envelope for an EVA glove over the hand was determined by comparing glove measurements to anthropometric data and defined as an increase of 35%. Based on the collaborated data, a basic sizing guideline was developed for the digits (Table 3.1). Although the dimensions for each digit differ on humans, a single set of measurements was determined for digits II-V for modularity. The thumb was not made modular to ensure proper opposition and fingertip interaction. Average and 95th percentile anthropometric dimensions used as the basis for sizing are detailed in Appendix A.

| | FINGERS II-V (in) | THUMB (in) |
|-------------------|-------------------|------------|
| WIDTH | 0.84 | 1.00 |
| THICKNESS | 1.14 | 1.00 |
| PROXIMAL PHALANGE | 1.37 | 2.00 |
| MIDDLE PHALANGE | 1.10 | 1.50 |
| DISTAL PHALANGE | 1.00 | 1.25 |

Table 3.1: Desired Sizing for Finger Design

3.2.2 Joint Range of Motion

In addition to the general structure, the range of motion in each joint must also be considered. Many hand designs target the approximate active range of motion for the finger joints (0-90°). However, the passive range allows for a much greater hyperextension of the DIP and MP joints. The increased range of motion can assist grip stability, particularly for pinch grips. Another consideration in an anthropomorphic design is the variation in joint motion between the four fingers.

Generally speaking, the range of motion for the MP and PIP joints increases and that of the DIP joint decreases from digits II-V. The difference in range of motion across the digits is greatest at the MP joint (approximately 25°) while the difference at the IP joints is less than 10° each.

Precise matching of human motion would require five separate sets of range of motion requirements for the digits. As with sizing, a single set of MP and IP joint range of motion requirements was defined for digits II-V to allow for modular fingers. The values for each joint and direction were taken from the maximums among the four digits. The thumb, which varies the most from the other digits in both size and motion, was again given a separate requirement set. The range of motion requirements for the digits and the wrist were derived from multiple anthropometric studies and are detailed in Tables 3.2 below[5, 19, 17, 20].

| DIGITS II-V | | | THUMB | | | WRIST | |
|-------------|-----------|---------|-------|-----------|---------|---------------------|---------|
| Joint | Direction | Degrees | Joint | Direction | Degrees | Direction | Degrees |
| MP | Flexion | 105 | CMC | Flexion | 45 | Flexion | 80 |
| | Extension | -30 | | Extension | 0 | | |
| | Abduction | 25 | | Abduction | 60 | Extension | -70 |
| | Adduction | -25 | | Adduction | 0 | | |
| PIP | Flexion | 110 | MP | Flexion | 56 | Radial Deviation | 20 |
| | Extension | -10 | | Extension | 0 | | |
| DIP | Flexion | 80 | IP | Flexion | 73 | Ulnar Deviation | -30 |
| | Extension | -20 | | Extension | -5 | | |

Table 3.2: Hand Range of Motion Requirements

3.3 Grasp Requirements

3.3.1 Grasp Classification

An empirical approach to studying grasping and manipulation uses natural systems as a model for robotic end-effectors. Currently, artificial hands are far from matching the capabilities of human and animal hands. Understanding how the human hand operates and manipulates objects provides a basis for mechanical design and deviation from anthropomorphism. In addition, research into grasp classification and manipulation behavior provides insight into grasp choice for different objects.

Early studies by Schlesinger (1919) in grasp taxonomy typically divided the human grasp into six types: cylindrical, fingertip, hook, palmar, spherical, and lateral. This categorization tended to associate grasps with object shape. However, in addition to shape, the desired task has great affect on the chosen grasp. Humans tend to modify grips to adapt to changing force and torque conditions. The concept of task dependent grasps led to Napier's classification of grasps as power or precision grasps. Power grasps typically involve large areas of contact and high stability. On the other hand, precision grasps fall into the realm of dexterous manipulation.

From this broader definition of grasp type, Cutkosky created a branching taxonomy that further subdivided the power and precision classifications into shape grips based on a wide range of manufacturing tool grips[21]. Previous work on EVA compatible hands at the SSL used the Cutkosky taxonomy to examine specific human grasp types used during EVA operations. Pilotte examined a sample Hubble

repair mission and found that the majority of operations involved heavy wraps, pinches, or used a bolt drive tool[22]. Further studies by Foster into grasps for EVA tools in general showed that about 90% of all CATs used either a cylindrical or three-finger grip. Using a knowledge-based approach, the hand design should thus be optimized for these primary expected grasp types and sizes.

3.3.2 Grasp Force Requirements

Necessary grip strength depends upon the type and size of the grasp. For the purpose of this design, the key grasps to consider are those necessary for EVA operations. These operations, which use an even distribution of precision and power grasps, can be broken down into three main grasp requirements: pinch, tripod, and cylindrical[22]. The cylindrical grasps in particular use a diameter ranging from 0.5 to 2.0 inches[4]. The minimum grip strength as defined by the preliminary design requirements should thus be considered in these particular conditions.

Actual grip forces of astronauts using EVA tools have not been studied. However, many existing studies have been performed on human strength in different grasp configurations. These studies can be used to extrapolate specific force requirements based on the NASA-STD-3000 EVA tool design requirements. Wraps, which account for over 50% of all CATs, are the strongest and most well studied of the grasp types. Humans are capable of exerting the largest forces, approximately 135 lbs, at $\varnothing 1.25''$. Beyond 1.25'', grip strength decreases as diameter increases.[23, 1, 2] To ensure the ability to use all CATs with cylindrical grips, the NASA-STD-3000

force requirement for maximum required tool actuation force is applied to the largest CAT diameter, 2.00".

Pinches represent the vast majority of the remaining tools. A study on hand strength found that on average, humans are only able to produce pinch forces at 25% their peak cylindrical grip capacity. The 20 lbs required wrap force strength thus corresponds to a minimum pinch strength requirement of 5 lbs.

3.3.3 Grasp Distribution

Grasp shape can also be used to estimate force requirements. Assuming a grasp geometry that approximates the human grasp, studies on force distribution for different grasps in humans can be used to understand phalange forces and calculate tendon forces. Force distribution in a cylindrical grasp is a well-studied subject and, as analysis of grasp classification has shown, a primary consideration for EVA tool usage. With the thumb held in opposition, the total grasp force is distributed over fingers II-V. Individual finger contribution remains consistent regardless of cylinder size and decreases from the index to the little finger. Table 3.3 below shows the force distribution over the fingers as found by two separate studies by Amis and Lee and Rim.

| FINGER | PERCENTAGE CONTRIBUTION | |
|------------|-------------------------|--------------|
| | Amis[1] | Lee & Rim[2] |
| FINGER II | 30% | 32.5% |
| FINGER III | 30% | 29.5% |
| FINGER IV | 22% | 22.6% |
| FINGER V | 18% | 15.4% |

Table 3.3: Force Distribution in Cylindrical Grip[1, 2]

In addition to distribution across the fingers, both studies also examined the separate phalange contribution for each individual finger. Both found that phalange distribution was consistent over all fingers and cylinder sizes. Table 3.4 displays the percentage values.

| PHALANGE | PERCENTAGE CONTRIBUTION | |
|----------|-------------------------|--------------|
| | Amis[1] | Lee & Rim[2] |
| PROXIMAL | 25% | 32% |
| MIDDLE | 25% | 18% |
| DISTAL | 50% | 50% |

Table 3.4: Force Distribution Over Phalanges in Cylindrical Grip[1, 2]

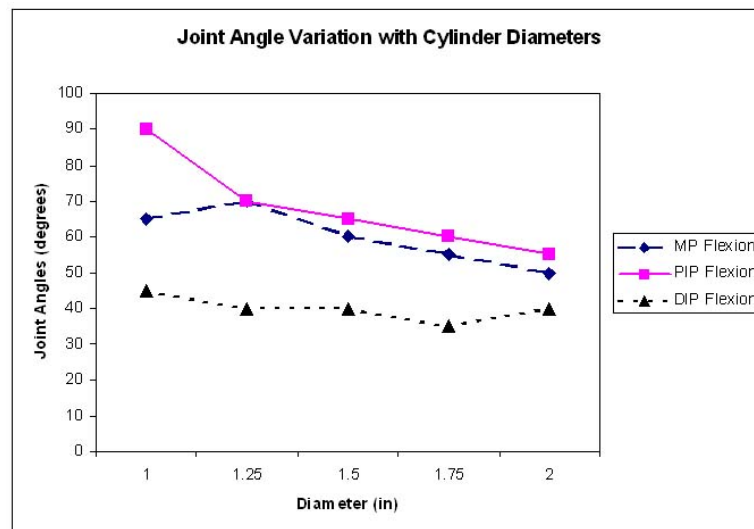


Figure 3.5: Finger joint angle flexion for varying cylinder diameters, averaged over digits II-V

For a full understanding of the cylindrical grasp, finger geometry must also be examined. Lee and Rim expanded upon the force distribution research to include a study on finger joint angles and force centers. They used markers and video analysis to compare the angles of the MP, PIP, and DIP joints over a range of cylindrical diameters from one to two inches. The greatest variation was seen in the PIP joint

| | LONG AXIS | | | TRANSVERSE AXIS | | |
|--------|-----------|--------|--------|-----------------|--------|--------|
| | PROXIMAL | MIDDLE | DISTAL | PROXIMAL | MIDDLE | DISTAL |
| INDEX | 0.51 | 0.74 | 0.47 | -0.14 | 0.02 | 0.02 |
| LONG | 0.59 | 0.65 | 0.44 | -0.03 | 0.08 | 0.11 |
| RING | 0.64 | 0.63 | 0.48 | 0.02 | 0.08 | 0.15 |
| LITTLE | 0.63 | 0.40 | 0.63 | 0.12 | 0.17 | 0.13 |

Table 3.5: Mean values of force centers
(long axis > 0.5 = distal, transverse > 0 = radial)[2]

while the DIP was consistently measured at around 40° for all fingers and cylinder sizes. Figure 3.5 details the average joint angle relationships for digits II-V. Force centers were measured along the long and transverse axes for each finger at each phalange. Mean values are displayed in Table 3.5.

3.4 Joint Torque Requirements

Based on the required grasp forces and estimated distributions, required joint torques were calculated for a cylindrical grasp. The maximum EVA tool diameter of 2.00 inches was used to determine hand geometry parameters (Table 3.6). The required 20 lb load distributed over the fingers and phalanges as described in the previous chapter results in the phalange forces shown in Table 3.7.

| | PROXIMAL | MIDDLE | DISTAL |
|------------|----------|--------|--------|
| FINGER II | 60° | 55° | 37.5° |
| FINGER III | 57.5° | 55° | 40° |
| FINGER IV | 55° | 52.5° | 40° |
| FINGER V | 37.5° | 47.5° | 37.5° |

Table 3.6: Hand Geometry for $\varnothing 2.00''$ Cylindrical Grasp

Assuming point forces at the phalange centers and a geometry as described previously, a force-moment analysis was performed on each finger to determine the

| | PROXIMAL | MIDDLE | DISTAL | TOTAL |
|------------|----------|--------|--------|--------------|
| FINGER II | 2.08 | 1.17 | 3.25 | 6.50 |
| FINGER III | 1.89 | 1.06 | 2.94 | 5.90 |
| FINGER IV | 1.45 | 0.814 | 2.26 | 4.52 |
| FINGER V | 0.986 | 0.554 | 1.54 | 3.08 |

Table 3.7: 20 lb Load Distribution (all values given in lbs)

| | DIGIT II | DIGIT III | DIGIT IV | DIGIT V |
|-----|----------|-----------|----------|---------|
| MP | 9.82 | 8.86 | 7.06 | 5.06 |
| PIP | 4.00 | 3.50 | 2.83 | 2.07 |
| DIP | 1.43 | 1.34 | 0.94 | 0.61 |

Table 3.8: Joint Torques for a 20 lb Cylindrical Grasp, $\varnothing 2.00''$
All values listed in lb-in

torques at each joint. The results are displayed in Table 3.8. The greatest torque, 9.82 lb-in, is seen at the MP joint of digit II. This value is used as the minimum required actuation torque per joint. In addition, the estimated torques are used in actuator selection, which will be expanded upon in Chapter 4. A fully detailed analysis can be found in Appendix A.

Chapter 4

Hardware Development

4.1 Hand Configuration

Each digit can be viewed as a separate serial manipulator. In order to implement a fully dexterous hand, the base of each digit must be configured within a palm structure to ensure grasp and manipulation capability. The palm design was simplified by grouping the fingers based on their primary functionality. The thumb in combination with digits II and III are treated as a dexterous set for manipulation. In the human hand, these three fingers are the strongest and have the greatest range of motion. As only three fingers are necessary for a stable spherical grasp and only one or two fingers necessary for the other primary grasp types, the dexterous set alone is sufficient for object manipulation. In order to simplify the palm, the two fingers are mounted at the same level. Digits IV and V provide additional stability and strength, in particular for cylindrical grasps. These two fingers are mounted lower than their dexterous equivalents.

An anthropometric parallel of the eight bones in the human wrist requires a densely packed and complex design. Wrist motion can be simplified down to two DOFs, abduction/adduction and flexion/extension, with minimal loss of functionality for the overall wrist. However, the range of bend in the CMC joints increases from finger II - V in the human hand. This aids in motions of opposition, in par-

ticular cupping motions and the contact of pinky to thumb. In order to simplify the palm and wrist design, the individual CMC joints are combined in with the two overall wrist joints. As a result, fingers II - V can move only in the palmar flexion/extension and abduction/adduction planes. To ensure sufficient range of motion in opposition, the thumb is mounted at a 90° angle to the palm, thus moving in a plane angled to that of the other fingers. In addition, the lower mounting point of the grasping set increase reachability in opposition.

4.2 Finger Skeletal Structure

Each finger in the human hand has the same kinematic arrangement - a two DOF joint followed by two single DOF joints in serial. For modularity, all five fingers use the same joint design. The thumb differs from the other four fingers only by the phalange sizes. In most previous designs, the IP joints are pin joints either individually controlled or mechanically coupled together, often by a four-bar linkage. By using this type of coupling, it is easy to know the behavior of one joint in relation to the other. However, coupled pin joints are both highly complex to package in the confines of a small finger and typically lack the ability for motion in extension.

4.2.1 Compliant Mechanism Development

An alternative to coupled pin joints for the finger framework is the use of compliant mechanisms. Compliant mechanisms use the deflection of flexible members

rather than movable joints to gain mobility. This allows for several cost and performance advantages. The greatest benefit is the significant reduction in part count, which may reduce assembly time, simplify the manufacturing process, and reduce total cost. Compared to traditional rigid-body mechanisms, compliant mechanisms have fewer movable joints, such as pin and sliding joints. The subsequent reduction in wear and need for lubrication is a valuable benefit for the limited accessibility and harsh environment of an EVA application. Compliant mechanisms also have the advantage of weight reduction and relative ease of miniaturization. For a finger design, the use of a compliant piece could replace the entire skeleton of the finger with a single component. In addition, the inherent compliance increases the potential range of motion in both extension and flexion and lends itself to applications needing delicate manipulation.

Several challenges and disadvantages exist with compliant mechanisms as well. The primary difficulty is accurate analysis and modeling. Due to the large deflections of flexible members, linearized beam equations do not account for the geometric nonlinearities. Many early compliant mechanisms were designed based on trial and error approaches to circumvent these difficulties. However, recent theory has been developed to simplify the analysis and design.

Another challenge is fatigue failure and component strength, particularly for large angle deflections. Compliant mechanisms are more often applied in small angle deflections to better balance the trade-off between member strength and material flexibility. Large angle applications are more likely to face shorter fatigue lives as increased range of motion is limited by the strength of the deflecting members.

While a compliant link can not rotate 360° continuously as is possible with a pin joint, the requirements of the finger design require only limited large angle deflection. This makes the use of compliant mechanisms possible and may reduce the problems with fatigue life. Despite the analytical challenges, the use a compliant piece for the finger framework was chosen to reduce overall design complexity and weight[24].

Material selection is the first step to compliant mechanism development. For a rectangular cross section, the maximum deflection of the free end, δ_{max} , is given by:

$$\delta_{max} = \frac{2 S_y L^2}{3 E h} \quad (4.1)$$

where S_y is the yield strength, E is the Young's modulus, L is the length of the flexible member, and h is the thickness. Thus, the material that will allow the largest deflection before failure is that with the highest ratio of strength to Young's modulus. Although metals generally provide more predictable material properties and fatigue life, they also have low strength-to-modulus ratios compared to polymers. As this particular application requires a large angle of deflection, metals were not considered for compliant mechanism design. Among plastics, polypropylene is a commonly used polymer in compliant mechanisms. It has a very high strength-to-modulus ratio and is also both readily available and inexpensive. Polypropylene is also very ductile, which makes catastrophic failure less likely when yielded. For these reasons, polypropylene was chosen as the skeletal material for the finger design.

Using the material properties of polypropylene and the calculated moments

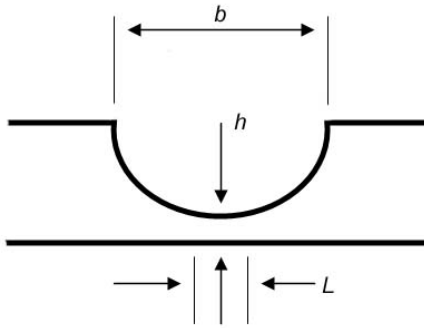


Figure 4.1: Cross section of compliant hinge

and forces, dimensions for the flexible member were calculated. To minimize buckling problems, a curved cut was selected for the compliant hinge. The use of the curved cut gives a small flexible member length while still allowing a wide range of flexure without interference. Based on machining capabilities, the member length was set at 0.0625 inches. The width was also preset based on hand sizing requirements to be 0.7625 inches. From the previously calculated maximum moment and polypropylene material properties, the thickness was calculated to be 0.03 inches.

4.2.2 MP Joint Design

The MP joint is often approximated by two pin joints mounted perpendicularly in series. However, a more accurate mechanical model of the human MP joint is a universal joint. Rather than having two separate pin joints, a universal joint allows for intersecting axes of rotation. While it is possible to design a two DOF compliant mechanism, strength and failure concerns are greater at the MP joint than the IP joints. The MP joint serves as the attachment point to the palm and typically sees the largest forces. A modified universal joint of aluminum, shown in an exploded

view in Figure 4.2 was thus designed to mount within the palm design and attach to the compliant framework.

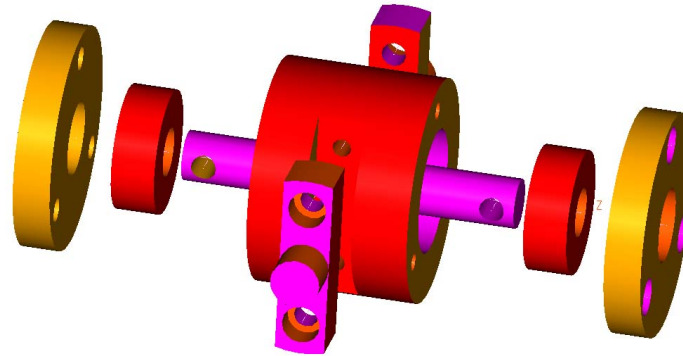


Figure 4.2: Exploded View of MP Joint



Figure 4.3: Assembled MP Joint

The joint consists of a central hub containing two bushings to support the pitch shaft. The pitch shaft runs through the hub and connects on both ends to the rest of the finger structure, providing motion in the flexion and extension. In order to make the components more easily machinable, two yaw shaft pieces attach to the

hub instead of being integrated into a single hub piece. The yaw shaft components are supported in the palm structure and provide for abduction/adduction motion. Figure 4.3 shows the manufactured and assembled MP joint components with a quarter for size comparison.

4.2.3 Phalange Connection

In the original prototype design, the compliant piece linked to the MP joint by means of external shell components. The external casings, intended to be manufactured by rapid prototype, were simple block pieces that bolted directly to the phalange links. The proximal phalange blocks also attached to the flexion shaft of the MP joint by set screws. Internal cable routing was integrated into the shells. This particular design had several drawbacks. The structure of the finger was dependent upon the proximal phalange shells used to connect the compliant shaft to the MP joint. Due to the material, method of manufacturing, and thickness of the pieces, the shells have several weak points that make it a less than ideal structural member. In addition, difficulties with producing parts on the rapid prototype machine made it less desirable to use it to produce structural members. The simple block design of the initial external casings also resulted in large gaps on the external phalange surface to allow for full range of motion. The decrease in grasping surface and increase in internal component exposure to the environment is undesirable.

The second version of the finger design attaches the compliant component directly to the flexion shaft of the MP joint. This creates a base skeleton of links

and joints, leaving the shell pieces serving purely as external casings. Two shells, split into radial and ulnar halves, are used at each phalange. Instead of the simple blocks, the modified components fit together with those of the adjacent phalange in a pin joint fashion. Varying the width over the length of the external shell also allows for greater coverage of the finger surface while still preserving the full range of motion. The ends of the middle phalange fit into the ends of the distal and proximal phalanges. Using this overlap, the components are cut to provide hard stops at the ends of the joint ranges of motion. This design provides greater stability to the overall structure and is more anthropomorphic in geometry. An exploded view of the final phalange and skeletal design is seen in Figure 4.4. An assembled view including the MP joint hub (excluding the palm connection) is shown in Figure 4.5.

A cable routing groove is cut along the interior of the phalange shell components. PVC tubing sits inside this groove, providing a protective sheath through which the cable can run smooth. Steel pins integrated into the distal and proximal phalanges serve as termination points.

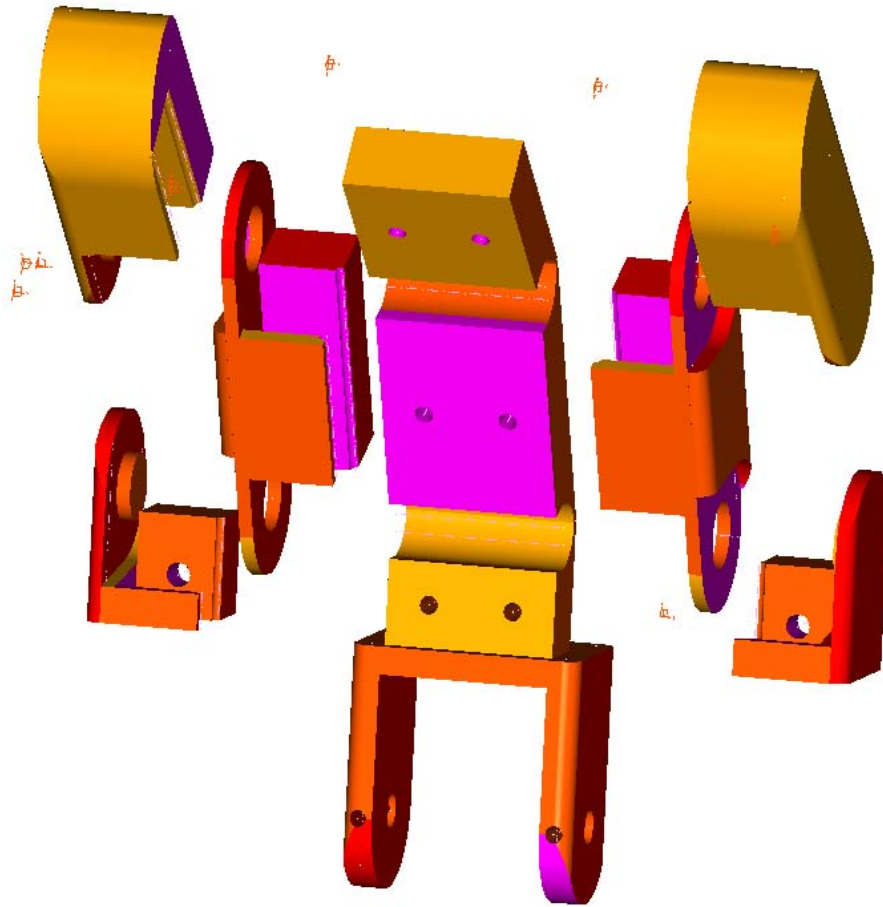


Figure 4.4: Exploded View of Finger

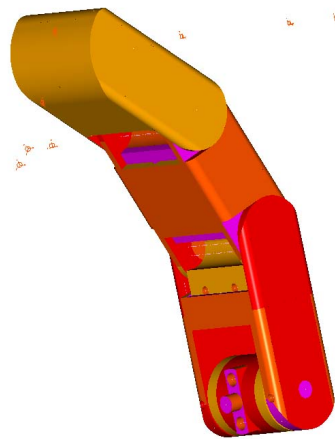


Figure 4.5: Full Finger Assembly (palm not shown)

4.3 Actuation System

4.3.1 Actuator Type Selection

Several different options for actuators were considered for the design. The application and packaging constraints require consideration of the trade-offs between weight, size, and power. In addition, availability of components was a primary factor in final actuator selection. The following sections describe the main actuator types considered.

McKibben muscles (air)

McKibben artificial muscles, also known as air muscles or fluid actuators, are pneumatic actuators that behave in a similar fashion to real human muscles. An individual McKibben device consists of an expandable internal bladder surrounded by a braided sheath. When inflated with compressed air at low pressure, the internal bladder expands against the sheath. The sheath acts to constrain the expansion, thus causing the overall length of the actuator to shorten.

McKibben muscles provide a high strength to weight ratio and advantages with compliance and packaging. Because of the compressibility of their energy source, air, McKibben muscles demonstrate compliant behavior. Additional compliance is seen as a result of the dropping force to contraction curve, rendering spring-like behavior. This inherent compliance provides benefits for man-machine interactions and applications where a soft touch for delicate operations is desired. Another advantage is the flexibility of the actuator that makes it a rugged component. McKibben

muscles will work when twisted axially, bent around a corner, and do not require precise aligning. From a packaging standpoint, this eases the requirement to fit a high number of actuators in the small volume of the forearm.[25]

Despite their benefits, McKibben muscles present a challenge for use in an EVA environment. Outside of the general problem of using pneumatics in EVA operations, the added requirement for a compressor is a drawback. While the actuators themselves can be packaged in a small space, a compressor and air source add weight and a large external component.

Shape Memory Alloys & Electroactive Polymers

Increasingly complex designs, particularly for humanoid robotics and space mechanisms, face growing mass, power, size, and cost constraints. To satisfy these demands, ongoing research examines the use of smart materials as actuators. The current leading alternative actuators are shape memory alloys (SMA) and electroactive polymers (EAP).

An SMA is a metal that can return to its original shape when heated. This behavior is a result of the reversible crystalline phase transformation that occurs between the low temperature (martensite) and high temperature (austenite) phases. Austenite and martensite are identical in chemical composition, but have different crystallographic structures. When an SMA is deformed in martensite, the residual strain can be recovered by heating the material to the austenite phase. This shape memory effect returns the SMA to its original shape[26].

The use of SMAs as actuators has many potential advantages and disadvantages. SMAs exert a large force against external resistance during the martensite-austenite transformation, thus providing a high strength-to-weight ratio. By training the material, both the high temperature and low temperature shapes can be recalled. The two-way shape memory effect behavior makes SMAs a viable option for robotic actuators. However, precise regulation of position is still a challenge due to the hysteresis associated with the phase transformation. In addition, SMAs tend to have a slower speed of actuation, making its use in high bandwidth control applications difficult[27, 26].

Another alternative actuator is the electroactive polymer. Over the past several years, the use of EAPs as artificial muscles has received increasing attention. EAPs are polymers that respond to an applied voltage with displacement and can be used as both actuators and sensors. They are light weight with high compliance, have a fast response time, can be produced at a low cost, and have superior fatigue characteristics to SMAs. Researchers have designed EAPS to emulate biological muscles in robotic arms as well as studied their application in the space environment for various mechanisms and actuation tasks. The performance capabilities of these polymers make it a promising candidate for inexpensive, low mass, low-power consuming actuators. However, EAPs can only handle small forces, significantly less than SMAs[28, 29, 30].

Commercially available SMAs and EAPs are difficult to find. In addition, SMA performance speed is too slow to match human motion and EAPs lack the strength capabilities desired. Though novel in concept and attractive from a pack-

aging perspective, the primary factors in consideration for actuator type make SMAs and EAPs undesirable.

DC Motors

DC motors, the final type of actuator considered, are a proven technology with widespread use in a large range of applications. Although by far the heaviest and bulkiest of the actuators discussed, they also have high speed and strength capabilities and are commonly commercially available. In addition, brushless DC motors are often used successfully in space applications. The vast majority of hand designs to date have used some form of motor and the Robonaut hand, the only current hand designed for EVA operations, uses brushless motors. DC motors thus provide a proven, readily available platform capable of matching the required performance standards and were therefore chosen as the actuator for the hand design. Table 4.1 summarizes the discussed actuator performances.

| | MCKIBBEN | SMA | EAP | DC MOTOR |
|--------|---------------------------------------|---|---------------------------|-------------------------------------|
| Size | $\varnothing=6-30mm$ $l=150-290mm$ | $\varnothing=0.018-32mm$ $w=0.013-0.410mm$ | | $\varnothing=6-44mm$ $l=20-90mm$ |
| Weight | 10-80g | 3-4oz/in ³ | 0.5-1.5oz/in ³ | 2.5-750g |
| Force | 7-70kg | 700MPa | 0.1-3MPa | |
| Speed | sec | sec to min | μ sec to sec | μ sec to sec |

Table 4.1: Comparison of Actuator Types

The simplest design would use a direct drive, placing motors locally at pin joints. This approach presents a challenging packaging problem and does not lend itself to the compliant mechanism choice. Another option is to remotely locate the motors and use a tendon system to actuate the joints. In addition to easing

packaging problems, it is also easier to protect the drive components in the remote drive box. This approach, both similar to the way human muscles work and the basis for many previous hand designs, was chosen to actuate the finger joints. The motors are housed in the forearm and connect to a leadscrew, which converts the rotary motion of the motor to linear tendon motion.

4.3.2 Tendon Forces and Motor Selection

Component selection depends upon the expected tendon forces at the maximum grasp force. From the joint torques determined in Chapter 3, tendon forces can be calculated based on attachment point geometry. Figure 4.6 shows the relationship between attachment point distance from the joint and maximum tendon force. For the previously determined curvature of the compliant mechanism, a 0.25" distance allows for full desired range of motion without interference at a maximum calculated tendon force of 39 lbs.

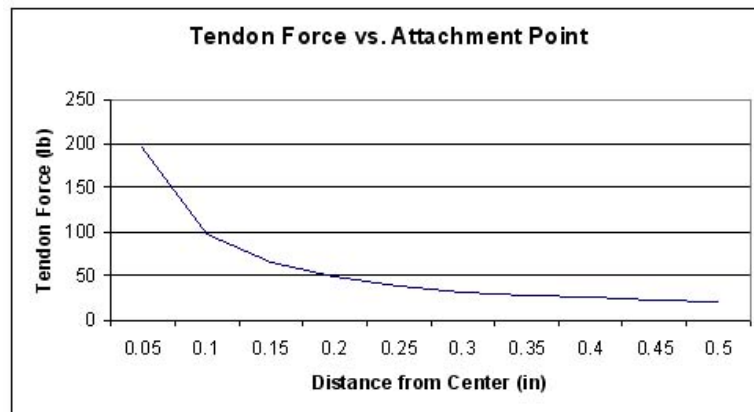


Figure 4.6: Projected Actuation Tendon Forces

This analysis neglects any friction effects in the tendon lines or impediments

to the compliant motion. Previous work at the Space Systems Lab utilized a tendon driven compliant skeleton embedded within a foam hand mold as an EVA glove test stand[31]. While this study investigated pressures on the hand, the setup can also be used to experimentally test tendon forces in a high friction compliant arrangement. The design utilizes six individual tendons to actuate the five fingers and a palm DOF. Due to the foam encasement, the compliant mechanism actuation is significantly hindered. Measurement of tendon forces in this setup provides a worst-case approximation of actuation requirements for a compliant framework.

Two separate test cases were run. The first measured the unweighted actuation force. The original test stand utilized guitar tab tuners to pull on each individual tendon. In order to measure the tendon forces, the stand was modified and the guitar tabs were removed and the tendons were extended. Using a Shimpo digital force gauge, each tendon was pulled until the corresponding finger was fully bent in. Table 4.2 shows average peak and holding forces for each tendon.

| | PALM | LITTLE | RING | MIDDLE | INDEX | THUMB |
|--------------|------|--------|------|--------|-------|-------|
| Peak (lb) | 12.5 | 9.25 | 8.84 | 10.2 | 9.97 | 8.33 |
| Holding (lb) | 10.4 | 8.44 | 7.39 | 9.33 | 9.12 | 7.98 |

Table 4.2: Peak and Holding Forces for Unweighted Setup

Tendon forces were also measured under load. The test stand was mounted in an inverted position and a cylindrical bar positioned within the closed grasp of the hand. Total load of the bar was increased in two-pound increments by hanging additional lead weights from the bar. Given the cylindrical grasp shape, only tendon forces for fingers II-V were measured. The set curvature of the compliant framework

design made it unable to hold weights beyond eight pounds without slipping. Results for the four tendons are plotted below.

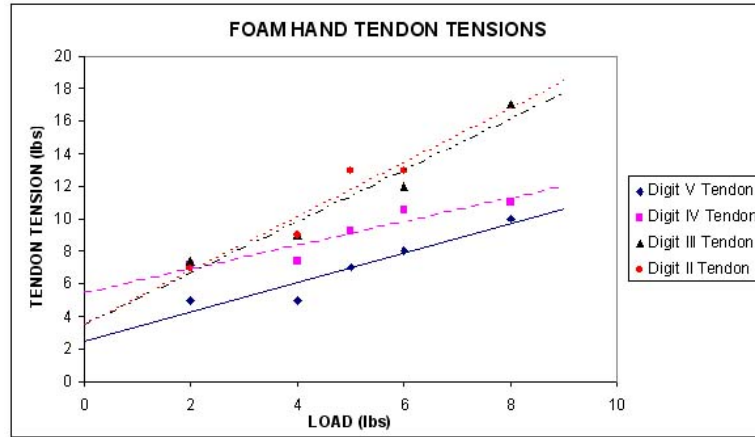


Figure 4.7: Experimentally Derived Tendon Forces

A notable outcome is the force distribution between the four fingers. Given the anthropometric design, the distribution behavior appears to approximate the expected anthropometric distribution. Applying a linear regression analysis on each of the four data sets gives the trendlines seen in Figure 4.7. Projecting to the maximum input load of 20 lbs based on these trendlines results in tendon forces of 36.7, 35.2, 19.9, and 20.6 lbs for fingers II - V respectively. This experimental result corresponds with the calculated forces, thereby establishing the minimum required tendon force.

4.3.3 Component Selection

PowerPro Superline, made of braided Spectra fiber and rated for 100 lbs, was selected for the tendon lines. The weight-to-strength ratio of Spectra cable is ten times stronger than steel wire, allowing for a reduction in wire diameter and weight.

A fiber-based cable is also more easily routed around small radii than metal wire. The PowerPro line, intended for fishing, functions well in wet, harsh environments and has near zero stretch. This particular line is braided, giving it added resistance to abrasion.

The tendons attach directly to the leadscrew nut, which thus requires a component capable of handling the minimum required tendon force. A $\frac{1}{4}$ " B-Series Kerk Motion lead screw assembly with a 50 lb load rating was selected. Torque, power, and speed calculations were used to select a lead length. The required motor torque to drive a lead screw assembly is given by Equation 4.2.

$$T_L = \frac{\text{Load} \times \text{Lead}}{2\pi \times \text{Efficiency}} \quad (4.2)$$

$$\text{rpm} = \frac{\text{linspd}}{\text{Lead} \times 60} \quad (4.3)$$

$$P = T_L \times \text{rpm} \times 0.00074 \quad (4.4)$$

According to the data specifications from Kerk Motion, the optimum traveling speed for a nut along a leadscrew with a lead less than $\frac{1}{2}$ " is 4 in/sec. Motor power to move the desired load was calculated using Equations 4.3 and 4.4. As lead length decreases drive torque also decreases. However, required motor power increases exponentially. Plotting both T_L and P versus lead shows that a lead of 0.118" lies both at the knee of the power graph and before a large jump in the torque graph. This was thus the chosen lead length.

A motor/gearbox combination was then selected to drive the chosen lead screw. This is an iterative process. Starting with the required output torque and sizing

restraints, a gearhead is initially selected. Dividing the maximum available motor input speed for a potential gearhead by the desired output speed gives the theoretical reduction ratio. A ratio equal to or less than the theoretical is chosen and multiplied by the desired output speed to get the actual input motor speed. The new input torque requirement is then given by:

$$M_i = \frac{M_o}{i \times \eta} \quad (4.5)$$

where η is the gearhead efficiency, i is the reduction ratio, M_i is the input torque needed, and M_o is the required output torque specified. A compatible motor is then selected that is capable of providing the necessary torque, power, and speed. This process was repeated for several potential motor/gearbox combinations. A Faulhaber Series 23/1 Gearhead with a Series 2342 012 CR motor was chosen for the design. For detailed calculations, see Appendix A.

4.3.4 Packaging

For the selected actuation method of tendon driven joints using motors and leadscrews, packaging is a significant challenge. The motor leadscrew assemblies must be fully encased within the space of the forearm and cable routing must ensure smooth tendon motion avoiding sharp corners and exposure to elements that may damage the cables. In addition, the trade-off between active actuation with increased control capability and passive actuation for packaging and weight is a significant issue.

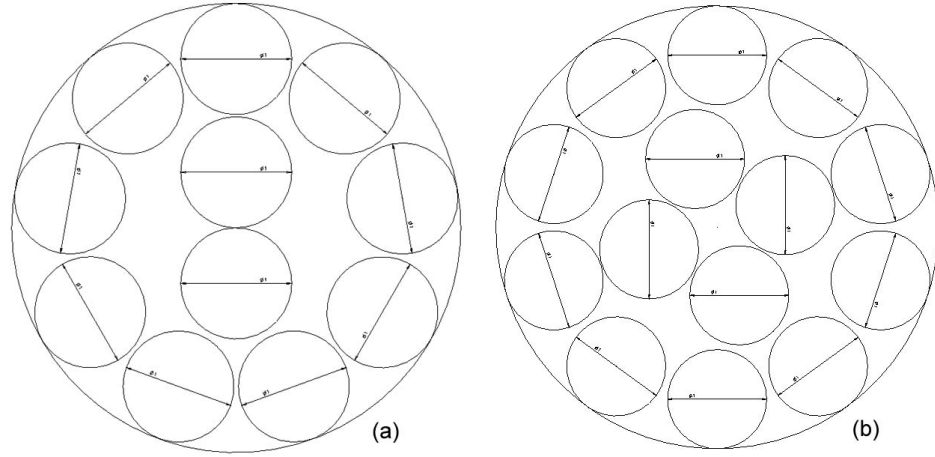


Figure 4.8: Actuator Packaging in Forearm

For the average male forearm diameter, a maximum of 11 actuator assemblies can be packaged (Figure 4.8a). However, the overall length can fit two assemblies, with proper cable routing. This gives a total of 22 actuators, four more than the total number of DOFs in the fingers and wrist. Increasing the forearm diameter to that of the 95th percentile male (Figure 4.8b), the housing fits 14 actuator assemblies in a single layer and 28 total.

4.3.5 Passive vs. Active Actuation

A key concern in the development of the actuation system was the trade-off between passive and active actuation. The human hand operates using opposing muscle pairs to actuate a single joint. This type of active opposition in a robotic design has the potential benefit of increasing dexterous capability, particularly in regards to speed and small force interactions. However, using active opposition instead of passive return requires doubling the number of actuators, exacerbating

packaging and weight issues. For the fingers and wrist combined, this increases the number of actuators from 18 to 36, all of which are ideally packaged within the forearm. Packaging enough actuators for antagonistic pairs at every joint requires increasing the forearm radius to 2.25 inches, a 12% increase over the 95th percentile measurement. This fits within the EVA glove envelope restriction of 30%.

No previous hand design allows for active antagonism in all the joints of the fingers. Typically, the joints are actuated in one direction and use a constant spring return. Both the Shadow hand and the Robonaut hand use opposing actuator pairs for the abduction/adduction motions, but only one actuator for the flexion component of the other joints. Compliance can be introduced on the control level through software. However, implementing compliance at a mechanical level creates an intrinsic, adaptable behavior that helps ensure system safety. In addition, different spring constants can be modeled in the system, increasing the potential complexity of control. The opposing tendon forces can also be used to exert some degree of control over the two separate IP joints that are coupled together. While a rigid four-bar linkage allows for only one grasp shape of each finger, the compliant joint together with an antagonistic actuation system can better fit its grasp shape to the object[32].

4.4 Sensors

Tendon sensors were chosen and integrated into the actuator assembly design. Selection and integration of other sensors, including joint position and tactile feed-

back, were beyond the scope of this thesis. However, consideration of sensor type and placement are presented in the following section.

4.4.1 Position and Force Sensing

Motor encoders can be used in combination with the leadscrew and hand geometry to determine joint position. However, the compliance of the framework and potential slop in the tendons creates a large potential for errors. A preferred system would measure joint angles directly. Bend sensors provide reliable feedback and can be laid over the IP joints on the surface of the framework. Integration of these sensors around the MP joint to measure abduction/adduction presents a design difficulty. Previous experience with bend sensors at the Space Systems Lab suggests that bend sensors are not sufficiently robust to be packaged in such a tight manner.

Fiber optic based joint angle sensing has been studied at the Space Systems Lab and can be found as an off-the-shelf unit from Fifth Dimension Technologies (5DT). The 5DT system is a glove with 14 sensors capable of measuring the bend at each of the IP joints as well as the abduction between fingers. While this glove-based system is easily integrated, it is unable to measure the bend at the MP joint. An alternative sensing solution would also be needed to measure wrist motion.

Hall Effect sensors, found in many other robotic hand designs, are the most viable option for joint position sensing. These sensors are small in size and can be easily integrated within the framework such that they are protected from the

external environment. The main disadvantage to this system is that operation in a strong magnetic field can produce errors. While the design of the position sensing system is outside the scope of this thesis, future development must minimize sensitivity.

Several load cells were considered to measure tendon forces. The selected sensor was the LC201 subminiature tension/compression load cell, manufactured by Omega[33]. This load cell has a 50 lb load capacity with resolution of 0.10 lbs. The size and shape makes this sensor well suited for the application. At $\varnothing 0.75 \times 1.03''$, this load cell can fit inline with the tendon assembly without requiring more room axially than the leadscrew itself.

4.4.2 Tactile Sensing

Previous work at the space systems lab utilized FlexiForce single-element load sensors for pressure sensing applications. These sensors provided a highly economical solution for discrete point sensing. For initial testing, the FlexiForce components could be integrated to provide sensing data on each phalange and within the palm[34]. Operating on a similar principle is the FingerTPS system, a sensor suite designed specifically for fingertip force measurement. FingerTPS is capable of up to eight discrete sensing points per hand[35].

Large, single-point sensors are sufficient for power grasps and low-dexterity applications. However, a distributed tactile sensor system is a better analog to human capability and is necessary for high-level manipulation control. For applications

requiring high dexterity and particularly soft touch interactions, multiple tactels per contact surface are desired. Stretchable, conformable tactile array systems are commercially available and can be used to create a skin around the outer shell of the mechanical design. Although the use of such a skin would increase dexterous ability, a key consideration is the greater complexity of the control problem.

Chapter 5

Kinematics Analysis

5.1 Finger Kinematics

5.1.1 Forward Kinematics

Solving the forward kinematics problem relates a system pose to the position and orientation of the end effector. Though several methods exist to describe mechanisms, the analysis presented uses methods put forth in Craig[36]. This method utilizes Denavit-Hartenberg (DH) parameters to describe the links and connections. The change from joint space to Cartesian space is executed by constructing a transformation that defines the tool tip frame relative to the base frame. This transformation is a function of the four DH parameters and is derived by examination of the mechanism kinematic structure.

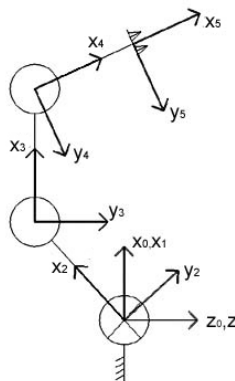


Figure 5.1: Kinematic Structure of Individual Finger

The kinematic layout of an individual finger with frame assignments is shown in Figure 5.1. The corresponding DH parameters are listed in Table 5.1 where l_p , l_m , and l_d are the proximal, middle, and distal phalange lengths respectively.

| i | α_{i-1} | a_{i-1} | d_i | θ_i |
|-----|-----------------|-----------|-------|------------|
| 1 | 0 | 0 | 0 | θ_1 |
| 2 | $\frac{\pi}{2}$ | 0 | 0 | θ_2 |
| 3 | 0 | l_p | 0 | θ_3 |
| 4 | 0 | l_m | 0 | θ_4 |
| 5 | 0 | l_d | 0 | 0 |

Table 5.1: Denavit-Hartenberg Parameters for Finger

The general form of the transformation matrix, shown in Equation (5.2), uses these link parameters to define frame $\{i\}$ relative to frame $\{i-1\}$. By the matrix structure, the 3 x 3 rotation matrix, ${}^{i-1}_iR$, and the 3 x 1 translation vector, ${}^{i-1}_iP$, can also be determined.

$${}^{i-1}_iT = \begin{bmatrix} \cos \theta_i & -\sin \theta_i & 0 & a_{i-1} \\ \sin \theta_i \cos \alpha_{i-1} & \cos \theta_i \cos \alpha_{i-1} & -\sin \alpha_{i-1} & -\sin \alpha_{i-1} d_i \\ \sin \theta_i \sin \alpha_{i-1} & \cos \theta_i \sin \alpha_{i-1} & \cos \alpha_{i-1} & \cos \alpha_{i-1} d_i \\ 0 & 0 & 0 & 1 \end{bmatrix} \quad (5.1)$$

$$= \begin{bmatrix} {}^{i-1}_iR & {}^{i-1}_iP \\ 0 & 0 & 0 & 1 \end{bmatrix} \quad (5.2)$$

The individual link-transformation matrices are then computed using the DH parameters. Multiplying these link transformations together gives the final transformation from the base frame, 0, to the tool frame, N .

$${}^0_N T = {}^0_1 T {}^1_2 T {}^2_3 T \dots {}^{N-1}_N T \quad (5.3)$$

5.1.2 Inverse Kinematics

Solving the inverse kinematics problem computes the set of joint angles needed to achieve a desired position and orientation of the tool tip. This problem is more difficult than the forward kinematics problem and raises the concerns of solution existence as well as the possibility of multiple solutions. Two general methods of solution used in robotics are closed-form, or analytical, and numerical solutions. The inherent iterative nature of numerical solutions make it significantly slower than analytical methods. For many applications, a closed-form solution is thus highly desirable.

Whether a solution exists is first a question of whether the desired end point is within the manipulator's reachable workspace. Individual joint range of motion limits the workspace. In addition, the finger manipulator has only four joints and is therefore unable to achieve general goal positions and orientations. In order to characterize the attainable subspace, an orientation constraint is considered. As seen in Figure 5.1, the x-axis of the tool frame lies in the vertical plane of the arm that contains the frame origins. The nearest attainable orientation for a general goal orientation is found by rotating the tool point to lie in the arm plane.

For a desired tool position in the base frame, p , with x, y, and z components p_x , p_y , and p_z , the vector normal to the arm plane, \hat{M} , is defined as

$$\hat{M} = \frac{1}{\sqrt{p_y^2 + p_z^2}} \begin{bmatrix} 0 \\ p_y \\ p_z \end{bmatrix}$$

Given the desired pointing direction, \hat{X}_T , of the tool, a new pointing direction, \hat{X}'_T , that lies in the arm plane is found by rotating by some angle, θ , about some vector, \hat{K} . \hat{K} is then given by

$$\hat{K} = \hat{M} \times \hat{X}_T$$

and the new pointing direction is

$$\hat{X}'_T = \hat{K} \times \hat{M}$$

The amount of rotation is determined from

$$\cos \theta = \hat{X}_T \cdot \hat{X}'_T$$

$$\sin \theta = (\hat{X}_T \times \hat{X}'_T) \cdot \hat{K}$$

and \hat{Y}'_T is found using Rodriguez's formula.

$$\hat{Y}'_T = \cos \theta \hat{Y}_T + \sin \theta (\hat{K} \times \hat{Y}_T) + (1 - \cos \theta) (\hat{K} \cdot \hat{Y}_T) \hat{K}$$

The final column of the new rotation matrix of the tool is determined by the cross product

$$\hat{Z}'_T = \hat{X}'_T \times \hat{Y}'_T$$

Given the general goal orientation projected into the manipulator subspace, the kinematic equations can then be solved analytically using both algebraic and geometric approaches. For link lengths of l_p , l_m , and l_d for the proximal, middle,

and distal phalanges respectively, the joint angles are given by

$$\begin{aligned}\theta_1 &= \text{atan2}\left(\frac{p_y}{p_x}\right) \\ \theta_2 &= \begin{cases} \beta + \alpha & \text{if } \theta_3 > 0, \\ \beta - \alpha & \text{if } \theta_3 < 0 \end{cases} \\ \theta_3 &= \cos^{-1}\left(\frac{p^2 - l_p^2 - l_m^2}{2l_p l_m}\right) \\ \theta_4 &= \phi - \theta_2 - \theta_3\end{aligned}$$

where p_x , p_y , and p_z are the x, y, and z components of the desired position, ϕ is the desired orientation of the tool and

$$\begin{aligned}p &= \sqrt{p_x^2 + p_z^2} \\ \beta &= \text{atan2}\left(\frac{p_x}{p_z}\right) \\ \alpha &= \cos^{-1}\left(\frac{p^2 + l_p^2 - l_m^2}{2l_p p}\right)\end{aligned}$$

From this derivation, it is apparant that a solution will not exist where $p_x = 0$ or $p_z = 0$. Multiple solutions may exist for θ_3 where the positive computed cosine is less than the absolute value of the extension joint limit. In this case, two solutions will exist when

$$\cos^{-1}\left(\frac{p^2 - l_p^2 - l_m^2}{2l_p l_m}\right) \leq \pm 10^\circ$$

A corresponding dual solution exists for θ_2 as well. For a detailed derivation of the inverse kinematic equations, see Appendix C.

5.1.3 Velocities and Static Forces

Expanding the analysis beyond static positioning leads to the examination of manipulator motion as well as static forces. The velocity of any link $i + 1$ is that of link i plus the new velocity components added by joint $i + 1$. Applying Equations (5.4) and (5.5) successively from link to link, the linear velocity, ν , and angular velocity, ω , can be propagated from the base to the tool frame. The resultant velocities can then be rotated back to the base frame using the rotation matrix ${}^0_N R$.

$${}^{i+1}\omega_{i+1} = {}^{i+1}_i R \dot{\omega}_i + \dot{\theta}_{i+1} {}^{i+1}\hat{Z}_{i+1} \quad (5.4)$$

$${}^{i+1}\nu_{i+1} = {}^{i+1}_i R ({}^i\nu_i + {}^i\omega_i \times {}^i P_{i+1}) \quad (5.5)$$

where ${}^{i+1}\hat{Z}_{i+1}$ is the z-axis unit vector in frame $\{i + 1\}$ and ${}^i P_{i+1}$ is the position vector of frame $\{i + 1\}$ in terms of frame $\{i\}$.

The forces and moments exerted on a manipulator can also be propagated from one link to the next. For many serial manipulators, a static analysis considers only a load applied at the free end. However in the case of a finger, loads are distributed between the links depending on the grasp. Assuming knowledge of the forces applied at each link, the necessary joint torques to keep the system in static equilibrium can be solved for. The inward force iteration equations are given in 5.6 and 5.8.

$${}^i f_i = {}_{i+1}^i R {}^{i+1} f_{i+1} + {}^i F_i \quad (5.6)$$

$${}^i n_i = {}_{i+1}^i R {}^{i+1} n_{i+1} + {}^i P_{F_i} \times {}^i F_i + {}^i P_{i+1} \times {}_{i+1}^i R {}^{i+1} f_{i+1} \quad (5.7)$$

where ${}^i F_i$ is the applied force on link i and ${}^i P_{F_i}$ is the position vector describing the

contact point for the applied load on link i . The joint torque needed to maintain static equilibrium is then given by

$$\tau_i = {}^i n_i^T {}^i \hat{Z}_i \quad (5.8)$$

5.1.4 Jacobian Matrix

A Jacobian matrix relates differentials of one coordinate system to another. In robotics, it is desirable to be able to change between tool space and joint space. Thus for serial manipulators, the Jacobian is used to relate joint velocities to Cartesian velocities. In the force domain, the Jacobian transpose is used to map Cartesian fingertip forces to equivalent joint torques. These relationships are described in Equations (5.9) and (5.10).

$$v = {}^i J(q) \dot{q} \quad (5.9)$$

$$\tau = {}^i J^T(q) {}^i F \quad (5.10)$$

where v is the vector of tool velocities, q is the vector of joint velocities, and F is the vector of fingertip forces and torques.

The structure of the Jacobian matrix depends upon the number of DOFs in Cartesian space under consideration and the number of joints in the manipulator. For the finger analysis in three-dimensional space, this leads to a 6 x 4 matrix that can be broken down into two components, rotational and translational. Equation (5.11) defines the rotational Jacobian for a manipulator with all revolute joints.

$${}^i J_{\text{rot}} = \begin{bmatrix} {}^i_1 R \hat{z} & {}^i_2 R \hat{z} & \dots & {}^i_N R \hat{z} \end{bmatrix} \quad (5.11)$$

The most straightforward method to determine the translational Jacobian is by direct differentiation. Taking the partial derivatives of the position vectors gives the matrix shown in Equation (5.12).

$${}^i J_{\text{trans}} = \begin{bmatrix} \frac{\partial^i P_{xN}}{\partial \theta_1} & \frac{\partial^i P_{xN}}{\partial \theta_2} & \cdots & \frac{\partial^i P_{xN}}{\partial \theta_N} \\ \frac{\partial^i P_{yN}}{\partial \theta_1} & \frac{\partial^i P_{yN}}{\partial \theta_2} & \cdots & \frac{\partial^i P_{yN}}{\partial \theta_N} \\ \frac{\partial^i P_{zN}}{\partial \theta_1} & \frac{\partial^i P_{zN}}{\partial \theta_2} & \cdots & \frac{\partial^i P_{zN}}{\partial \theta_N} \end{bmatrix} \quad (5.12)$$

Combining the two components, the full Jacobian relating joint velocities to tip velocities is

$$J = \begin{bmatrix} J_{\text{trans}} \\ J_{\text{rot}} \end{bmatrix} \quad (5.13)$$

Reversing the Jacobian relationship to get joint velocities from Cartesian velocities raises singularity concerns. A singular configuration of a manipulator is a configuration at which the Jacobian becomes rank deficient. For a manipulator with fewer than six DOFs, this corresponds to fewer DOFs of the end-effector. Near these configurations, joint velocities required to maintain certain desired end-effector velocities can become extremely large. Likewise, small joint torques can produce large end-effector forces.

For a square Jacobian, the inverse Jacobian can be used to determine the reverse relationship between joint and Cartesian velocities. At singular configurations, the inverse is not defined. These conditions can be found by solving for configurations where the determinant of the Jacobian equals zero.

For a non-square Jacobian, as in the case of the finger manipulator, the inverse of the Jacobian cannot be used. Instead, the Moore-Penrose pseudoinverse Jacobian

is defined to determine joint velocities from end-effector velocities (5.14, 5.15). This pseudoinverse is not defined at the singular configurations where the rank of the Jacobian drops[37, 38].

$$J^\dagger = J^T(JJ^T)^{-1} \quad (5.14)$$

$$\dot{q} = J^\dagger v \quad (5.15)$$

Singular value decomposition (SVD) provides a tool for analyzing singularities in all possible kinematic structures. Every matrix $A_{m \times n}$ with arbitrary dimensions $m \times n$ has an SVD that expresses A in the form

$$A = U\Sigma V^T \quad (5.16)$$

such that U and V are orthogonal matrices and Σ is an $m \times n$ diagonal matrix with elements $\sigma_1 \geq \sigma_2 \geq \dots \geq \sigma_m \geq 0$. Matrix A has full rank when $\sigma_m \neq 0$ and loses rank when $\sigma_m = 0$ [39]. Applying SVD to the Jacobian matrix, proximity to singular configurations can be checked by monitoring the value of σ_m .

5.2 Multifingered Hand Kinematics

5.2.1 Hand Kinematics

Considering the hand as a whole and the total grasp forces on an object, it is necessary to determine the transformation to represent the finger forces in a common frame. To simplify the calculation, the new base frame is located at the wrist and aligned with frame $\{0\}$ of fingers II-V. With the exception of the thumb, the transformations then involve only translation. The rotation of the thumb frame

is defined relative to the base frame by a -90° rotation about the wrist x-axis and a -45° rotation about the wrist z-axis. Calculating the rotation matrix for the thumb and the overall hand geometry, a transformation, W_0T_i , is defined for each finger, i . Equation (5.17) is then used to determine the forward kinematics from the common wrist frame, $\{W\}$, to the tool frame, $\{N\}$.

$${}^W_NT_i = {}^W_0T_i {}^0_NT \quad (5.17)$$

With a common base frame to work from, a hand Jacobian can be formed to determine joint torques for each from given tip forces. The hand Jacobian is based on the standard Jacobian and is brought together in the form

$$\begin{bmatrix} \tau_1 \\ \tau_2 \\ \vdots \\ \tau_m \end{bmatrix} = \begin{bmatrix} J_1^T & 0 & \cdots & 0 \\ 0 & J_2^T & \cdots & 0 \\ \vdots & \vdots & \ddots & \vdots \\ 0 & \cdots & 0 & J_m^T \end{bmatrix} \begin{bmatrix} f_{\text{tip}_1} \\ f_{\text{tip}_2} \\ \vdots \\ f_{\text{tip}_m} \end{bmatrix} \quad (5.18)$$

5.2.2 Grasp Quality Considerations

Further analysis of a multifingered hand focuses on grasp stability. A grasp is composed of a set of contacts that can be represented by screw systems. By this representation, the collective forces and moments on a body can be described as a force along and a moment about a single wrench axis. Likewise, the motion of the body can be represented as a translation along and a rotation about a twist axis. For each contact, the twist and wrench systems can be used to describe the constraints.

Without a physical bonding agent, two bodies in contact can only exert forces in one direction. In addition, for friction contacts to be active, the normal force must be positive. As a result of these unisense force limitations imposed on an arbitrary grasp, only a subset of all possible disturbance forces can be resisted by a grasp. In these cases, if the disturbance forces act to maintain contact between the fingers and the object and thus the grasp can still be maintained, a condition of force closure is met. A grasp that can resist arbitrary disturbance wrenches is said to exhibit form closure. For an object completely restrained by a grasp, there is a set of internal forces that can be applied to the object without disturbing its equilibrium.

For a total of n wrenches acting on an object and assuming p of those wrenches are unisense, the wrench matrix, $W_{6 \times n}$, is built as shown in Equation (5.19). To resist an arbitrarily applied wrench, w , on an object, there must then be a vector, c , of contact wrench intensities that satisfies Equation (5.20).

$$W = \begin{bmatrix} w_1 & w_2 & \dots & w_p & w_{p+1} & \dots & w_n \end{bmatrix} \quad (5.19)$$

$$Wc = w \quad (5.20)$$

If the wrench matrix W has a rank of six and contains the applied wrench w in its column space, a grasp may be able to fully constrain an object. However, as a result of the p unisense wrenches, the first p elements of the c vector must also be positive. If these elements are not, the wrench w can cause broken contacts or slip to occur at unisense contact points. The solution to (5.19) can be broken up into

the two vectors c_p and c_h such that

$$c = c_p + \lambda c_h \tag{5.21}$$

where c_p is the particular solution to (5.19) and c_h is the homogeneous solution. If the first p elements of c_h are positive, then for any value of c_p , there is some large value of λ that will result in the first p elements of c to be positive as well. Thus, c_h corresponds to the internal grasp forces that can be increase by a magnitude of λ to make the contact forces positive[40, 41].

Chapter 6

Testing and Results

The previous chapters described the design of a geometrically anthropometric robotic finger utilizing antagonistic actuator pairs. Studies on human hand motion and grasp force distributions as well as an analysis describing the expected finger behavior were also presented. A kinematic analysis was performed and yields a model relating opposing tendon tensions and applied loads. This chapter presents experimental strength and position tests and compares the results with the predictive model.

Position of the PIP and DIP joints were measured over the full range of flexion and extension. Holding tendon tensions were also measured for varying cylindrical grasp diameters and weights. Finally, an analysis of the benefit of active antagonism was performed by measuring tip force resolution and joint positioning for differing tendon tensions.

6.1 Test Setup

A test stand, shown in Figure 6.1, was developed to actuate a single degree of freedom in opposition. Two motors are mounted to a cylindrical delrin base. As with the hand actuator assembly, these motors connect to leadscrews by oldham couplings with the leadscrew supported by bushings on both ends. Guide rails for

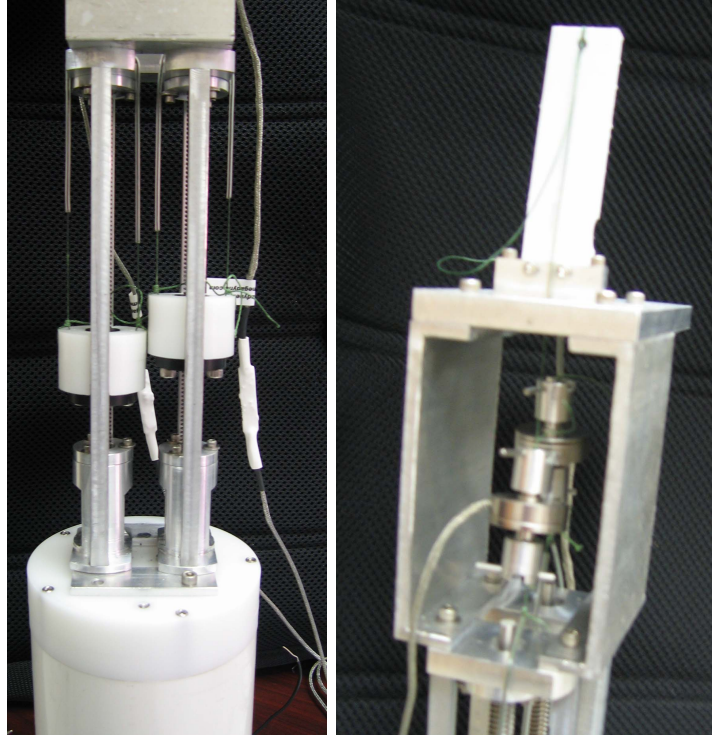


Figure 6.1: Side View & Close-Up of Load Cells/Top Plate

the leadscrew nut are bolted to the delrin base. Spectra cable attaches to two sides of each nut and routes through wire tubing over the edges of the bushing mounts. Beyond the bushing mount, the spectra cables join to a single line and connect to a tension/compression force sensor. The other end of the tendon connects from the sensor up to the actuated joint. Wire tubing and cable restraints were used to guide the tendons along the links and around corners. The finger mechanism itself mounts on an interchangeable plate, as shown in Figure 6.2, that allows for simple changing of test components.

The test setup only allows for actuation of a single degree of freedom at a time. Initially, the compliant skeleton with phalange shell components was intended to be the test element. However, due to fabrication problems with the rapid prototype



Figure 6.2: Close-up of Load Cell Attachment and Top Plate

machine, the shell components were not completed. For the desired testing goals, it was deemed sufficient to use only the compliant mechanism. The compliant piece serves as a skeletal base for the finger and therefore is capable of the necessary grasps for testing. In addition, investigation of joint positions and the effect of active antagonism can be effectively executed with the simplified skeletal setup.

For position testing, a goniometer was used to measure PIP and DIP joint flexion of the 2DOF compliant skeleton. To compare the natural coupling of the compliant skeleton to expected behavior, only the flexion tendon was used and angles taken from fully open to fully closed at $\frac{1}{16}$ -inch intervals of linear screw actuation. In this setup, the flexion tendon was attached at the tip and routed through a restraint at the mid-point of the middle phalange. Changing from fully open to fully closed configurations required a linear actuation distance of one inch. In addition to measuring relative joint angles, flexion tendon tension was also measured using the tension/compression force sensor for comparison to the model.

Tendon forces relative to grasp load were measured using the test setup in an inverted mounting position. A single finger was tested in a cylindrical grasp. The

total load was increased by attaching weights in a bag to the cylinder and the flexion tendon force recorded. No extension tendon was used during this testing.

The final set of tests conducted examined the effect of the antagonistic actuation pair. Joint angle position tests were repeated with the 2DOF compliant skeleton, this time using the extension tendon in varying levels of tension. Because the tendon tensions change relative to each other when one side is actuated, these tests were done by adjusting linear positions. The leadscrew position of the extension tendon was kept constant while the flexion tendon was actuated from fully open to fully closed in increments of $\frac{1}{16}$ -inch. Joint angles and tendon tensions were recorded at each position.

Tip forces were also studied in the antagonistic case. A single DOF joint was mounted on the test stand and an Omega LC302 button cell compression force sensor placed such that when fully actuated, the tip touches the center of the sensor. Tip forces were then measured while varying the relative antagonistic tendon tensions.

6.2 Data/Results

6.2.1 Coupled Joint Angles

Joint coupling behavior is shown in Figure 6.3. The experimental data is fit to a 2^{nd} order polynomial with an R^2 value of 0.92. As seen in the graph, the experimental behavior is similar to that of the predictive model. The main difference, seen at the beginning of the flexion motion, is likely due to the fact that the compliant joint does not return completely to its original unbent position. After

the joint is initially bent, it tends to have a preferred base position of approximately 10 degrees. While this behavior is consistently repeated, it is not factored into the model.

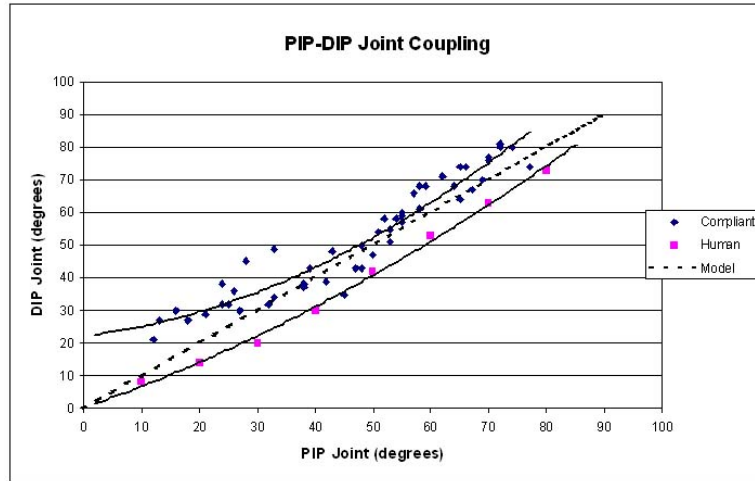


Figure 6.3: PIP-DIP Joint Coupling

The coupled joint motion observed also matches well with human finger motion. The human PIP-DIP coupling is shown as described by Lee and Rim[2]. The upward shift of the experimental trend line relative to the human line is again likely due to the initial bend of the DIP joint.

6.2.2 Tendon Forces in a Cylindrical Grasp

Analysis of grip strength was analyzed for a cylindrical grasp. Using a single finger wrapped around a 1.25" diameter aluminum cylinder, tendon tensions were measured for loads up to 10 lbs. Although the largest EVA tool diameter for testing is 2.00" in diameter, the mounting point of the finger in the test stand creates in a shortened proximal phalange, thus resulting in a maximum grasp geometry of 1.25". However, by testing beyond the required 20 lb grasp distributed over four fingers,

the single finger test can still demonstrate sufficient strength capability.

Lead weights were added to a cordura bag attached by spectra cable to the grasping cylinder in approximately one-pound increments. The applied weight at each increment was measured and recorded. The finger was then actuated in flexion until the cylinder was held securely. Holding tension of the flexion tendon was then measured. Figure 6.4 shows the flexion tendon forces relative to the total load on the finger. The calculated tendon tensions, derived from the kinematic model and based on the geometry of the hand in a 1.25" cylindrical grasp, are also displayed on the graph.

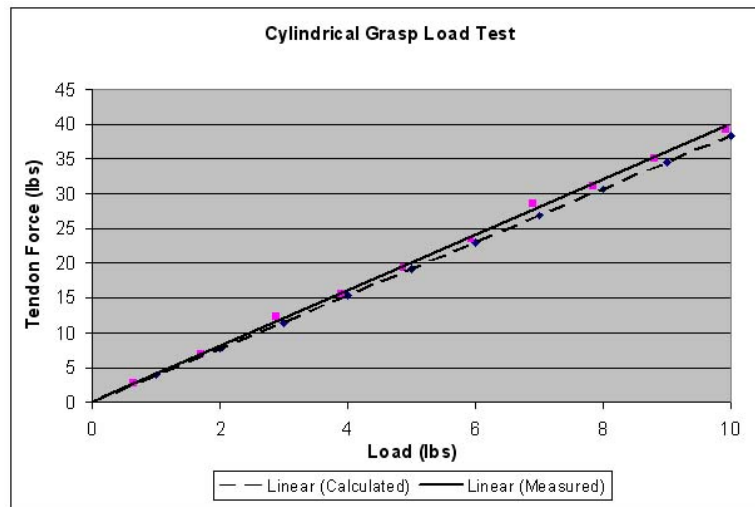


Figure 6.4: Tendon Tensions for Applied Loads on a 1.25" Diameter Cylindrical Grasp

As depicted in Figure 6.4, the measured tendon tensions increase linearly with applied load and appear to correspond with the expected forces. The experimental values seem to increase at a steeper slope than the calculated, though this can be attributed to friction in the system. In addition, previous calculations show that for a distributed cylindrical grasp, a 20 lb total grip force requires a maximum load

of 6.50 lbs on a single finger. Testing has proven an individual finger capable of holding up to a 10 lb load, 50% greater than the required load.

6.2.3 Active Antagonism

The use of opposing actuators affects both joint control and tip forces. Due to the compliant nature of the skeleton, changing the relative tensions of the flexion and extension cables creates a level of decoupling between the DIP and PIP joint DOFs. Figures 6.5 shows DIP joint angles relative to the measured flexion tendon tensions. Each line represents a constant extension tendon position with varying tension. Testing shows that for an unloaded finger, the relative flexion and extension forces remain consistent despite linear position. Thus, the predictive model determines the DIP joint angle based on the experimentally derived relationship between flexion force and extension force during actuation. The slopes of the experimental trend lines verify the model. An upward shift in the data is again seen and can once more be attributed to the initial bend in the DIP joint.

There is significantly less variation in the PIP joint angle. For a given extension tendon position, experimental data shows that the PIP joint angle generally remains constant from open to close (Figure 6.6). When both the extension and flexion tendon positions are more fully actuated, corresponding to significantly greater forces on both sides, the joint angle begins to vary during actuation. Based on joint angle calculations done for the DIP joint, this result corresponds to the expected trend. The location of the attachment point also makes it such that the affect of

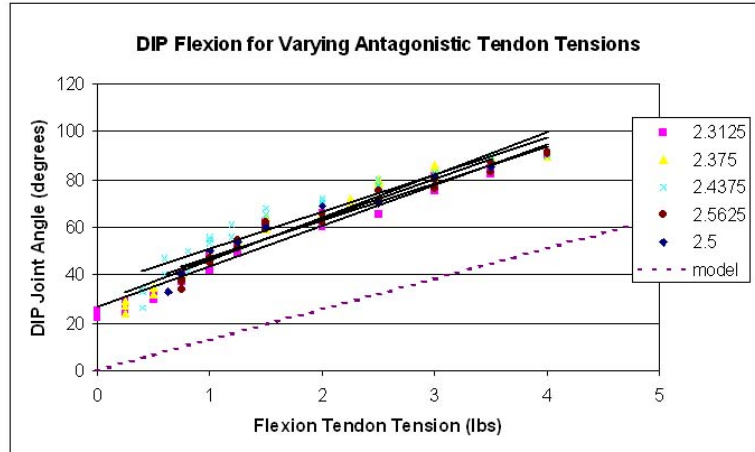


Figure 6.5: DIP Flexion for Varying Antagonistic Tendon Tensions

The legend indicates the linear position of the extension tendon in inches from the top of the test setup.

the extension tendon is greater at the distal versus proximal joint. As a result, it is possible to gain some level of control over the two coupled joints using an antagonistic setup. This is particularly useful for grasps that conform to the shape of the object, rather than a fixed curve.

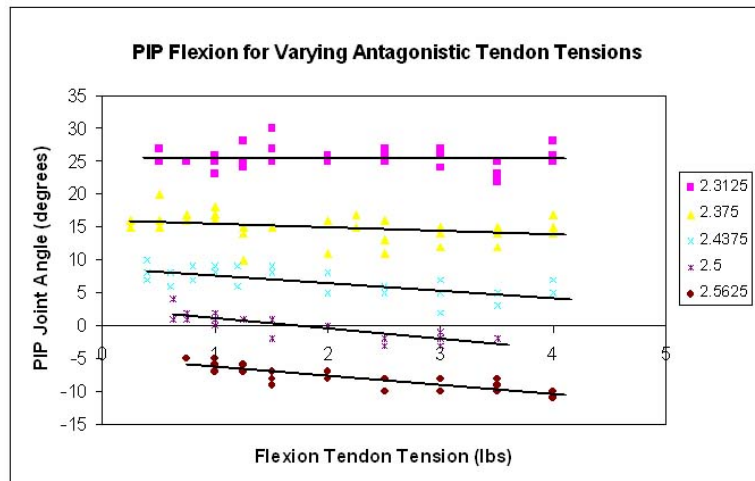


Figure 6.6: PIP Flexion for Varying Antagonistic Tendon Tensions

The legend indicates the linear position of the extension tendon in inches from the top of the test setup.

Testing on tip forces further demonstrates the benefit of an antagonistic tendon

setup. Switching to a single DOF compliant hinge, the test component was fully flexed to touch a button cell. With the flexion tendon pulled in such that it was fully actuated, the force on the extension tendon was then increased with the joint fully flexed. Both tendon tensions as well as subsequent tip force were recorded.

Initially, data was recorded continually while the extension tendon was actuated. However, running the motors resulted in increased noise. The range of forces measured at the tip was small enough that in combination with the added noise, the resultant data was inconclusive. Instead, data was recorded in 0.1-pound increments on the extension tendon. The averaged results are detailed in Figure 6.7.

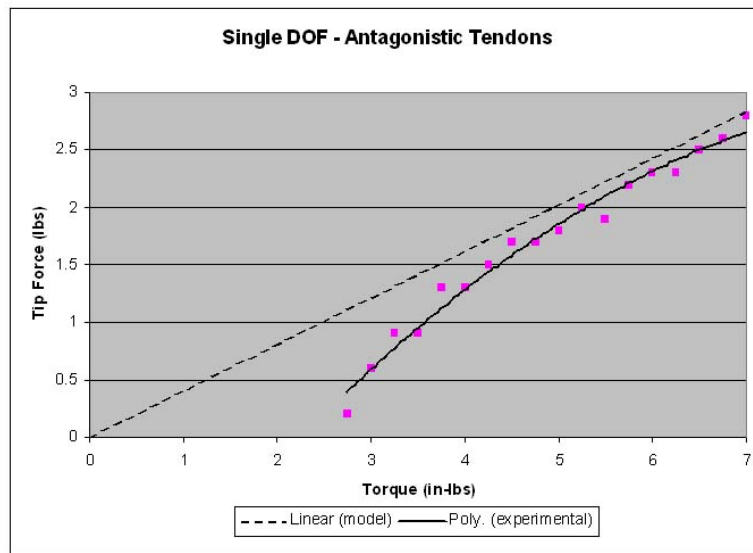


Figure 6.7: Tip Force vs Joint Torque

Torque was calculated based on the measured opposing tendon tensions. Based on the kinematic analysis detailed in Chapter 5, the comparative model determined joint torque over the range of measured tip forces. The tip force was assumed to act only in the y-axis of the tip with the joint angle fixed at 90° . The overall results show slightly smaller than expected forces with greater correlation to the model at higher

tip forces. This is largely due to the quality of contact at the load cell. At higher joint torques and subsequent greater tip forces, there is a more solid contact and the results closely match the expected values and trend. However, at lower forces where the contact could be considered more of a "touch" as opposed to "pressing" down on the button cell, the measured tip forces drop off dramatically. At approximately 2.5 in-lbs of torque, the test component lost contact with the force sensor and tip forces drop to zero.

Chapter 3 previously derived a required pinch grasp force of 5 lbs. Assuming a two-finger pinch and taking the grasp force as the total force applied to the object by the tips of both fingers, the maximum measured tip force for the fully actuated flexion shows the design is capable of satisfying the pinch requirement.

The experimental results further demonstrate the adaptability of the spring constant in the system. The torsional spring constant is taken from the relationship in Equation (6.1).

$$T = k\theta \tag{6.1}$$

The angle, θ , is assumed constant throughout as the test component is kept fully flexed. Therefore, as the joint torque varies for a constant θ , so does the spring constant of the system. The compliant hinge was designed with a spring constant of 4.5 in-lbs/rad. Experimental results with measured contact force provide a range of spring constants from 1.75-4.45 in-lbs/rad.

Chapter 7

Conclusions & Future Work

7.1 Summary

This thesis documents the development of a robotic finger for an anthropomorphic hand and details preliminary performance results. The benefits and drawbacks of different aspects of hand design are examined and insight into effective configurations provided. The research focuses on the detailed design of an actuated finger with particular interest in studying the use of opposing actuator pairs. A kinematic model is derived that presents a working analysis of the finger. Preliminary testing of tendon and tip forces verifies this model. Analysis of joint motion is also compared to human motion and found to correspond with the desired anthropomorphic behavior.

The work presented is the starting to point to a fully developed and highly dexterous robotic hand. Design choices consider future sensor integration and basic palm configuration solutions are proposed. The goal to design a hand component capable of EVA tool grasps and force requirements has been satisfied.

7.2 Future Work

Several avenues of research must be pursued to reach the ultimate goal of a fully operational hand for EVA tasks. Further development should continue with the single finger, followed by an intermediary 3-finger grasping manipulator, and finally a 5-fingered hand. The subsequent sections detail a plan for future work.

7.2.1 Single Finger Development

The first step towards the end goal is a second iteration of the single finger design. Both tendon attachment and compliant mechanism design should be revisited. One of the primary weaknesses in the current version is the tendon attachment procedure. From an assembly point of view, cable termination was by far the most time consuming step. In addition, the knots used were difficult to tie off at the exact point desired along the tendon line and prone to initial slipping. Methods of pre-tensioning that do not rely on increasing the linear actuation distance should also be investigated to ease the packaging constraints of the lead screw assemblies.

In addition to developing the tendon system, a re-design of the compliant mechanism may greatly improve performance. The current design tends to favor actuation of the DIP joint over the PIP joint. One branch of further study should aim to optimize the relative attachment points of the flexion and extension tendons as well as examine how an asymmetric hinge geometry would affect the compliant skeleton behavior. Another path of interest is to better characterize the ability of the compliant mechanism to both conform to grasp shapes and be forced into

desired shapes during actuation. Analysis of the compliant behavior is necessary to demonstrate the benefit of this approach over the typically rigid 4-bar linkage.

With the initial design revisions, a second prototype finger should be manufactured, including the phalange shell components and a basic palm attachment structure. Ideally, a new version of the MP hub should be manufactured with an integrated abduction/adduction shaft. Rapid prototyping is still desired for the phalange shell components to enable more complex internal geometries for wire routing and joint range of motion limitation. The second prototype will also require a new test stand design that can actuate three DOFs. The new test stand should use the more compact version of the actuator assemblies and look into packaging within the forearm design.

The second prototype should also work on incorporating Hall effect sensors for joint angle measurement and a rudimentary tactile sensing system. This next step in sensor development focuses on packaging within the finger structure and preliminary signal processing. At this point, work on a controls system for the three DOF manipulator can begin, particularly improving the model of the compliant mechanism and antagonistic tendon behavior.

7.2.2 Three-Finger Grasper

The second proposed phase of hand development yields a three-finger grasper. For Finger V (the thumb), minor modifications will need to be made to increase link length and width. In addition, a more complex palm design is necessary that

fits Finger III, Finger IV, and properly mounts Finger V in opposition. Mechanically, this version can use the existing finger design as a basis and focus on the palm structure and forearm packaging. Improvement of the sensor system and data processing can continue on a parallel track.

A three-finger grasper provides an intermediary step to demonstrate grasp capability and investigate multi-finger interaction on a smaller scale. As shown by previous studies on grasp classification and EVA tools, three fingers are sufficient for a stable grasp of all CATs. Research into grasp quality and dexterous manipulation is thus possible with this grasper. Having an end effector with multiple fingers also allows for a more complex analysis of active antagonism, in particular which joints benefit the most during dexterous manipulation. The controls system also becomes increasingly complex and can now research cooperative motion and optimizing grasps.

7.2.3 Five-Finger Hand

The final step is to build a hand with five fingers and wrist. To achieve this goal, mechanical design work will focus on completing the palm structure with a two DOF wrist. The major design consideration is how to best implement the final two grasping fingers. Trade-offs between making full three DOF fingers versus single or two DOF "graspers" should be analyzed. In addition, the necessity of a palm joint to aid in motions of opposition should be studied.

The production of a full five-fingered hand brings the resesarch to the point

of testing the operational use of the end effector. Desired tasks included the ability to pick up and hand off objects of arbitrary shapes and the use of tools to perform complex tasks. Continuing development on controlling five cooperative fingers and determining grasp quality and contact will also be necessary. Beyond the basic functionality and control of the full hand in a lab setting, it is hoped that the research can eventually focus on its use in space. The development of a multi-function end-effector is the first step towards increasing the capability of robots in space. Future research will look beyond the execution of EVA tasks to human-robot interaction and planetary exploration.

Appendix A

Design Measurements and Calculations

A.1 Hand Measurements

The following table details anthropometric data taken from an existing study of American military males[18].

| DIMENSION | MEAN (in) | 95 th percentile (in) |
|------------------------------------|-----------|----------------------------------|
| hand breadth | 3.48 | 3.78 |
| hand breadth across thumb | 4.05 | 4.38 |
| hand circumference | 8.46 | 9.14 |
| hand circumference including thumb | 10.05 | 10.85 |
| hand length | 7.57 | 8.15 |
| hand thickness | 1.14 | 1.28 |
| palm length | 4.30 | 4.70 |
| thumb-crotch length | 1.96 | 2.30 |
| finger diameter | 0.84 | 0.90 |
| finger II-crotch length | 4.97 | 5.50 |
| first phalanx length digit III | 2.67 | 2.9 |
| fist circumference | 11.43 | 12.40 |
| grip diameter, inside | 1.87 | 2.1 |
| grip diameter, outside | 4.08 | 4.40 |
| elbow-grip length | 13.86 | 14.94 |
| elbow-wrist length | 11.61 | 12.57 |
| forearm circumference, flexed | 11.44 | 12.63 |
| forearm circumference, relaxed | 10.91 | 11.96 |

Table A.1: Human Forearm and Hand Measurements

The following table details the results of hand measurements based on the BioConcepts chart. Ten male and ten female subjects were measured using a tailoring tape measure. Average values for males and females are listed for the left and right hand separately.

| DIMENSION | MALE | | FEMALE | |
|-----------|-----------|------------|-----------|------------|
| | LEFT (in) | RIGHT (in) | LEFT (in) | RIGHT (in) |
| A | 6.965 | 7.013 | 6.188 | 6.275 |
| A1 | 6.988 | 7.075 | 6.275 | 6.288 |
| B | 8.363 | 8.363 | 7.375 | 7.488 |
| C | 1.938 | 1.963 | 1.738 | 1.763 |
| D | 2.200 | 2.200 | 1.938 | 2.013 |
| E | 2.063 | 2.113 | 1.850 | 1.888 |
| F | 2.488 | 2.525 | 2.213 | 2.100 |
| G | 2.175 | 2.263 | 1.950 | 1.975 |
| H | 2.613 | 2.688 | 2.313 | 2.425 |
| I | 2.238 | 2.238 | 1.938 | 1.975 |
| J | 2.613 | 2.625 | 2.338 | 2.388 |
| K | 2.700 | 2.788 | 2.388 | 2.450 |
| a | 3.675 | 3.688 | 3.500 | 3.488 |
| b | 4.213 | 4.163 | 3.888 | 3.888 |
| c | 4.250 | 4.300 | 3.925 | 3.875 |
| d | 2.500 | 2.650 | 2.388 | 2.413 |
| e | 2.375 | 2.425 | 2.300 | 2.250 |
| f | 2.850 | 2.850 | 2.850 | 2.838 |
| g | 2.938 | 3.138 | 3.075 | 3.075 |
| h | 2.825 | 2.863 | 2.763 | 2.850 |
| i | 2.525 | 2.388 | 2.338 | 2.525 |
| j | 1.063 | 1.025 | 1.025 | 1.038 |
| k | 0.975 | 0.975 | 0.963 | 0.988 |
| l | 0.950 | 0.950 | 1.013 | 1.025 |
| m | 1.200 | 1.225 | 1.200 | 1.188 |
| n | 1.038 | 1.038 | 1.075 | 1.163 |
| length | 7.463 | 7.425 | 7.113 | 7.175 |
| breadth | 3.475 | 3.488 | 3.100 | 3.113 |

Table A.2: Hand Measurements

A.2 Matlab Code

A.2.1 Leadscrew Selection Calculations

```
clear all;
close all;

% Kerk Motion 1/4" 4000 Series, Lead-Load Torque Comparison
% define lead screw leads and efficiencies
kerk_lead_array = [0.025 0.0357 0.039 0.039 0.050 0.059 0.0625 0.079
                  0.100 0.118 0.200 0.250 0.333 0.394 0.400 0.500
                  0.750 1.000];
kerk_eff_array = [0.30 0.35 0.40 0.33 0.46 0.52 0.52 0.59 .62 0.68
                 0.65 0.79 0.82 0.78 0.84 0.85 0.86 0.84];

% define maximum and nominal tendon loads
load_max_lb = 41.5;
load_max = load_max_lb*16;
load_nom_lb = 10;
load_nom = load_nom_lb*16;

% calculate torque to move max load
kerk_torque_max = load_max.*kerk_lead_array./(2*pi.*kerk_eff_array);

% calculate torque to move nominal load
kerk_torque_nom = load_nom.*kerk_lead_array./(2*pi.*kerk_eff_array);

% define desired linear speed (in/s)
linspd = 4;

% define rpm for nominal tendon loads
rpm = linspd./kerk_lead_array*60

% calculate motor power for nominal loads
p_nom = kerk_torque_nom.*rpm.*0.00074;

% plot torque vs lead
figure;
plot(kerk_lead_array,kerk_torque_max,'k. ');
xlabel('Lead (in)');
ylabel('Torque to Move Load (oz-in)');
title('Lead vs. Load Torque');
hold on;
plot(kerk_lead_array,kerk_torque_nom,'bx');
```

```

legend('Max','Nominal');
hold off;

% plot power vs lead
figure;
plot(kerk_lead_array,p_nom,'b.');
```

xlabel('Lead (in)');
ylabel('Motor Power to Move Nominal Load (W)');
title('Lead vs. Motor Power');

A.2.2 Motor/Gearbox Calculations

```

clear all;
close all;

% Define BF4000 values
bf4000_lead = 0.118;
bf4000_eff = 0.68;

% Define load requirements
load_max = 40*16;

% Calculate torque to move load [oz-in]
bf4000_torque = load_max*bf4000_lead/(2*pi*bf4000_eff)

% Calculate desired rpm and desired output speed under load
rpm = 4/bf4000_lead*60
nL = rpm/2

% Estimate required power
P = bf4000_torque*0.0071*pi/30*nL

%%%%% Calculate theoretical reduction ratio
n_gearpermiss = 8000;
itheor = n_gearpermiss/nL

%%%%% Calculate motor speed
i = 5.4; % nearest lower available reduction ratio
n_motor = i*nL

%%%%% Define gearhead efficiency
eta_gear = 0.84;
```

```

% Calculate necessary motor torque
motor_torque = bf4000_torque*0.0071*1000/(i*eta_gear) % [mNm]

% Winding Selection
%%%%%%%% Calculate no load speed
stgrad = [202 202 202 202]; % from motor selection specs (line 5)
ni = n_motor+(stgrad.*motor_torque);
%%%%%%%% Calculate theoretical speed constant
U = [24 24 24 24]; % from motor selection specs
kni = ni./U

%%%%%%%% Power check
Pmotor = [20];
deltap = Pmotor-P

%%%%%%%% No-load speed check
no = [9500 16500 9500 16500];
deltan = no-ni

%%%%%%%% Actual speed constant and difference
kn = [406 704 406 704];
deltak = abs(kni-kn)

%%%%%%%% Stall torque safety factor
Mh = [48 83 48 83];
sf = Mh./motor_torque

```

A.2.3 Finger Force-Moment Analysis

```

clear;

% Define Indices
p = 1; % proximal
m = 2; % middle
d = 3; % distal

% Define Link Lengths
l_prox = 1.1;
l_mid = 1.1;
l_dist = 1.1;

% Define Finger Geometry for 2.00'' Diameter Grip
angles(2,:) = [60 55 37.5];

```

```

angles(3,:) = [57.5 55 40];
angles(4,:) = [55 52.5 40];
angles(5,:) = [37.5 47.5 37.5];

% Define Force Center Locations (Long Axis)
centers(2,:) = [0.51 0.74 0.47];
centers(3,:) = [0.59 0.65 0.44];
centers(4,:) = [0.64 0.62 0.48];
centers(5,:) = [0.63 0.40 0.63];

% Define Distributed Phalange Forces
forces(2,:) = [2.08 1.17 3.25];
forces(3,:) = [1.89 1.06 2.94];
forces(4,:) = [1.45 0.814 2.26];
forces(5,:) = [0.986 0.554 1.54];

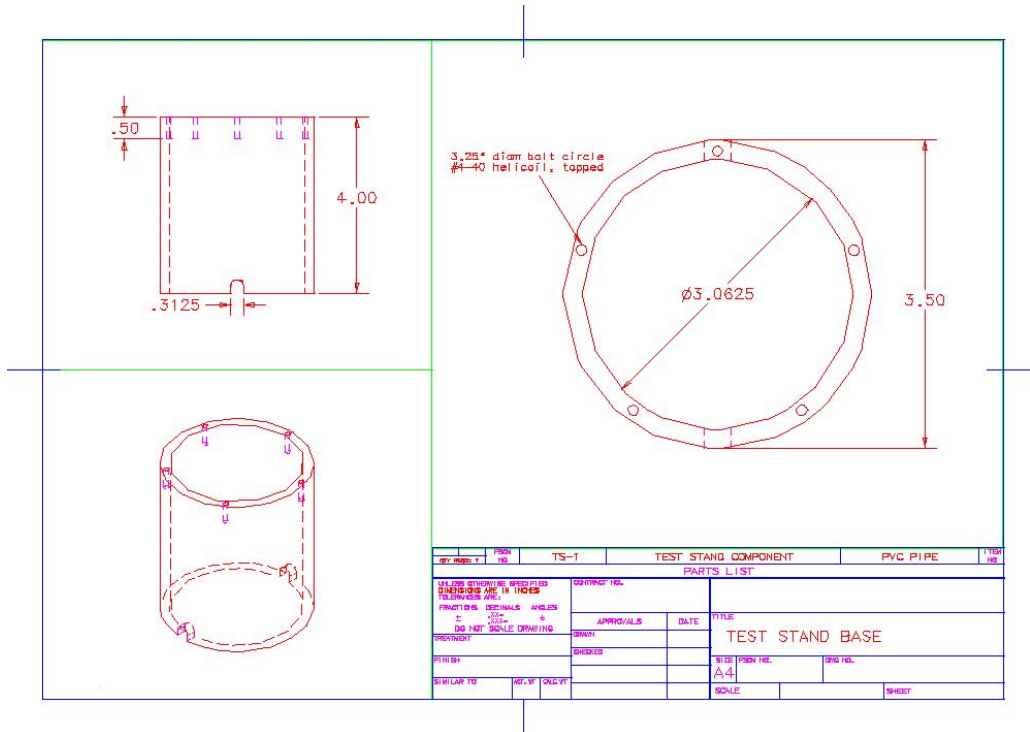
% Calculate Moments
for i=2:5
    l_13 = sqrt(l_prox^2+l_mid^2-2*l_prox*l_mid*...
        cosd(180-angles(i,m)));
    theta_inner = acosd((l_mid^2-l_prox^2-l_13^2)/(-2*l_prox*l_13));
    M_mp(i) = forces(i,p)*centers(i,p)+forces(i,m)*(centers(i,m)
        +l_prox*cosd(angles(i,m)))
        +forces(i,d)*(centers(i,d)+l_13*cosd(theta_inner));
    M_pip(i) = -forces(i,p)*(l_prox-centers(i,p))
        +forces(i,m)*centers(i,m)
        +forces(i,d)*(centers(i,d)+l_mid*cosd(angles(i,d)));
    M_dip(i) = forces(i,d)*centers(i,d)
        -forces(i,m)*(l_mid-centers(i,m))
        -forces(i,p)*((l_prox-centers(i,p))+l_mid*...
            cosd(angles(i,m)));
end

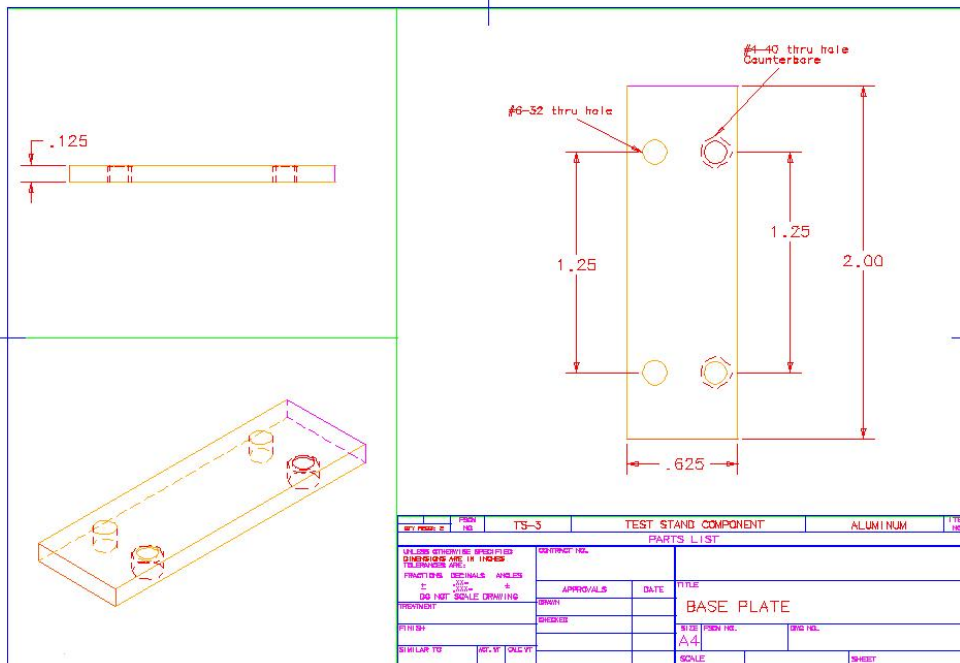
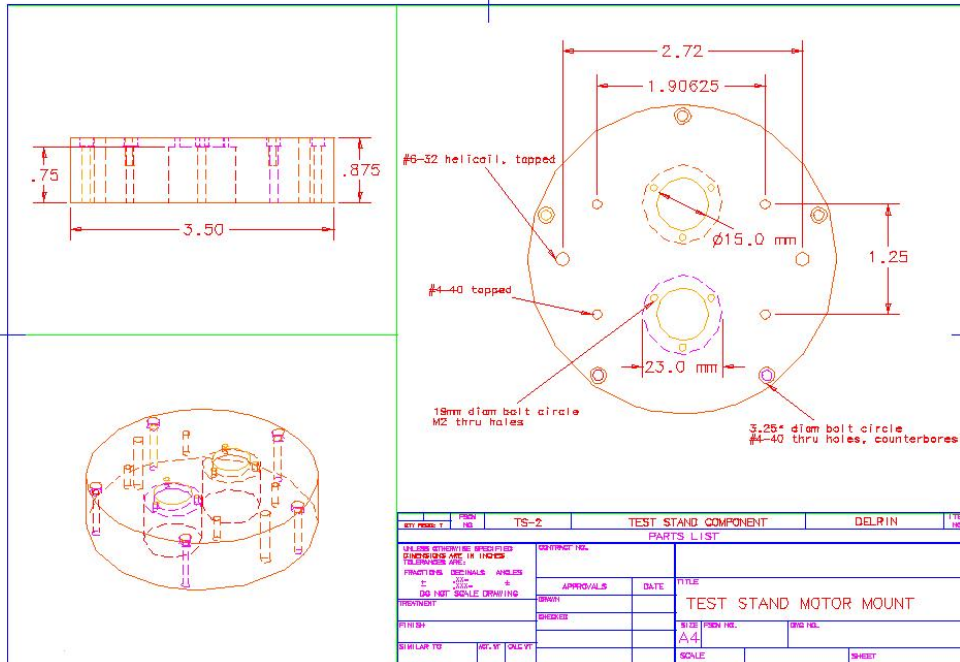
M_mp
M_pip
M_dip

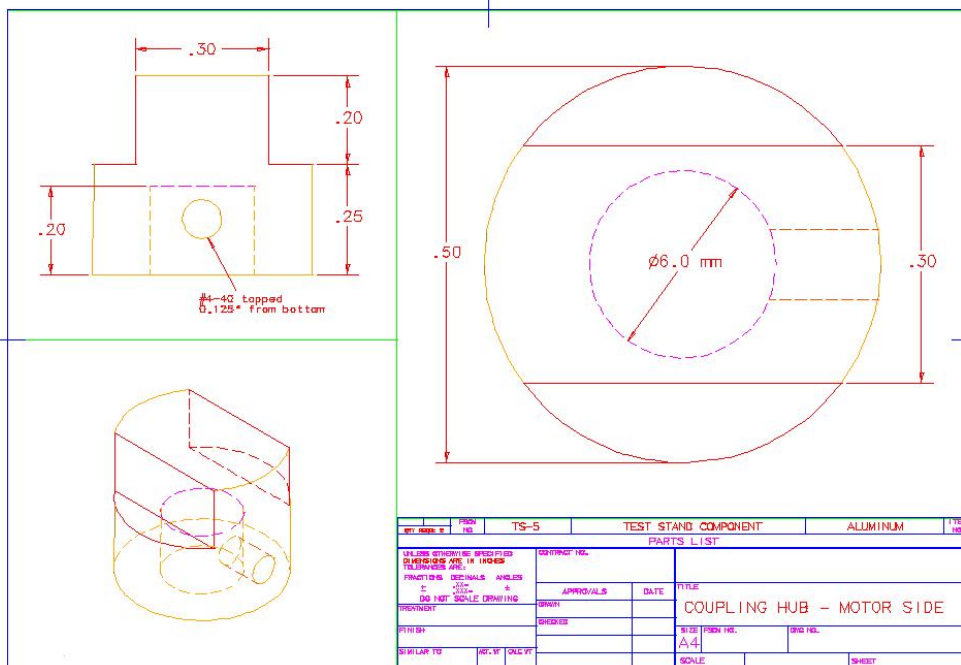
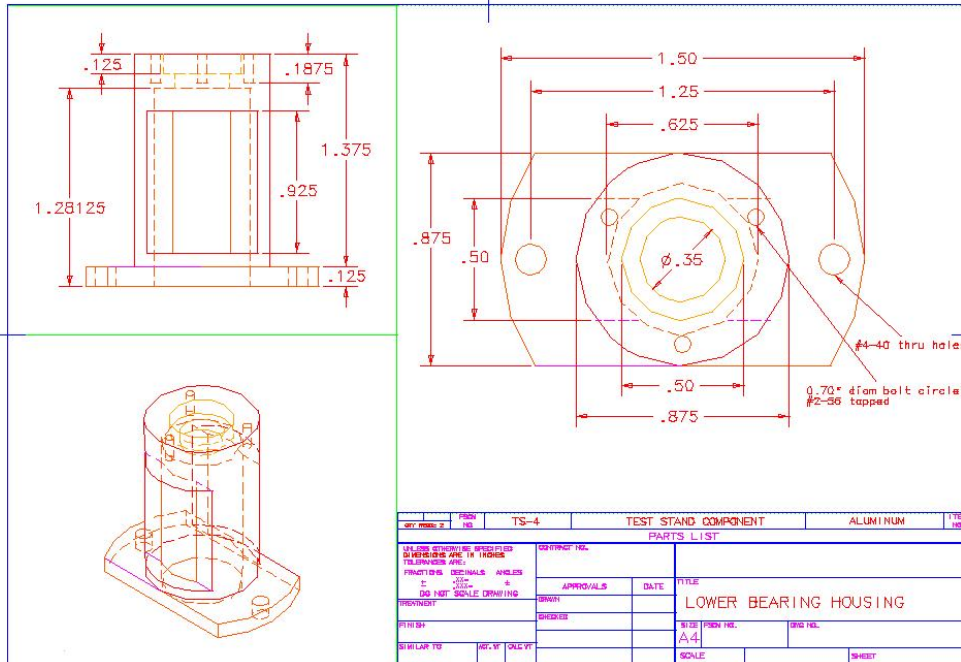
```

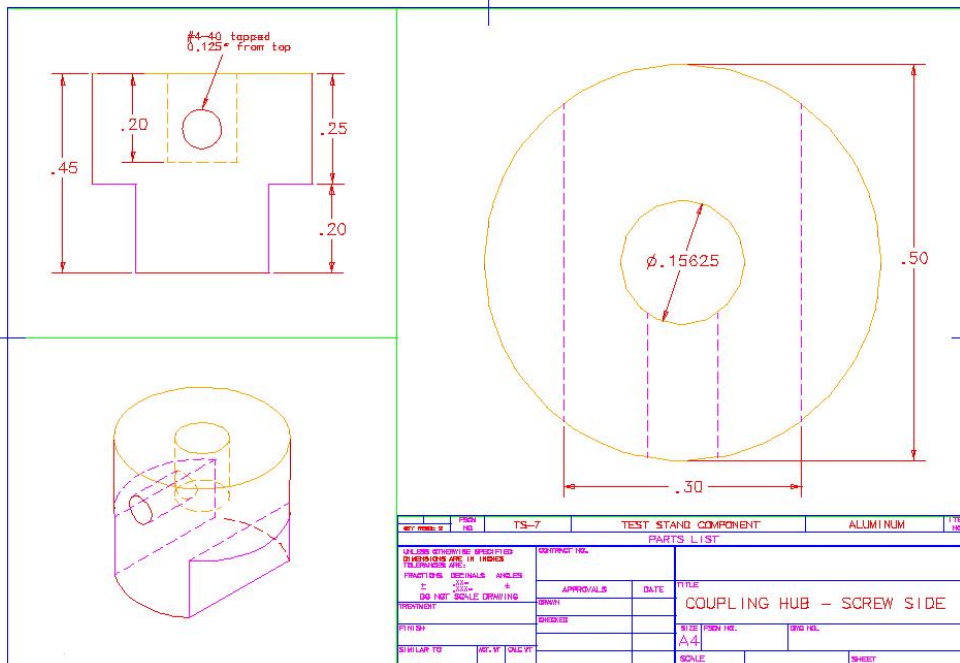
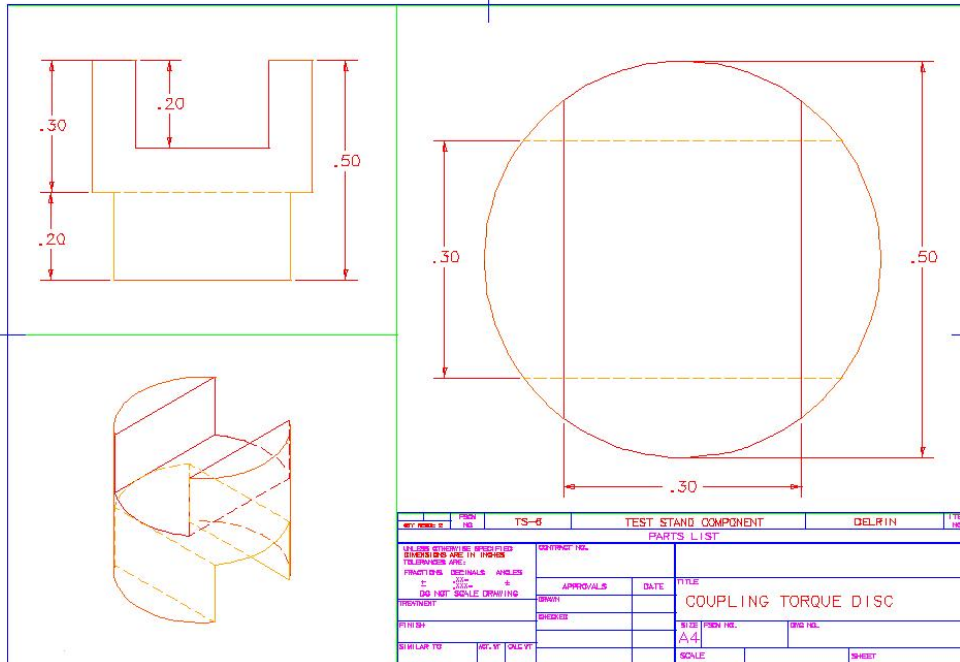
Appendix B

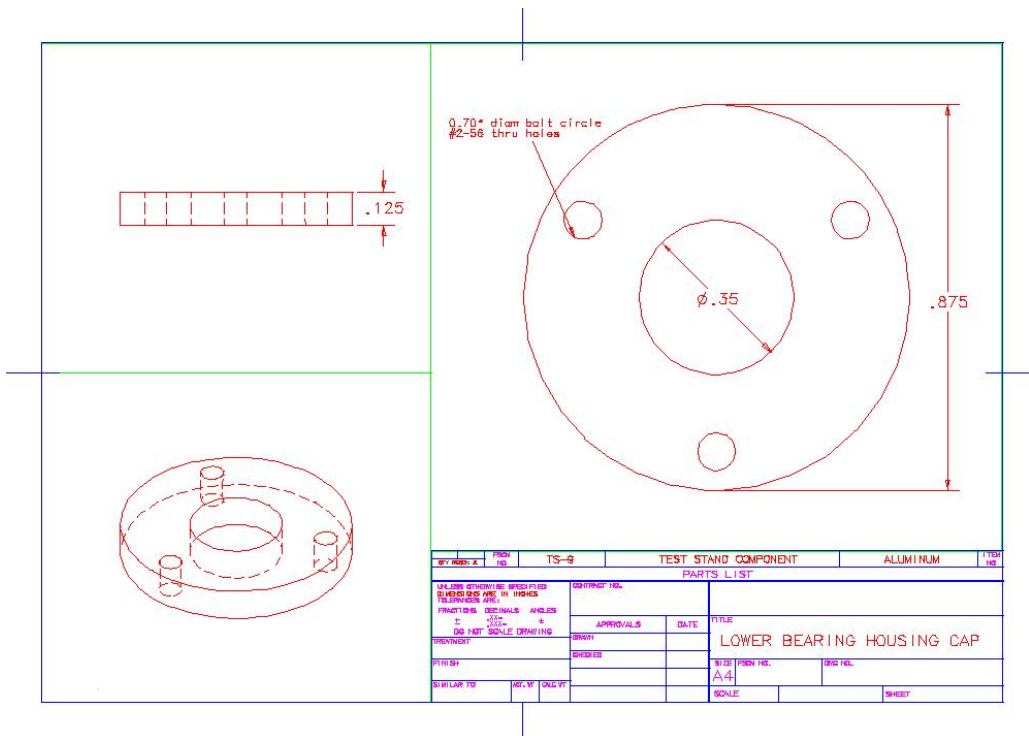
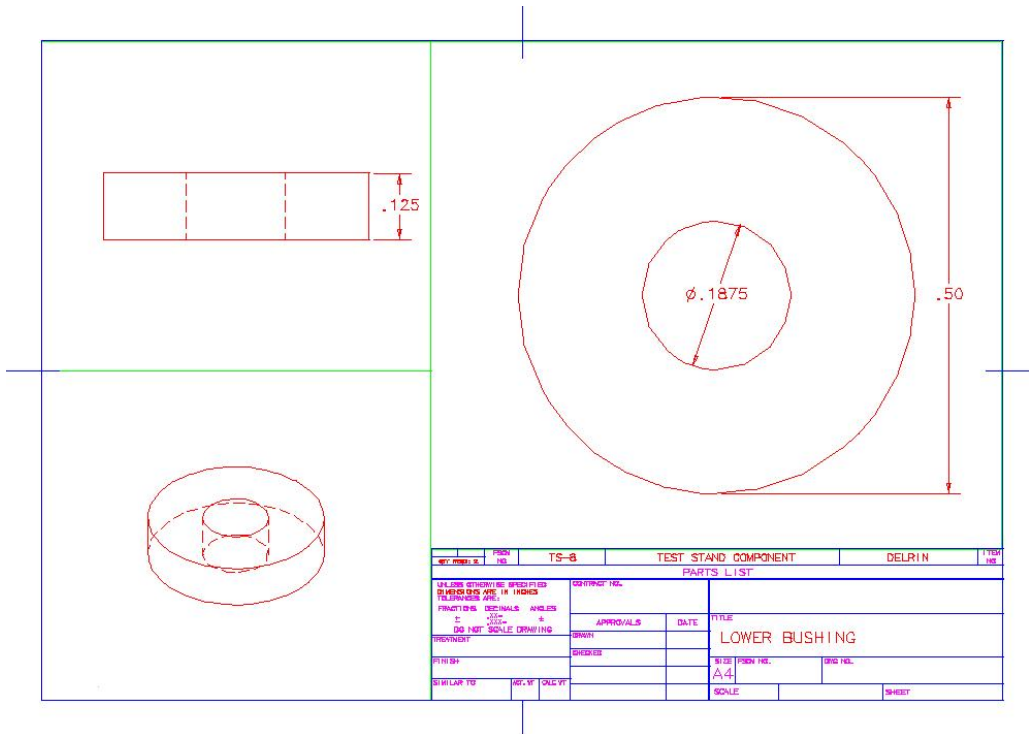
Component Drawings

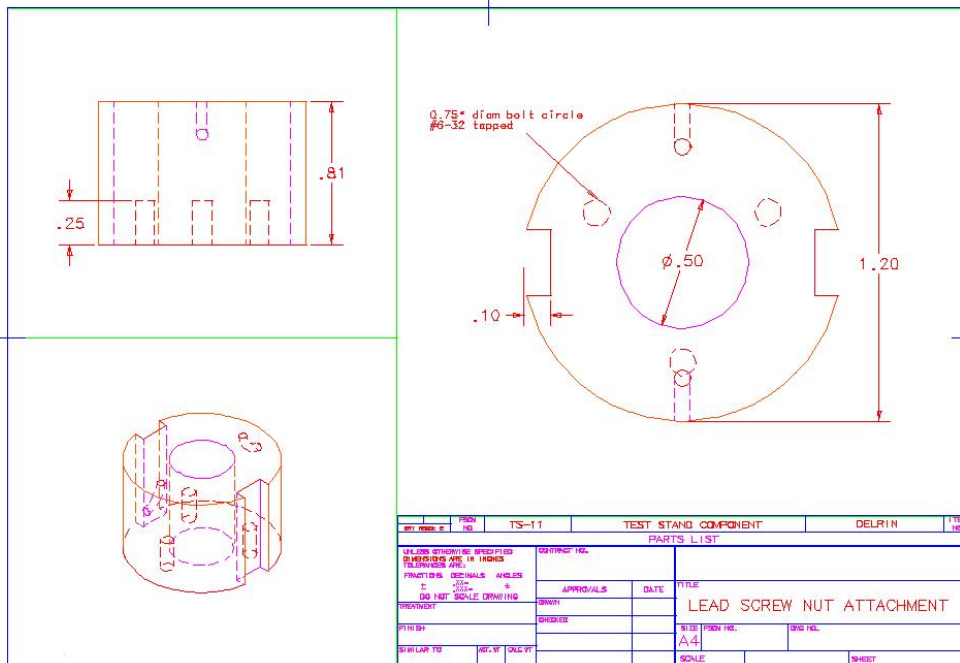
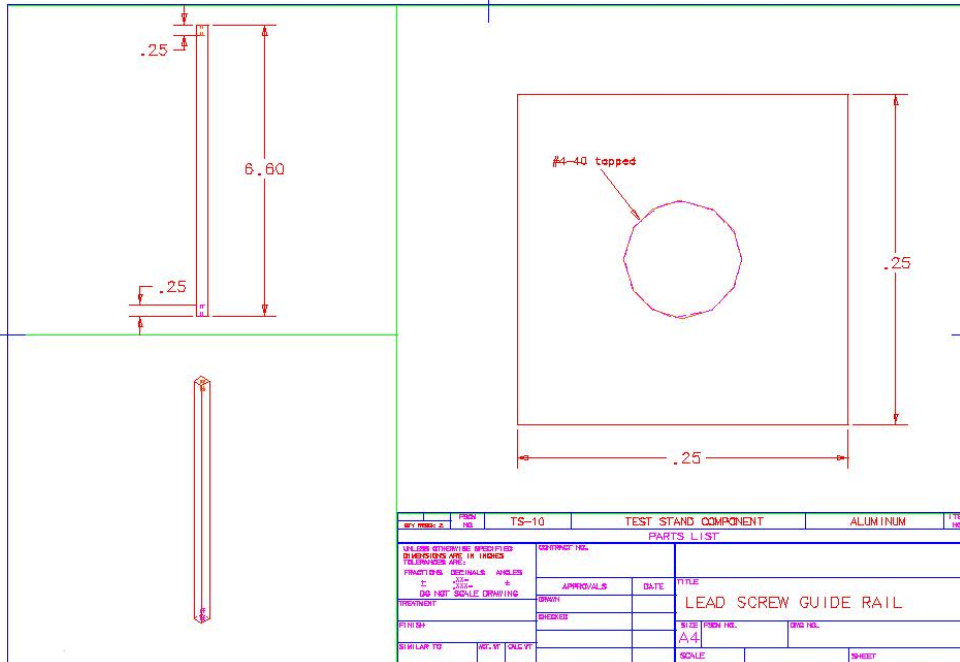


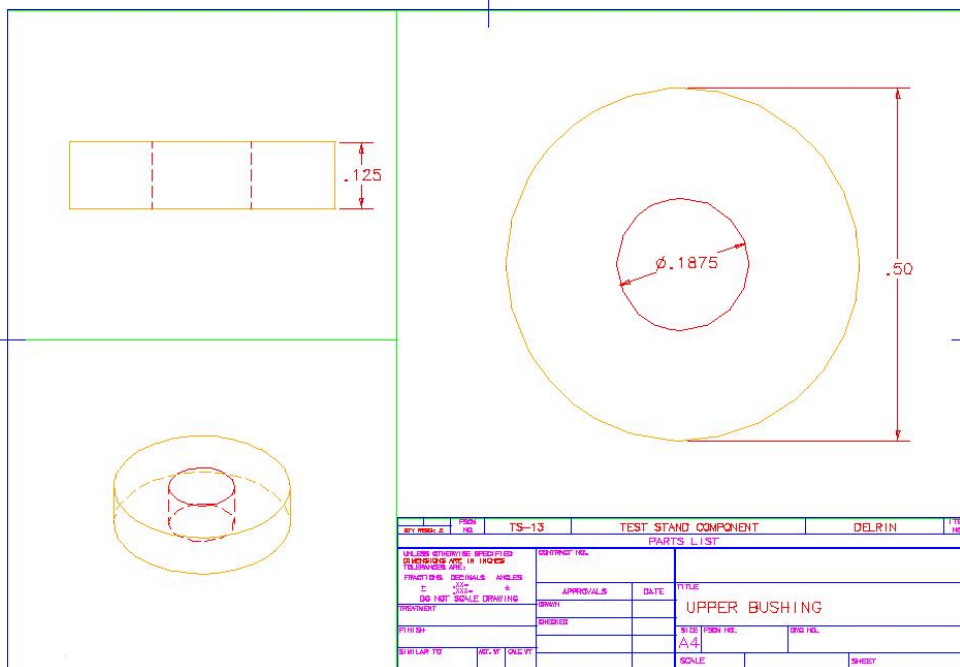
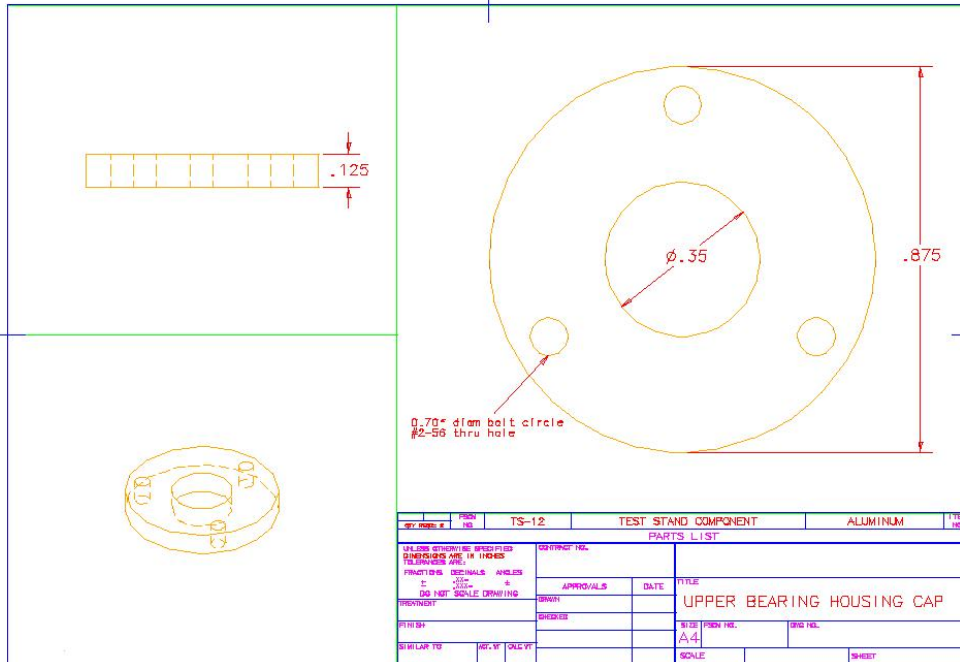


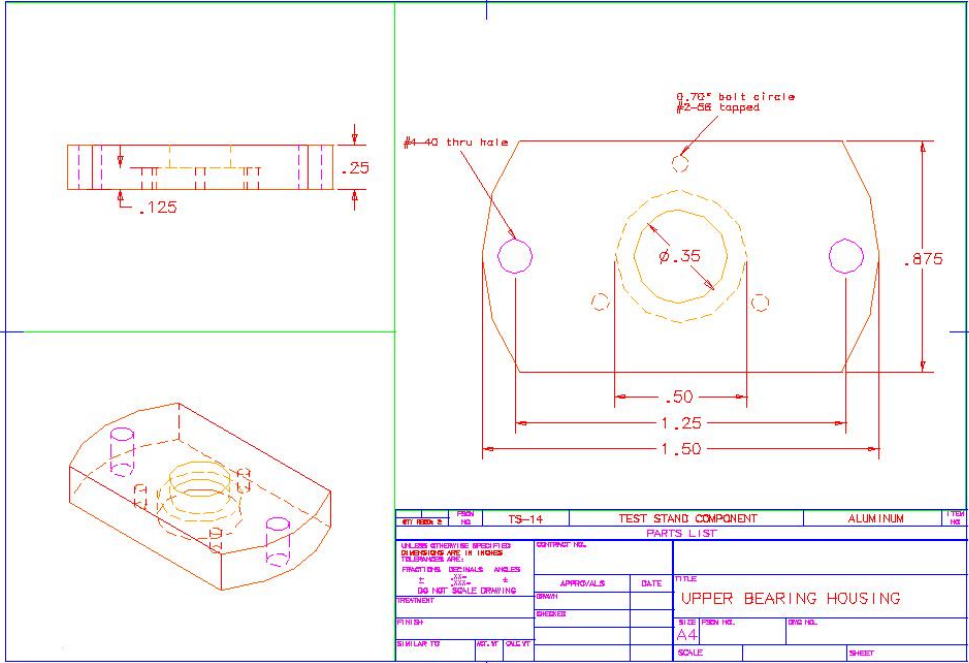


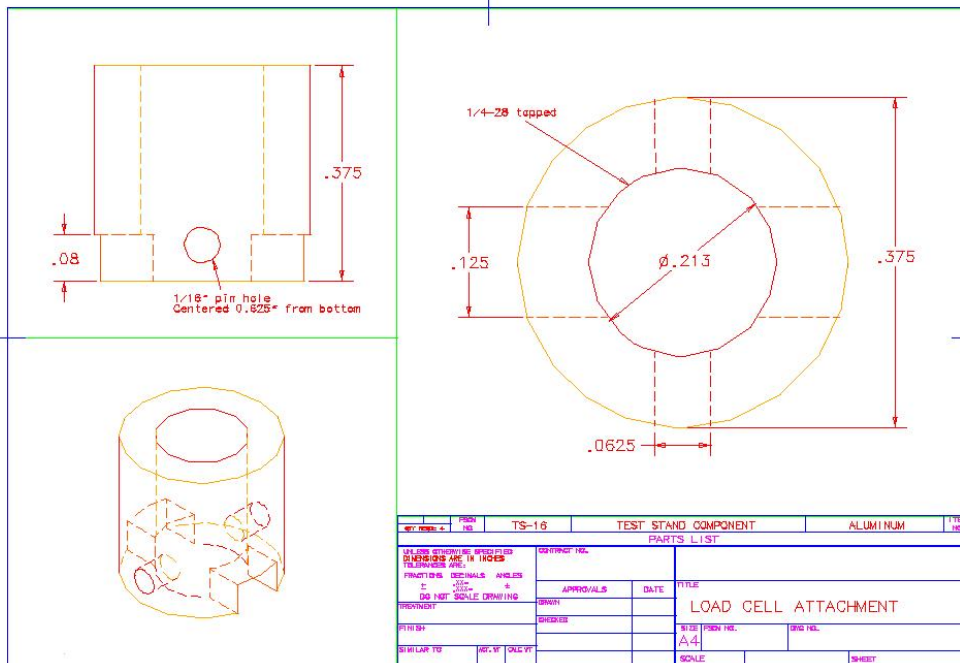
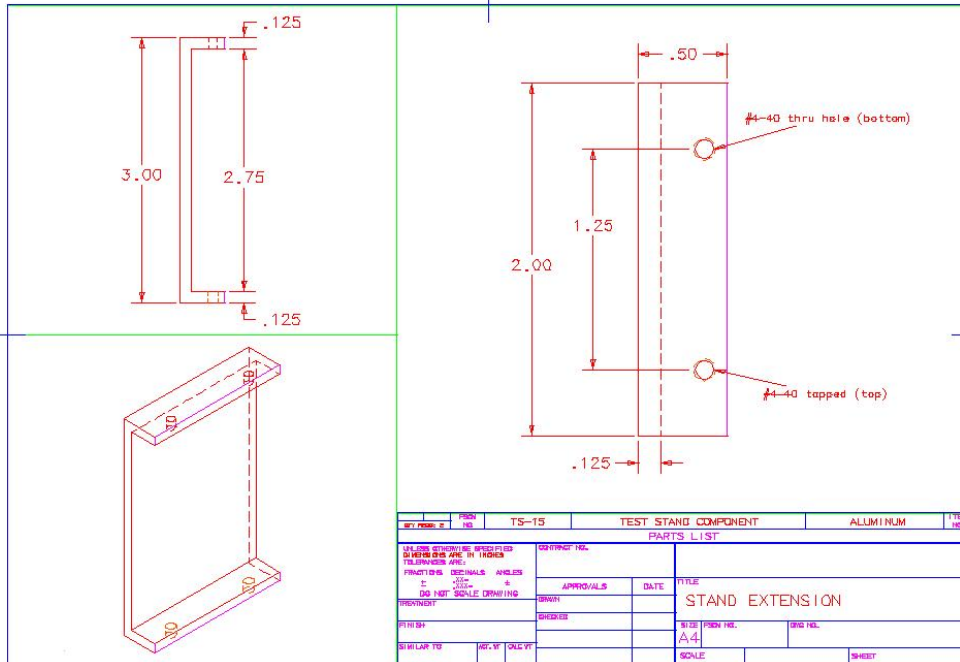


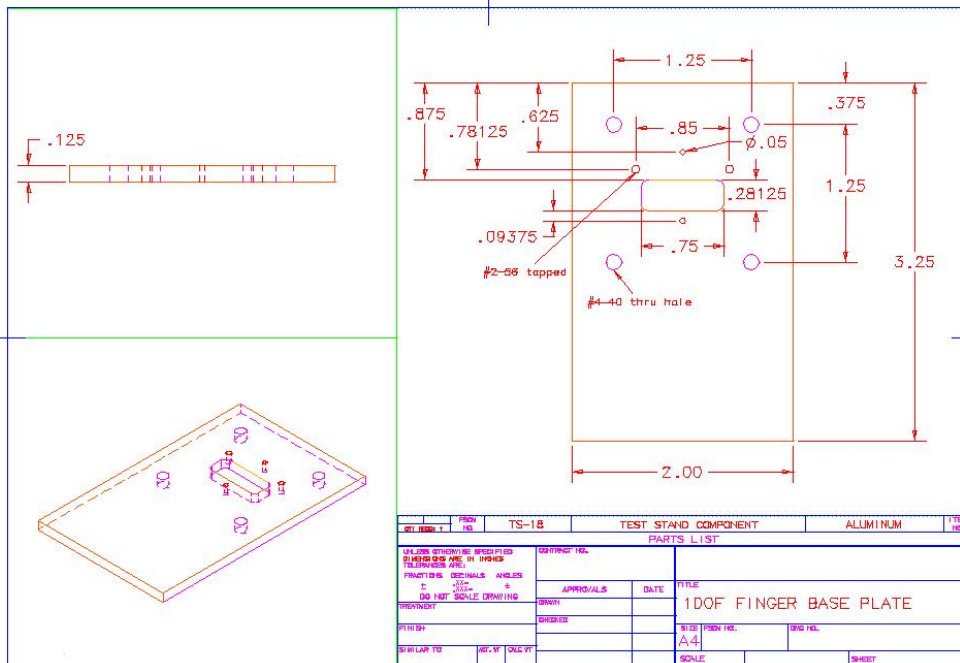
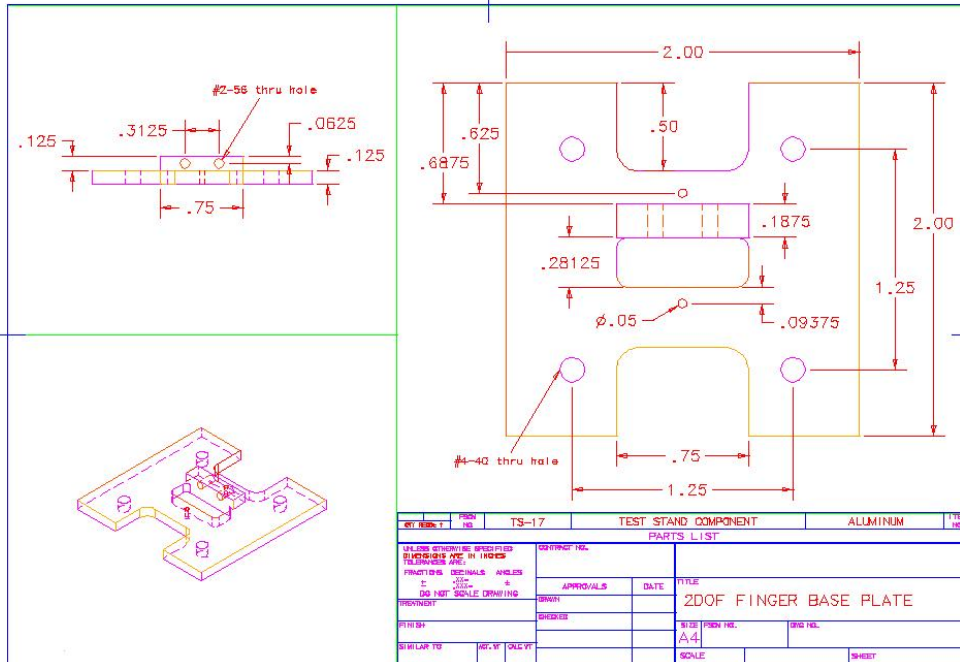


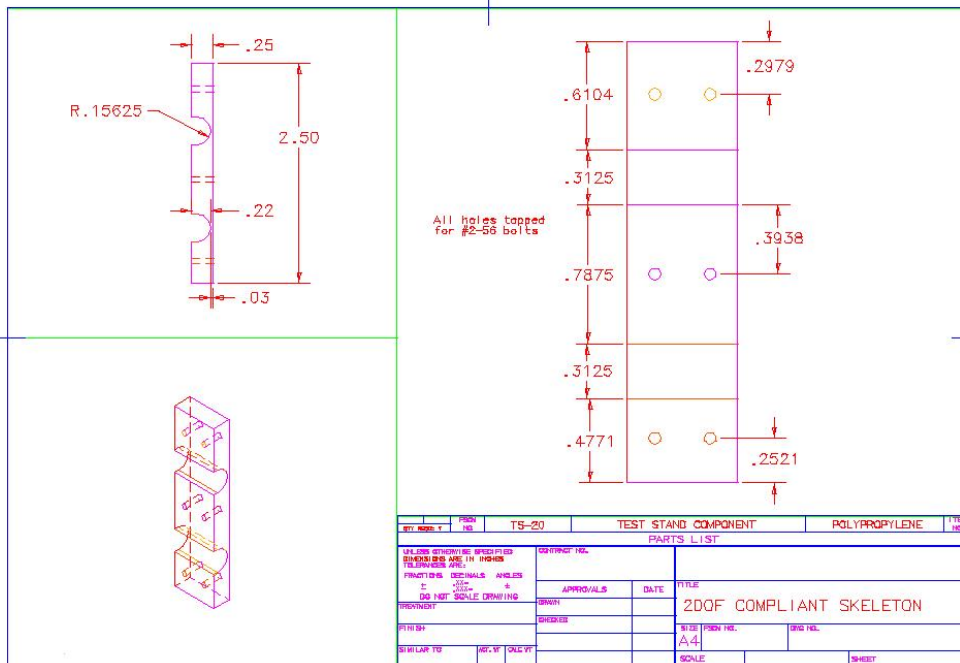
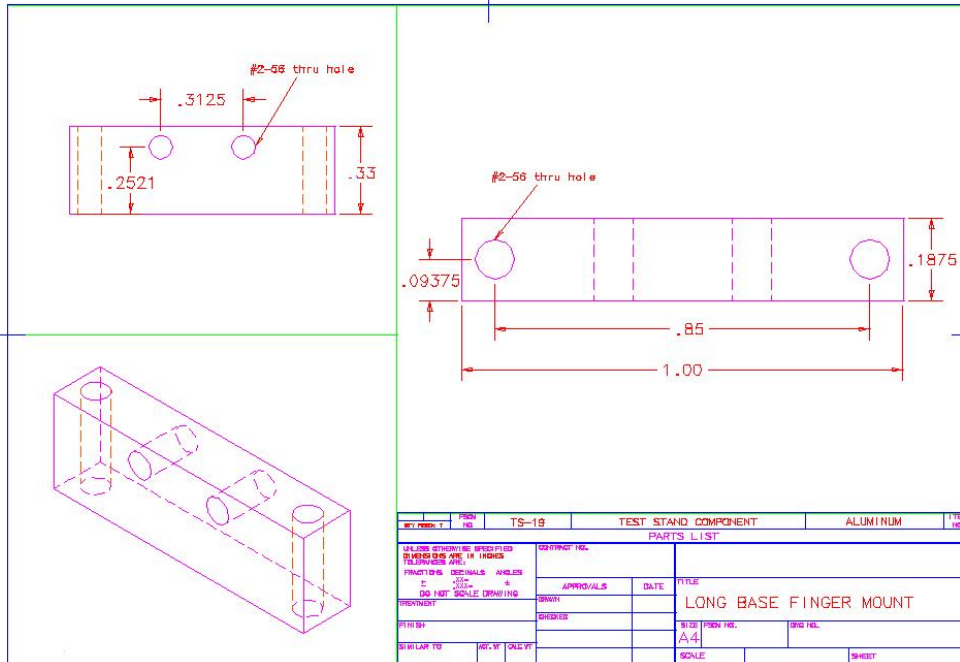


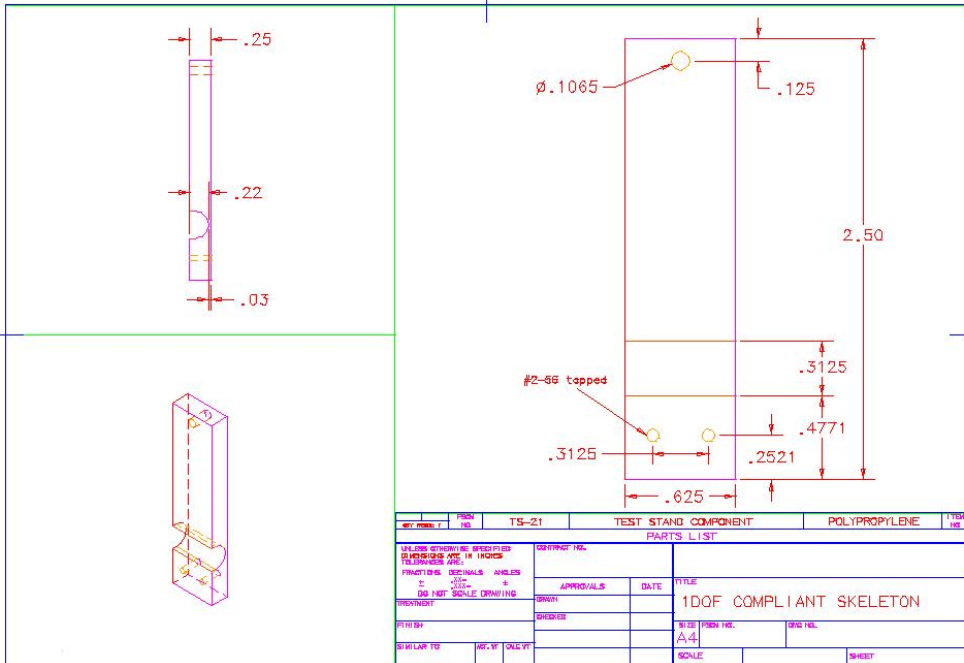












Appendix C

Kinematic Analysis

C.1 Mathematica Code

(* CALCULATE FORWARD KINEMATICS *)

```
ClearAll["Global*"];
```

(* Define Number of DOFs *)

```
DOF = 4;
```

(*DefineDHPParametersandJointType(1 = revolute, 0 = prismatic*)

```
 $\alpha_0 = 0; a_0 = 0; d_1 = 0; \theta_1 = \theta_1; \text{jtype}[1] = 1;$ 
```

```
 $\alpha_1 = \text{Pi}/2; a_1 = 0; d_2 = 0; \theta_2 = \theta_2; \text{jtype}[2] = 1;$ 
```

```
 $\alpha_2 = 0; a_2 = l_p; d_3 = 0; \theta_3 = \theta_3; \text{jtype}[3] = 1;$ 
```

```
 $\alpha_3 = 0; a_3 = l_m; d_4 = 0; \theta_4 = \theta_4; \text{jtype}[4] = 1;$ 
```

(* Calculate Local Link Transformation *)

```
For[ $i = 1, i \leq \text{DOF}, i++$ ,
```

```
 $T[i] = \{\{\text{Cos}[\theta_i], -\text{Sin}[\theta_i], 0, a_{i-1}\},$ 
```

```
 $\{\text{Sin}[\theta_i] * \text{Cos}[\alpha_{i-1}], \text{Cos}[\theta_i] * \text{Cos}[\alpha_{i-1}], -\text{Sin}[\alpha_{i-1}], -\text{Sin}[\alpha_{i-1}] * d_i\},$ 
```

```

{Sin [θi] * Sin [αi-1], Cos [θi] * Sin [αi-1], Cos [αi-1], Cos [αi-1] * di},
{0, 0, 0, 1}};

R[i] = Part[T[i], {1, 2, 3}, {1, 2, 3}];

p[i] = {T[i][[1, 4]], T[i][[2, 4]], T[i][[3, 4]]};

];

```

```
(*DefineTransformationfromNtoN + 1(tooltip)*)
```

```

pTN = {ld, 0, 0};

T[DOF + 1] = {{1, 0, 0, ld}, {0, 1, 0, 0}, {0, 0, 1, 0}, {0, 0, 0, 1}};

```

```
Print["LOCAL LINK TRANSFORMATIONS:"];
```

```
For[i = 1, i <= DOF + 1, i++,
```

```
Print["T[" , i, "] = ", MatrixForm[T[i]]];
```

```
];
```

```
LOCAL LINK TRANSFORMATIONS:
```

$$T[1] = \begin{pmatrix} \cos[\theta_1] & -\sin[\theta_1] & 0 & 0 \\ \sin[\theta_1] & \cos[\theta_1] & 0 & 0 \\ 0 & 0 & 1 & 0 \\ 0 & 0 & 0 & 1 \end{pmatrix}$$

$$T[2] = \begin{pmatrix} \cos[\theta_2] & -\sin[\theta_2] & 0 & 0 \\ 0 & 0 & -1 & 0 \\ \sin[\theta_2] & \cos[\theta_2] & 0 & 0 \\ 0 & 0 & 0 & 1 \end{pmatrix}$$

$$T[3]=\begin{pmatrix} \cos[\theta_3] & -\sin[\theta_3] & 0 & l_p \\ \sin[\theta_3] & \cos[\theta_3] & 0 & 0 \\ 0 & 0 & 1 & 0 \\ 0 & 0 & 0 & 1 \end{pmatrix}$$

$$T[4]=\begin{pmatrix} \cos[\theta_4] & -\sin[\theta_4] & 0 & l_m \\ \sin[\theta_4] & \cos[\theta_4] & 0 & 0 \\ 0 & 0 & 1 & 0 \\ 0 & 0 & 0 & 1 \end{pmatrix}$$

$$T[5]=\begin{pmatrix} 1 & 0 & 0 & l_d \\ 0 & 1 & 0 & 0 \\ 0 & 0 & 1 & 0 \\ 0 & 0 & 0 & 1 \end{pmatrix}$$

(* Compute Forward Kinematics *)

TN0 = T[1].T[2].T[3].T[4].T[5];

TN0 = Simplify[TN0];

RN0 = Part[TN0, {1, 2, 3}, {1, 2, 3}];

pN0 = Part[TN0, {1, 2, 3}, {4}];

Print["TN0=", MatrixForm[TN0]];

$$TN0 = \begin{pmatrix} \cos[\theta_1] \cos[\theta_2 + \theta_3 + \theta_4] & -\cos[\theta_1] \sin[\theta_2 + \theta_3 + \theta_4] & \sin[\theta_1] \\ \cos[\theta_2 + \theta_3 + \theta_4] \sin[\theta_1] & -\sin[\theta_1] \sin[\theta_2 + \theta_3 + \theta_4] & -\cos[\theta_1] \\ \sin[\theta_2 + \theta_3 + \theta_4] & \cos[\theta_2 + \theta_3 + \theta_4] & 0 \\ 0 & 0 & 0 \\ \cos[\theta_1] (\cos[\theta_2 + \theta_3 + \theta_4] l_d + \cos[\theta_2 \theta_3] l_m + \cos[\theta_2] l_p) & \sin[\theta_1] (\cos[\theta_2 + \theta_3 + \theta_4] l_d + \cos[\theta_2 + \theta_3] l_m + \cos[\theta_2] l_p) & \sin[\theta_2 + \theta_3 + \theta_4] l_d + \sin[\theta_2 + \theta_3] l_m + \sin[\theta_2] l_p \\ 1 & & \end{pmatrix}$$

(* INVERSE KINEMATICS *)

```

For[i = 1, i ≤ DOF + 1, i++,
invT[i] = Inverse[T[i]];
invT[i] = Simplify[invT[i]];
];
leftM = {{r11, r12, r13, px}, {r21, r22, r23, py}, {r31, r32, r33, pz}, {0, 0, 0, 1}};
leftM = invT[1].leftM;
leftM = Simplify[leftM];
rightM = T[2].T[3].T[4].T[5];
rightM = Simplify[rightM];
Print["leftM=", MatrixForm[leftM]];
Print["rightM=", MatrixForm[rightM]];
Print["invT[5]=", MatrixForm[invT[5]]];
p4 = invT[5].{px, py, pz, 1}
p40 = T[1].T[2].T[3].T[4];
p40 = Simplify[p40];
Print["p40=", MatrixForm[p40]];
leftM= 
$$\begin{pmatrix} r11\cos[\theta_1] + r21\sin[\theta_1] & r12\cos[\theta_1] + r22\sin[\theta_1] & r13\cos[\theta_1] + r23\sin[\theta_1] & px\cos[\theta_1] + py\sin[\theta_1] \\ r21\cos[\theta_1] - r11\sin[\theta_1] & r22\cos[\theta_1] - r12\sin[\theta_1] & r23\cos[\theta_1] - r13\sin[\theta_1] & py\cos[\theta_1] - px\sin[\theta_1] \\ r31 & r32 & r33 & pz \\ 0 & 0 & 0 & 1 \end{pmatrix}$$

rightM= 
$$\begin{pmatrix} \cos[\theta_2 + \theta_3 + \theta_4] & -\sin[\theta_2 + \theta_3 + \theta_4] & 0 & \cos[\theta_2 + \theta_3 + \theta_4]l_d + \cos[\theta_2 + \theta_3]l_m + \cos[\theta_2]l_p \\ 0 & 0 & -1 & 0 \\ \sin[\theta_2 + \theta_3 + \theta_4] & \cos[\theta_2 + \theta_3 + \theta_4] & 0 & \sin[\theta_2 + \theta_3 + \theta_4]l_d + \sin[\theta_2 + \theta_3]l_m + \sin[\theta_2]l_p \\ 0 & 0 & 0 & 1 \end{pmatrix}$$

invT[5]= 
$$\begin{pmatrix} 1 & 0 & 0 & -l_d \\ 0 & 1 & 0 & 0 \\ 0 & 0 & 1 & 0 \\ 0 & 0 & 0 & 1 \end{pmatrix}$$

p40= 
$$\begin{pmatrix} \cos[\theta_1]\cos[\theta_2 + \theta_3 + \theta_4] & -\cos[\theta_1]\sin[\theta_2 + \theta_3 + \theta_4] & \sin[\theta_1] & \cos[\theta_1](\cos[\theta_2 + \theta_3]l_m + \cos[\theta_2]l_p) \\ \cos[\theta_2 + \theta_3 + \theta_4]\sin[\theta_1] & -\sin[\theta_1]\sin[\theta_2 + \theta_3 + \theta_4] & -\cos[\theta_1] & \sin[\theta_1](\cos[\theta_2 + \theta_3]l_m + \cos[\theta_2]l_p) \\ \sin[\theta_2 + \theta_3 + \theta_4] & \cos[\theta_2 + \theta_3 + \theta_4] & 0 & \sin[\theta_2 + \theta_3]l_m + \sin[\theta_2]l_p \\ 0 & 0 & 0 & 1 \end{pmatrix}$$

(* VELOCITY PROPAGATION *)
zhat = {0, 0, 1};

```

(* Define Rotational Velocities *)

$$d\theta_1 = d\theta_1;$$

$$d\theta_2 = d\theta_2;$$

$$d\theta_3 = d\theta_3;$$

$$d\theta_4 = d\theta_4;$$

(* Propagate Velocities *)

$$\omega_0 = \{0, 0, 0\};$$

$$\nu_0 = \{0, 0, 0\};$$

For[$i = 1, i \leq \text{DOF}, i++$,

$$\omega_i = \text{Transpose}[R[i]].\omega_{i-1} + d\theta_i * \text{zhat};$$

$$\omega_i = \text{Simplify}[\omega_i];$$

$$\nu_i = \text{Transpose}[R[i]].(\nu_{i-1} + \text{Cross}[\omega_{i-1}, p[i]]);$$

$$\nu_i = \text{Simplify}[\nu_i];$$

Print[" ω ", i , "=", MatrixForm [ω_i], " ν ", i , "=", MatrixForm [ν_i];

];

$$\nu_{\text{DOF}+1} = \nu_{\text{DOF}} + \text{Cross}[\omega_{\text{DOF}}, p^{\text{TN}}];$$

$$\nu_{\text{DOF}+1} = \text{Simplify}[\nu_{\text{DOF}+1}];$$

Print[" ν ", $\text{DOF} + 1$, "=", MatrixForm [$\nu_{\text{DOF}+1}$];

$$\omega_1 = \begin{pmatrix} 0 \\ 0 \\ d\theta_1 \end{pmatrix} \quad \nu_1 = \begin{pmatrix} 0 \\ 0 \\ 0 \end{pmatrix}$$

$$\begin{aligned}
\omega 2 &= \begin{pmatrix} \sin [\theta_2] d\theta_1 \\ \cos [\theta_2] d\theta_1 \\ d\theta_2 \end{pmatrix} & \nu 2 &= \begin{pmatrix} 0 \\ 0 \\ 0 \end{pmatrix} \\
\omega 3 &= \begin{pmatrix} \sin [\theta_2 + \theta_3] d\theta_1 \\ \cos [\theta_2 + \theta_3] d\theta_1 \\ d\theta_2 + d\theta_3 \end{pmatrix} & \nu 3 &= \begin{pmatrix} \sin [\theta_3] d\theta_2 l_p \\ \cos [\theta_3] d\theta_2 l_p \\ -\cos [\theta_2] d\theta_1 l_p \end{pmatrix} \\
\omega 4 &= \begin{pmatrix} \sin [\theta_2 + \theta_3 + \theta_4] d\theta_1 \\ \cos [\theta_2 + \theta_3 + \theta_4] d\theta_1 \\ d\theta_2 + d\theta_3 + d\theta_4 \end{pmatrix} & \nu 4 &= \begin{pmatrix} \sin [\theta_4] d\theta_3 l_m + d\theta_2 (\sin [\theta_4] l_m + \sin [\theta_3 + \theta_4] l_p) \\ \cos [\theta_4] d\theta_3 l_m + d\theta_2 (\cos [\theta_4] l_m + \cos [\theta_3 + \theta_4] l_p) \\ -d\theta_1 (\cos [\theta_2 + \theta_3] l_m + \cos [\theta_2] l_p) \end{pmatrix} \\
\nu 5 &= \begin{pmatrix} \sin [\theta_4] d\theta_3 l_m + d\theta_2 (\sin [\theta_4] l_m + \sin [\theta_3 + \theta_4] l_p) \\ d\theta_4 l_d + d\theta_3 (l_d + \cos [\theta_4] l_m) + d\theta_2 (l_d + \cos [\theta_4] l_m + \cos [\theta_3 + \theta_4] l_p) \\ -d\theta_1 (\cos [\theta_2 + \theta_3 + \theta_4] l_d + \cos [\theta_2 + \theta_3] l_m + \cos [\theta_2] l_p) \end{pmatrix}
\end{aligned}$$

(* FORCE PROPAGATION *)

(* Define Link Loads *)

$$F_1 = \{0, 0, 0\};$$

$$F_2 = \{0, 2.08, 0\};$$

$$F_3 = \{0, 1.17, 0\};$$

$$F_4 = \{0, 3.25, 0\};$$

(*DefineForceCenters – CurrentValuesBasedonIndexFingerinCylindricalGrip*)

$$pF[4] = \{0.47 * l_d, 0, 0.02 * w_{\text{finger}}/2\};$$

$$pF[3] = \{0.74 * l_m, 0, 0.02 * w_{\text{finger}}/2\};$$

$$pF[2] = \{0.51 * l_p, 0, -0.14 * w_{\text{finger}}/2\};$$

$$pF[1] = \{0, 0, 0\};$$

(* Propagate Forces and Torques *)

$$f_4 = F_4;$$

$$n_4 = \text{Cross}[pF[4], F_4];$$

$$\text{Print}["f4=", \text{MatrixForm}[f_4]];$$

$$\text{Print}["n4=", \text{MatrixForm}[n_4]];$$

$$\text{For}[i = \text{DOF} - 1, i >= 1, i -,$$

$$f_i = R[i + 1].f_{i+1} + F_i;$$

$$f_i = \text{Simplify}[f_i];$$

$$n_i = R[i + 1].n_{i+1} + \text{Cross}[pF[i], F_i] + \text{Cross}[p[i + 1], R[i + 1].f_{i+1}];$$

$$n_i = \text{Simplify}[n_i];$$

$$\text{Print}["f", i, "=", \text{MatrixForm}[f_i]];$$

$$\text{Print}["n", i, "=", \text{MatrixForm}[n_i]];$$

];

$$f4 = \begin{pmatrix} 0 \\ 3.25 \\ 0 \end{pmatrix}$$

$$n4 = \begin{pmatrix} -0.0325w_{\text{finger}} \\ 0 \\ 1.5275l_d \end{pmatrix}$$

$$\begin{aligned}
f3 &= \begin{pmatrix} -3.25\text{Sin}[\theta_4] \\ 1.17 + 3.25\text{Cos}[\theta_4] \\ 0 \end{pmatrix} \\
n3 &= \begin{pmatrix} (-0.0117 - 0.0325\text{Cos}[\theta_4]) w_{\text{finger}} \\ -0.0325\text{Sin}[\theta_4] w_{\text{finger}} \\ 1.5275l_d + (0.8658 + 3.25\text{Cos}[\theta_4]) l_m \end{pmatrix} \\
f2 &= \begin{pmatrix} (-1.17 - 3.25\text{Cos}[\theta_4]) \text{Sin}[\theta_3] - 3.25\text{Cos}[\theta_3] \text{Sin}[\theta_4] \\ 2.08 + \text{Cos}[\theta_3] (1.17 + 3.25\text{Cos}[\theta_4]) - 3.25\text{Sin}[\theta_3] \text{Sin}[\theta_4] \\ 0 \end{pmatrix} \\
n2 &= \begin{pmatrix} (0.1456 + \text{Cos}[\theta_3] (-0.0117 - 0.0325\text{Cos}[\theta_4]) + 0.0325\text{Sin}[\theta_3] \text{Sin}[\theta_4]) w_{\text{finger}} \\ ((-0.0117 - 0.0325\text{Cos}[\theta_4]) \text{Sin}[\theta_3] - 0.0325\text{Cos}[\theta_3] \text{Sin}[\theta_4]) w_{\text{finger}} \\ 1.5275l_d + (0.8658 + 3.25\text{Cos}[\theta_4]) l_m + (1.0608 + \text{Cos}[\theta_3] (1.17 + 3.25\text{Cos}[\theta_4]) - 3.25\text{Sin}[\theta_3] \text{Sin}[\theta_4]) l_p \end{pmatrix} \\
f1 &= \begin{pmatrix} \text{Cos}[\theta_2] ((-1.17 - 3.25\text{Cos}[\theta_4]) \text{Sin}[\theta_3] - 3.25\text{Cos}[\theta_3] \text{Sin}[\theta_4]) + \\ \text{Sin}[\theta_2] (-2.08 + \text{Cos}[\theta_3] (1.17 + 3.25\text{Cos}[\theta_4]) + 3.25\text{Sin}[\theta_3] \text{Sin}[\theta_4]) \end{pmatrix} \\
n1 &= \begin{pmatrix} w_{\text{finger}} (\text{Sin}[\theta_2] ((0.0117 + 0.0325\text{Cos}[\theta_4]) \text{Sin}[\theta_3] + 0.0325\text{Cos}[\theta_3] \text{Sin}[\theta_4])) + \\ w_{\text{finger}} (\text{Cos}[\theta_2] (0.1456 + \text{Cos}[\theta_3] (-0.0117 - 0.0325\text{Cos}[\theta_4]) + 0.0325\text{Sin}[\theta_3] \text{Sin}[\theta_4])) \\ -1.5275l_d + (-0.8658 - 3.25\text{Cos}[\theta_4]) l_m + (-1.0608 + \text{Cos}[\theta_3] (-1.17 - 3.25\text{Cos}[\theta_4]) + 3.25\text{Sin}[\theta_3] \text{Sin}[\theta_4]) l_p \\ w_{\text{finger}} (\text{Cos}[\theta_2] ((-0.0117 - 0.0325\text{Cos}[\theta_4]) \text{Sin}[\theta_3] - 0.0325\text{Cos}[\theta_3] \text{Sin}[\theta_4])) + \\ w_{\text{finger}} (\text{Sin}[\theta_2] (0.1456 + \text{Cos}[\theta_3] (-0.0117 - 0.0325\text{Cos}[\theta_4]) + 0.0325\text{Sin}[\theta_3] \text{Sin}[\theta_4])) w_{\text{finger}} \end{pmatrix}
\end{aligned}$$

(* JOINT TORQUES *)

For[i = 1, i ≤ DOF, i++,

$\tau_i = \text{Dot}[n_i, \text{zhat}];$

Print [" τ ", i, "=", τ_i];

];

$\tau_1 = (\text{Cos}[\theta_2] ((-0.0117 - 0.0325\text{Cos}[\theta_4]) \text{Sin}[\theta_3] - 0.0325\text{Cos}[\theta_3] \text{Sin}[\theta_4]) +$

$\text{Sin}[\theta_2] (0.1456 + \text{Cos}[\theta_3] (-0.0117 - 0.0325\text{Cos}[\theta_4]) + 0.0325\text{Sin}[\theta_3] \text{Sin}[\theta_4])) w_{\text{finger}}$

$\tau_2 = 1.5275l_d + (0.8658 + 3.25\text{Cos}[\theta_4]) l_m + (1.0608 + \text{Cos}[\theta_3] (1.17 + 3.25\text{Cos}[\theta_4]) - 3.25\text{Sin}[\theta_3] \text{Sin}[\theta_4]) l_p$

$\tau_3 = 1.5275l_d + (0.8658 + 3.25\text{Cos}[\theta_4]) l_m$

$$\tau_4 = 1.5275l_d$$

(*JACOBIAN*)

(*Define z – vectors*)

$$R0[1] = R[1];$$

$$z_1 = R0[1].zhat;$$

For[$i = 2, i \leq \text{DOF}, i++$,

$$R0[i] = R0[i - 1].R[i];$$

$$z_i = R0[i].zhat;$$

];

(*DetermineRotationalJacobian – AssumesAllRevoluteJoints*)

$$\text{Jrot} = \text{Table}[0, \{3\}, \{\text{DOF}\}];$$

For[$i = 1, i \leq 3, i++$,

For[$j = 1, j \leq \text{DOF}, j++$,

$$\text{Jrot}[[i, j]] = z_j[[i]];$$

];

];

Print["Jrot=", MatrixForm[Jrot]];

(* Determine Translational Jacobian by Direct Differentiation*)

$$\text{Jtrans} = \text{Table}[0, \{3\}, \{\text{DOF}\}];$$

For[$i = 1, i \leq 3, i++$,

```

Jtrans[[i, 1]] = D [Part[TN0, i, 4],  $\theta_1$ ];
Jtrans[[i, 2]] = D [Part[TN0, i, 4],  $\theta_2$ ];
Jtrans[[i, 3]] = D [Part[TN0, i, 4],  $\theta_3$ ];
Jtrans[[i, 3]] = D [Part[TN0, i, 4],  $\theta_4$ ];

];

Jtrans = Simplify[Jtrans];

Print["Jtrans= ", MatrixForm[Jtrans]];

```

(* Combine Full Jacobian *)

```

J = Table[0, {6}, {DOF}];

For[i = 1, i <= 3, i++,

  For[j = 1, j <= DOF, j++,

    {J[[i, j]] = Jtrans[[i, j]],

     J[[i + 3, j]] = Jrot[[i, j]]}

  ]

];

```

```
Print["J=", MatrixForm[J]];
```

$$Jrot = \begin{pmatrix} 0 & \sin[\theta_1] & \sin[\theta_1] & \sin[\theta_1] \\ 0 & -\cos[\theta_1] & -\cos[\theta_1] & -\cos[\theta_1] \\ 1 & 0 & 0 & 0 \end{pmatrix}$$

Jtrans displayed by column

$$Jtrans1 = \begin{pmatrix} -\sin[\theta_1] (\cos[\theta_2 + \theta_3 + \theta_4] l_d + \cos[\theta_2 + \theta_3] l_m + \cos[\theta_2] l_p) \\ \cos[\theta_1] (\cos[\theta_2 + \theta_3 + \theta_4] l_d + \cos[\theta_2 + \theta_3] l_m + \cos[\theta_2] l_p) \\ 0 \end{pmatrix}$$

$$J_{\text{trans2}} = \begin{pmatrix} -\cos[\theta_1] (\sin[\theta_2 + \theta_3 + \theta_4] l_d + \sin[\theta_2 + \theta_3] l_m + \sin[\theta_2] l_p) \\ -\sin[\theta_1] (\sin[\theta_2 + \theta_3 + \theta_4] l_d + \sin[\theta_2 + \theta_3] l_m + \sin[\theta_2] l_p) \\ \cos[\theta_2 + \theta_3 + \theta_4] l_d + \cos[\theta_2 + \theta_3] l_m + \cos[\theta_2] l_p \end{pmatrix}$$

$$J_{\text{trans3}} = \begin{pmatrix} -\cos[\theta_1] \sin[\theta_2 + \theta_3 + \theta_4] l_d \\ -\sin[\theta_1] \sin[\theta_2 + \theta_3 + \theta_4] l_d \\ \cos[\theta_2 + \theta_3 + \theta_4] l_d \end{pmatrix}$$

$$J_{\text{trans4}} = \begin{pmatrix} 0 \\ 0 \\ 0 \end{pmatrix}$$

J displayed by column

$$J_1 = \begin{pmatrix} -\sin[\theta_1] (\cos[\theta_2 + \theta_3 + \theta_4] l_d + \cos[\theta_2 + \theta_3] l_m + \cos[\theta_2] l_p) \\ \cos[\theta_1] (\cos[\theta_2 + \theta_3 + \theta_4] l_d + \cos[\theta_2 + \theta_3] l_m + \cos[\theta_2] l_p) \\ 0 \\ 0 \\ 0 \\ 1 \end{pmatrix}$$

$$J_2 = \begin{pmatrix} -\cos[\theta_1] (\sin[\theta_2 + \theta_3 + \theta_4] l_d + \sin[\theta_2 + \theta_3] l_m + \sin[\theta_2] l_p) \\ -\sin[\theta_1] (\sin[\theta_2 + \theta_3 + \theta_4] l_d + \sin[\theta_2 + \theta_3] l_m + \sin[\theta_2] l_p) \\ \cos[\theta_2 + \theta_3 + \theta_4] l_d + \cos[\theta_2 + \theta_3] l_m + \cos[\theta_2] l_p \\ \sin[\theta_1] \\ -\cos[\theta_1] \\ 0 \end{pmatrix}$$

$$J_3 = \begin{pmatrix} -\cos[\theta_1] \sin[\theta_2 + \theta_3 + \theta_4] l_d \\ -\sin[\theta_1] \sin[\theta_2 + \theta_3 + \theta_4] l_d \\ \cos[\theta_2 + \theta_3 + \theta_4] l_d \\ \sin[\theta_1] \\ -\cos[\theta_1] \\ 0 \end{pmatrix}$$

$$J_4 = \begin{pmatrix} 0 \\ 0 \\ 0 \\ \sin[\theta_1] \\ -\cos[\theta_1] \\ 0 \end{pmatrix}$$

(* SINGULARITY ANALYSIS *)

(* $\theta_1 = 0$ Degree;

$\theta_2 = 90$ Degree;

$\theta_3 = 0$ Degree;

$\theta_4 = 0$ Degree;

J;

Print["J=", MatrixForm[J]];

MatrixRank[J]*)

(* MULTIFINGER KINEMATICS *)

(* Forward Kinematics to Wrist Frame *)

$n_{\text{digits}} = 5;$

$T_{\text{wrist}}[1] = \{\{0.707, 0, 0.707, 0.82\}, \{-0.707, 0, 0.707, -1.08\}, \{0, -1, 0, 0.5\}, \{0, 0, 0, 1\}\};$

$T_{\text{wrist}}[2] = \{\{1, 0, 0, 4.2\}, \{0, 1, 0, -1.32\}, \{0, 0, 1, 0\}, \{0, 0, 0, 1\}\};$

$T_{\text{wrist}}[3] = \{\{1, 0, 0, 4.2\}, \{0, 1, 0, -0.45\}, \{0, 0, 1, 0\}, \{0, 0, 0, 1\}\};$

$T_{\text{wrist}}[4] = \{\{1, 0, 0, 3.785\}, \{0, 1, 0, 0.45\}, \{0, 0, 1, 0\}, \{0, 0, 0, 1\}\};$

$T_{\text{wrist}}[5] = \{\{1, 0, 0, 3.785\}, \{0, 1, 0, 1.32\}, \{0, 0, 1, 0\}, \{0, 0, 0, 1\}\};$

For $[i = 1, i \leq n_{\text{digits}}, i++,$

$T_{\text{wn}}[i] = T_{\text{wrist}}[i].\text{TN0};$

$T_{\text{wn}}[i] = \text{Simplify}[T_{\text{wn}}[i]];$

$\text{Print}["T_{\text{wn}}[" , i, "]" = " , \text{MatrixForm}[T_{\text{wn}}[i]]];$

];

Twn matrices displayed by column

$$T_{\text{wn}}[1]1 = \begin{pmatrix} 0.707 \cos[\theta_1] \cos[\theta_2 + \theta_3 + \theta_4] + 0.707 \sin[\theta_2 + \theta_3 + \theta_4] \\ -0.707 \cos[\theta_1] \cos[\theta_2 + \theta_3 + \theta_4] + 0.707 \sin[\theta_2 + \theta_3 + \theta_4] \\ -\cos[\theta_2 + \theta_3 + \theta_4] \sin[\theta_1] \\ 0 \end{pmatrix}$$

$$T_{\text{wn}}[1]2 = \begin{pmatrix} 0.707 \cos[\theta_2 + \theta_3 + \theta_4] - 0.707 \cos[\theta_1] \sin[\theta_2 + \theta_3 + \theta_4] \\ 0.707 \cos[\theta_2 + \theta_3 + \theta_4] + 0.707 \cos[\theta_1] \sin[\theta_2 + \theta_3 + \theta_4] \\ \sin[\theta_1] \sin[\theta_2 + \theta_3 + \theta_4] \\ 0 \end{pmatrix}$$

$$T_{\text{wn}}[1]3 = \begin{pmatrix} 0.707 \sin[\theta_1] \\ -0.707 \sin[\theta_1] \\ \cos[\theta_1] \\ 0 \end{pmatrix}$$

tion from the base frame to the tool frame is given by

$$\begin{aligned}
{}^0_5T &= {}^0_1T {}^1_2T {}^2_3T {}^3_4T {}^4_5T \\
&= \begin{bmatrix} c_1 c_{234} & -c_1 s_{234} & s_1 & c_1(l_d c_{234} + l_m c_{23} + l_p c_2) \\ s_1 c_{234} & -s_1 s_{234} & -c_1 & s_1(l_d c_{234} + l_m c_{23} + l_p c_2) \\ s_{234} & c_{234} & 0 & l_d s_{234} + l_m s_{23} + l_p s_2 \\ 0 & 0 & 0 & 1 \end{bmatrix} \\
&= \begin{bmatrix} r_{11} & r_{12} & r_{13} & p_x \\ r_{21} & r_{22} & r_{23} & p_y \\ r_{31} & r_{32} & r_{33} & p_z \\ 0 & 0 & 0 & 1 \end{bmatrix}
\end{aligned}$$

Premultiplying both sides by ${}^0_1T^{-1}$ results in

$${}^0_1T^{-1} {}^0_5T = {}^1_2T {}^2_3T {}^3_4T {}^4_5T$$

where

$${}^0_1T^{-1} {}^0_5T = \begin{bmatrix} c_1 r_{11} + s_1 r_{21} & c_1 r_{12} + s_1 r_{22} & c_1 r_{13} + s_1 r_{23} & c_1 p_x + s_1 p_y \\ -s_1 r_{11} + c_1 r_{21} & -s_1 r_{12} + c_1 r_{22} & -s_1 r_{13} + c_1 r_{23} & -s_1 p_x + c_1 p_y \\ r_{31} & r_{32} & r_{33} & p_z \\ 0 & 0 & 0 & 1 \end{bmatrix}$$

and

$${}^1_5T = \begin{bmatrix} c_{234} & -s_{234} & 0 & l_d c_{234} + l_m c_{23} + l_p c_2 \\ 0 & 0 & -1 & 0 \\ s_{234} & c_{234} & 0 & l_d s_{234} + l_m s_{23} + l_p s_2 \\ 0 & 0 & 0 & 1 \end{bmatrix}$$

Analysis begins with an algebraic approach and equates elements (2,4)

$$-s_1 p_x + c_1 p_y = 0$$

which gives us θ_1 in terms of the desired goal point coordinates.

$$\theta_1 = \tan^{-1} \left(\frac{p_y}{p_x} \right)$$

To solve for angles θ_2 , θ_3 , and θ_4 , a geometric approach is used. Figure C.1 shows the arm plane with the manipulator in its desired position and orientation, represented by the point p and the angle ϕ .

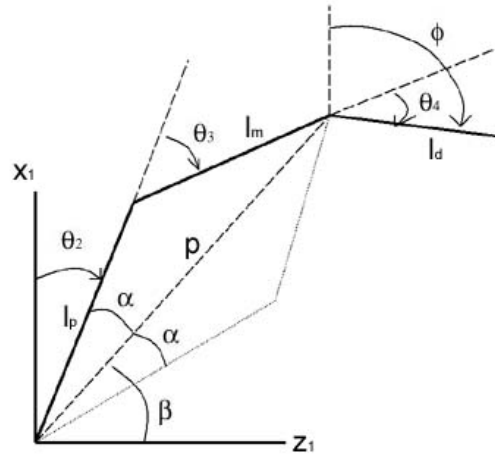


Figure C.1: Geometric View in Arm Plane

Using the law of cosines, θ_3 is solved as follows

$$p = \sqrt{p_x^2 + p_z^2}$$

$$p^2 = l_p^2 + l_m^2 - 2l_p l_m \cos(\pi + \theta_3)$$

$$p^2 = l_p^2 + l_m^2 + 2l_p l_m \cos \theta_3$$

$$\theta_3 = \cos^{-1} \left(\frac{p^2 - l_p^2 - l_m^2}{2l_p l_m} \right)$$

where θ_3 is constrained by the joint range of motion, -10° to 110° .

Further observations of the manipulator geometry shows θ_2 and θ_4 are given by

$$\theta_2 = \begin{cases} \beta + \alpha & \text{if } \theta_3 > 0, \\ \beta - \alpha & \text{if } \theta_3 < 0 \end{cases}$$

where

$$\beta = \text{atan2}(p_x, p_z)$$

$$l_m^2 = p^2 + l_p^2 - 2l_p p \cos \alpha$$

$$\alpha = \cos^{-1} \left(\frac{p^2 + l_p^2 - l_m^2}{2l_p p} \right)$$

and

$$\theta_4 = \phi - \theta_2 - \theta_3$$

where the joint range of motion constraints are -30° to 105° and -20° to 80° for θ_2 and θ_4 respectively.

BIBLIOGRAPHY

- [1] Amis, A. Variation of finger forces in maximal isometric grasp tests on a range of cylinder diameters. *Journal of Biomedical Engineering* **9** (1987).
- [2] Lee, J. & Rim, K. Measurement of finger joint angles and maximum finger forces during cylinder grip activity. *Journal of Biomedical Engineering* **13** (1991).
- [3] Rosheim, M. *Robot Evolution: The Development of Anthrobotics* (Wiley-Interscience, 1994).
- [4] Foster, T. *Development of a Four-Fingered Dexterous Robot End Effector for Space Operations*. Master's thesis, University of Maryland, College Park (2001).
- [5] Arbuckle, J. Measurement of the arc of digital flexion and joint movement ranges. *Journal of Hand Surgery* **20** (1995).
- [6] BioConcepts, http://www.bio-con.com/PDFs/hand_cht.pdf. *Hand Measurement Chart* (1998).
- [7] Akin, D. L., Roberts, B., Pilotte, K. & Baker, M. Robotic augmentation of eva for hubble space telescope servicing. In *AIAA Space 2003 Conference* (Long Beach, CA, 2003).
- [8] Jacobsen, S., Iversen, E., Knutti, D., Johnson, R. & Biggers, K. Design of the utah/m.i.t. dextrous hand. In *Proceedings of the IEEE International Conference on Robotics and Automation*, 1520–1532 (1986).
- [9] Salisbury, K. *Kinematic and force analysis of articulated hands*. Ph.D. thesis, Stanford University (1982).
- [10] Townsend, W. The barretthand grasper - programmably flexible part handling and assembly. *Industrial Robot* **27**, 181–188 (2000).
- [11] National Aeronautics and Space Administration. *Improved Cable-Drive Pre-tensioner*, msc-22405 edn.
- [12] Carrozza, M. *et al.* The development of a novel prosthetic hand - ongoing research and preiminary results. *IEEE/ASME Transactions on Mechatronics* **7**, 108–114 (2002).
- [13] Walker, R. *Shadow Dexterous Hand Technical Specification*. Shadow Robot Company (2005).
- [14] Lovchik, C. The robonaut hand: A dexterous robot hand for space. In *Proceedings of the IEEE International Conference on Robotics and Automation*, vol. 2 (1999).
- [15] NASA-STD-3000. *Man-Systems Integration Standards*, revision b edn. (1995).

- [16] Gray, H. *Anatomy of the Human Body* (Bartleby, <http://www.bartleby.com/107>, 2000). Electronic version of Gray's Anatomy, published by Lea and Febiger, 1918.
- [17] Luttgens, K. & Wells, K. F. *Kinesiology: Scientific Basis of Human Motion* (Saunders College Publishing, 1982), 7th edn.
- [18] *Anthropometric Source Book Volume II: A Handbook of Anthropometric Data* (NASA Reference Publication 1024, 1978).
- [19] Mallon, W., Brown, H. & Nunley, J. Digital ranges of motion; normal values in young adults. *Journal of Hand Surgery* **16** (1991).
- [20] Behnke, R. S. *Kinetic Anatomy* (Human Kinetics, 2006), 2nd edn.
- [21] Cutkosky, M. & Howe, R. *Dextrous Robot Hands*, chap. Human Grasp Choice and Robotic Grasp Analysis (Springer-Verlag, 1990).
- [22] Pilotte, K. *Analysis of Grasp Requirements for Telerobotic Satellite Servicing*. Master's thesis, University of Maryland, College Park (2004).
- [23] Kinoshita, H., Murase, T. & Bandou, T. Grip posture and forces during holding cylindrical objects with circular grasps. *Ergonomics* **39** (1996).
- [24] Howell, L. *Compliant Mechanisms* (John Wiley & Sons, New York, 2001).
- [25] Daerden, F. & Lefeber, D. Pneumatic artificial muscles: Actuators for robotics and automation. *European Journal of Mechanical and Environmental Engineering* **47**, 11–21 (2002).
- [26] Ma, N., Song, G. & Lee, H. Position control of shape memory alloy actuators with internal electrical resistance feedback using neural networks. *Smart Materials and Structures* **13**, 777–783 (2004).
- [27] Otsuka, K. & Ren, X. Recent developments in the research of shape memory alloys. *Intermetallics* **7**, 511–528 (1999).
- [28] Bar-Cohen, Y., Xue, T., Shahinpoor, M., Simpson, J. & Smith, J. Low-mass muscle actuators using electroactive polymers (eap). In *Proceedings of SPIE's 5th Annual International Symposium on Smart Structures and Materials* (San Diego, CA, 1998).
- [29] Bar-Cohen, Y. *Handbook on Biomimetics*, chap. Electroactive Polymers as Artificial Muscles - Capabilities, Potentials, and Challenges (NTS, 2000).
- [30] DeRossi, D. *et al.* Electro-active polymers for actuation and sensing in space applications. In *55th International Astronautical Congress of the International Astronautical Federation, the International Academy of Astronautics, and the International Institute of Space Law* (Vancouver, Canada, 2004).

- [31] Lee, G. R. *Development of a Mechanical Test Apparatus for Spacesuit Gloves*. Master's thesis, University of Maryland, College Park (2001).
- [32] Beyl, P. *et al.* Compliant actuation in new robotic applications. In *Proceedings of the 7th National Congress on Theoretical and Applied Mechanics* (Belgium, 2006).
- [33] Omega - *Subminiature Tension or Compression Load Cells*. <http://www.omega.com/Pressure/pdf/LC201.pdf> (2007).
- [34] Tekscan, Inc. *FlexiForce Sensors User Manual* (2005).
- [35] Pressure Profile Systems, Inc. *FingerTPS: Fingertip Tactile Pressure Sensors, User Manual*.
- [36] Craig, J. J. *Introduction to Robotics: Mechanics and Control* (Pearson Prentice Hall, 2005), third edn.
- [37] Murray, R., Li, Z. & Sastry, S. S. *A Mathematical Introduction to Robotic Manipulation* (CRC Press, 1994).
- [38] Wolovich, W. *Robotics: Basic Analysis and Design* (Holt, Rinehart, and Winston, 1986).
- [39] Lay, D. *Linear Algebra and its Applications* (Addison-Wesley, 2003).
- [40] Mason, M. T. & Salisbury, J. K. *Robot Hands and the Mechanics of Manipulation* (MIT Press, 1985).
- [41] Kerr, J. & Roth, B. Analysis of multifingered hands. *International Journal of Robotics Research* **4** (1986).